On the Stopband Characterization of Periodic Structures

Amir Ali Tavallaee

Department of Electrical & Computer Engineering
McGill University
Montreal, Canada

October 2006

A thesis submitted to McGill University in partial fulfillment of the requirements for the degree of Master of Engineering.

Your file Votre référence
ISBN: 978-0-494-28626-5
Our file Notre référence
ISBN: 978-0-494-28626-5

Abstract

Electromagnetic band-gap (EBG) structures, often termed frequency selective surfaces (FSSs) or photonic band-gap (PBG) materials, have found widespread applications as filters for microwaves and optical signals. Due to their frequency selective features and ease of implementation in printed circuit board (PCB) technology, EBG structures are utilized in power distribution networks (PDNs) to induce wide stopband and to provide global power/ground noise suppression. Attenuation characteristic of EBG structures within their forbidden frequency regions is examined in this thesis which ultimately provides the insertion loss obtained by inserting the EBG structure in the PDN. Bandgap characterization is efficiently achieved by applying the Bloch analysis to only one unit-cell of the EBG structure. For that purpose, two approaches have been investigated: the transmission-line (TL) technique and the finite element method (FEM). Printed-circuit EBG structures can be efficiently modeled by transmission-line circuits; thus TL techniques are widely used for their fast characterization. The developed TL model is exploited to investigate the power attenuation within the badgap regions of PDNs containing EBG structures. A full-wave finite element code has been developed for accurate prediction of the stopband characteristics of periodic media. A number of simple periodic geometries are examined by the finite element code showing unique spectral properties of EBG structures, such as existence of evanescent and/or complex modes within their stopbands.

Résumé

Les structures à bandes interdites électromagnétiques (BIE) sont également nommées surfaces sélectives en fréquence (SSF) ou bandes interdites photoniques (BIP). On leur connaît de nombreuses applications telles que les filtres micro-ondes et les filtres optiques. Grâce à leur dispositif de sélection de fréquence et leur facilité d'implantation dans les circuits imprimés (CI), les structures BIE sont usitées pour les réseaux de distribution de puissance (RDP) dans le but d'introduire une large bande atténuée et de supprimer le bruit global. Les caractéristiques d'atténuation de ces structures, à l'intérieur des régions de fréquences interdites, sont examinées dans cette thèse : en insérant la structure BIE dans le RDP, un affaiblissement d'insertion se produit. La caractérisation de la bande interdite est réalisée en appliquant l'analyse de Bloch à une cellule unique de la structure BIE. Pour cela deux approches ont été étudiées : la technique par lignes de transmission et la méthode par éléments finis. Les structures BIE à circuits imprimés peuvent être effectivement modélisées à l'aide de circuits à base de lignes de transmission. Cette technique est largement utilisée pour sa rapidité de caractérisation. Le modèle de transmission développé est exploité afin de déterminer l'atténuation présente dans les régions interdites des RDP contenant des structures BIE. Un code par analyse d'éléments finis a été développé pour prévoir, avec précision, les caractéristiques de la bande d'atténuation de la structure périodique. De simples structures périodiques sont examinées par ce programme démontrant ainsi des propriétés spectrales uniques de la structure BIE comme l'existence de modes évanescents et/ou complexes dans leur bande d'atténuation.

Acknowledgments

I owe my deepest gratitude to Prof. Jonathan P. Webb for serving as my dissertation advisor and his guidance throughout my graduate studies. His expertise in both electromagnetics and mathematics, his patience and his enthusiasm have taught me a lot during these two years.

I am grateful to my co-supervisor, Prof. Ramesh Abhari, for introducing me to this subject and her continued support of my work. She has always given her time graciously.

I am very blessed to have the love and support of my family. Without their help and encouragement nothing of this would have been possible.

Contents

List of Figures

List of Acronyms

1D	One-Dimensional
2D	Two-Dimensional
3D	Three-Dimensional
CEM	Computational ElectroMagnetics
Dof	Degree of Freedom
EBG	Electromagnetic Band-Gap
EKP	Electromagnetic Kronig-Penney
EM	ElectroMagnetic
FDFD	Finite-Difference Frequency-Domain
FDTD	Finite-Difference Time-Domain
FE	Finite Element
FEM	Finite Element Method
FFT	Fast Fourier Transform
FSS	Frequency Selective Surface
GEP	Generalized Eigenvalue Problem
GSVD	Generalized Singular-Value Decomposition
LSE	Longitudinal Section Electric
LSM	Longitudinal Section Magnetic
MoM	Method of Moments
MTL	Multiconductor Transmission-Line
NRI	Negative Refractive Index
OOP	Object-Oriented Programming
PBC	Periodic Boundary Condition
PBG	Photonic Band-Gap

PCB	Printed Circuit Board
PDN	Power Distribution Network
PEC	Perfect Electric Conductor
PMC	Perfect Magnetic Conductor
PPW	Parallel-Plate Waveguide
PRI	Positive Refractive Index
QEP	Quadratic Eigenvalue Problem
SSN	Simultaneous Switching Noise
SVD	Singular-Value Decomposition
TE	Transverse Electric
TEM	Transverse Electromagnetic
TL	Transmission-Line
TLM	Transmission-Line Matrix
TM	Transverse Magnetic
TRT	Transverse Resonance Technique

Chapter 1

Introduction

Wave propagation through spatially periodic structures has been the subject of continuing interest for many years [1, 2]. Periodic structures are increasingly utilized by a wide variety of microwave and optical devices primarily because of their potential applications in the design of waveguides, transmission-line systems and circuit components.

The interest in waveguiding structures of this type stems from the following two properties [3]: (a) they can support waves with phase velocities much less than the speed of light, (b) they may exhibit pass bands and stop bands, i.e. frequencies at which electromagnetic waves propagate along the structure (passband) and those at which they are cut off and cannot propagate (stopband). Property (a) is of fundamental importance in slow-wave devices [4]. Attribute (b) allows for their utilization as filters [5, 6] or as reflectors of electromagnetic energy [7, 8, 9] –they can reflect an incident wave without phase reversal (an artificially perfect magnetic conductor (PMC)). Therefore, analysis of periodic structures has historically provided two types of information: the dispersion characteristics of the supported modes and the phase of the reflection coefficient of the structure under plane wave illumination. However, in many practical cases, the former is of more interest as it provides useful information about the frequency-selective features of the periodic structures.

Many numerical and analytical techniques have been proposed during the past decades to examine the modal behavior of periodic structures, e.g. [10, 11, 12, 13, 14, 15]. Despite their unquestionable success in predicting the passbands and the dispersion of propagating modes within those frequency regions, these techniques fail to reveal enough information about the stopbands. Our knowledge of the stopband physics is still very limited –mostly restricted to those of one-dimensional (1D) periodic structures [16, 17]. Therefore, a complete modal analysis for all frequency ranges has not yet been realized.

The question that has been recently brought up about the stopband is whether there exist modes in the stopband or not, and if so what are they like and how are such modes related to the evanescence of electromagnetic energy? The answers to these questions will be crucial in gaining more physical insight into the stopband behavior and consequently the problem of eigenmode characterization of periodic structures. The first and a major step for stopband characterization is to obtain the propagation constants of evanescent and/or complex modes within banned frequencies and to predict the attenuation characteristics associated with each of them.

This thesis examines the attenuation behavior of different modes within the the stopband of doubly and triply periodic structures. Existence of evanescent modes with imaginary phase constants and/or modes with complex propagation constants in their forbidden frequency regions is investigated. Through several studied cases, the preceding questions about the nature of the stopband are answered[1] and various modal characteristics of periodic structures are demonstrated[2].

1.1 Rationale

1.1.1 Motivation

Recently, periodic structures have found wide spread applications as a viable solution to the problem of power/ground noise suppression and port isolation in high-speed digital and mixed-signal electronic circuits [19, 20, 21, 22, 23]. In these applications, the periodic structure is incorporated in the power distribution network of the electronic circuit by replacing one of the reference voltage planes such as the one shown in Fig. 1.1(a) [24]. Examples of implementation of these types of modified PDN in printed circuit board technology have been reported in the literature [20, 21, 22, 23, 25, 26]. A similar approach, nonetheless more challenging due to the fabrication, material and geometrical constraints, is applicable to

[1] It should be noted that the formation of stopbands and the mechanisms responsible for evanescence of electromagnetic energy within them are not the subject of the present thesis and are not investigated herein.

[2] It is worth noting that for a complete modal characterization of periodic structures visualization of the field distribution is required along with the propagation constant of each mode. Field visualization is out of the scope of this thesis and therefore is not addressed here.

modern system integration platforms, such as system-on/in-package. In all of these system integration scenarios, design engineers need to employ efficient methods to account for the added frequency-selective features of the modified PDN in simulations.

This modified PDN has a parallel-plate arrangement in which one of reference voltage planes may be periodically patterned (refer to Fig. 1.1(b)) or may be textured by using the

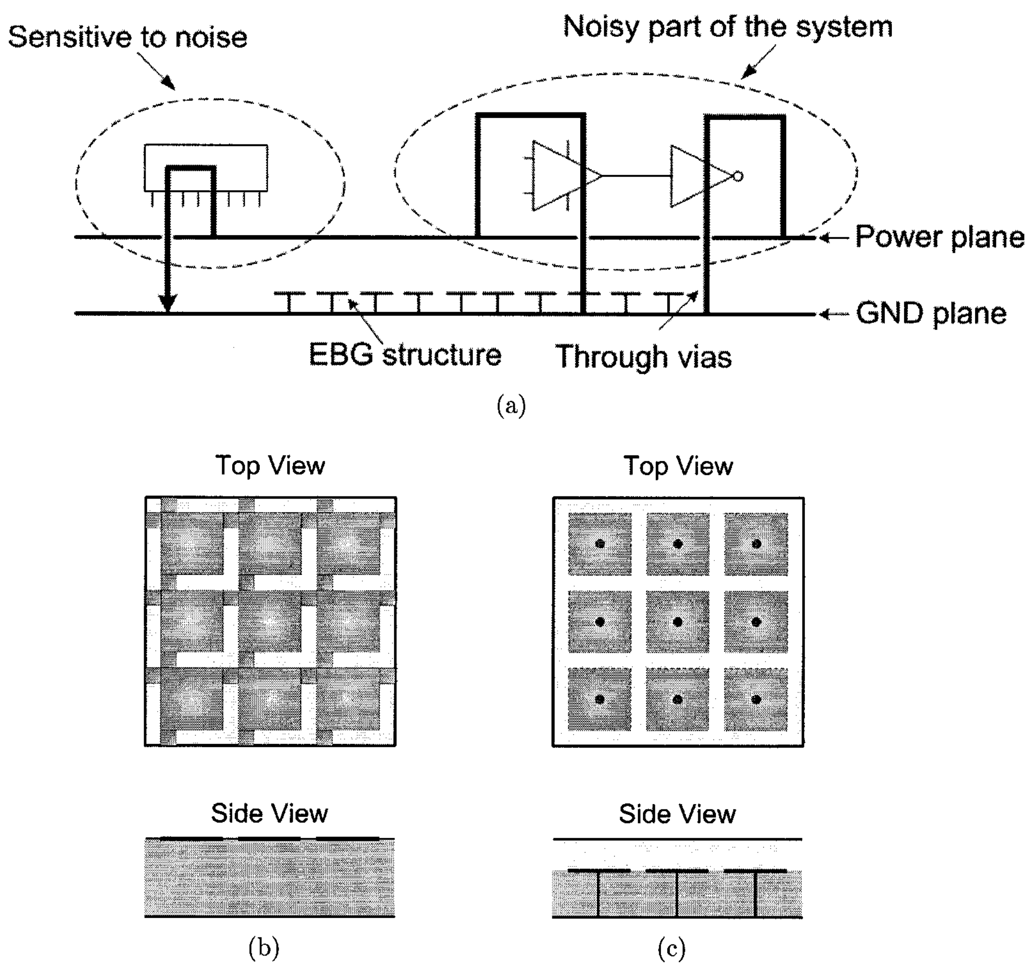

Fig. 1.1 (a) The parallel-plate PDN of a typical electronic circuit with an embedded periodic structure for suppression of power/ground noise [18]. (b) Top view and side view of a modified PDN with a patterned power plane [19]. (c) Top view and side view of a modified PDN with a textured ground plane [20].

mushroom EBG structure originally introduced by Sievenpiper *et. al.* [27] (see Fig. 1.1(c)). In both cases, owing to the modal characteristics of the periodic structure, a bandgap is induced within the operating frequency range of the PDN which acts as a band reject filter and mitigates the voltage fluctuations on the power delivery network. The insertion loss as well as the width of stopband region are two important measures of the efficiency of this noise suppression method. Wave evanescence is recognized as the responsible mechanism for the incurring losses in the stopband [28]. Therefore, prediction of the attenuation characteristics and the frequency range of the induced stopband are required in proper design of a periodic structure for a target application. This in turn calls for routines that are capable of capturing evanescent modes with real propagation constants and, in general, complex modes of such structures.

1.1.2 Objective

The objective of this thesis is to develop such codes for obtaining complex propagation constants of periodic structures in general and then applying them to configurations like Figs. 1.1(c), 1.1(b). Complex eigenmode analysis of periodic structures allows for their bandgap modal characterization. This information is particularly useful for investigation of the insertion loss characteristics achieved by inserting the EBG in the parallel-plate PDN configurations. Indeed, the ultimate goal is to investigate port isolation and insertion loss between two measurement ports placed arbitrarily in such modified PDN boards.

Fabrication of PDNs with EBG embodiments is a time consuming and costly process. Therefore, measuring the port isolation achieved by inserting the EBG in a parallel-plate PDN in a multilayer substrate is not always economical. On the other hand, using available general purpose electromagnetic (EM) solvers, the required insertion loss information can only be found along certain directions of signal propagation and for relatively small sizes of PDN boards. As the distance between two measurement ports increases, full-wave simulation of the whole PDN board becomes computationally costly and inefficient. Therefore, the alternative solution techniques proposed in this thesis, are investigated which enable efficient extraction of attenuation characteristics along arbitrary directions by analyzing only one unit-cell of the periodic structure. For that purpose, two distinct approaches have been investigated:

- Transmission-line techniques are used for fast characterization of the stopband behavior. Undoubtedly, field analysis techniques predict the passband/stopband modes most accurately; But, they are time consuming and have large memory requirements. TL techniques, on the contrary, allow for rapid estimation of passband/stopband characteristics and offer an efficient means for analysis of printed-circuit periodic structures.

- The finite element method is employed to accurately capture complex modes of such structures and thereby to predict their bandgap behavior. The FEM has been used for quite some time to find the propagating modes of periodic structures and to predict the pass band frequencies [12], and indeed commercial programs offer this capability. However, to the best of author's knowledge, no one has yet used FEM to find the attenuation constant of a mode in the stop band.

1.2 Thesis Organization

Following this introduction, Chapter 2 reviews the fundamentals of electromagnetic field modeling in periodic structures from both TL and FEM points of view. Chapter 3 is on transmission-line modeling of microwave and printed-circuit periodic structures. The emphasis will be on the stopband characterization of geometries that are particularly employed in power distribution networks. Chapter 4 addresses the finite element (FE) modeling of periodic structures. The FE model is implemented using an existing 3D FE code. This platform was enhanced for the prediction of bandgap behavior and complex eigenmode analysis of the electromagnetic waves in periodic media.

Simulation results for a number of representative periodic structures are presented in both Chapters 3 and 4. As far as the modal behavior is concerned, the so called $k-\beta$ diagrams are traditionally used to represent the dispersion characteristics of propagating modes. Corresponding to $k-\beta$ diagrams, $k-\alpha$ diagrams are introduced herein to characterize the attenuation of modes in the stopband frequencies. Indeed, the imaginary and the real parts of the complex propagation constants along arbitrary directions of propagation are plotted versus frequency to provide the desired $k-\beta$ and $k-\alpha$ diagrams, respectively. Extraction of insertion loss information from $k-\alpha$ diagrams is discussed in Chapter 3. Closing remarks and discussion on future work can be found in Chapter 5.

Chapter 2

Background

Techniques that are currently utilized for analyzing periodic structures can be divided into two major categories: transmission-line techniques and field analysis techniques. The former methods are borrowed from the area of transmission-line theory. These techniques model the dielectric media with transmission-lines and are well-suited to analysis of printed-circuit and TL-based periodic structures. TL techniques are constrained by the accuracy of results as well as the geometrical complexity of the structures they can handle. The latter methods are taken from the area of computational electromagnetics (CEM). These techniques are applicable, in principle, to any type of geometries and yield the most accurate results.

This chapter briefly reviews the fundamentals of electromagnetic fields modeling in periodic structures. The foundation for electromagnetic waves behavior in periodic media is provided in § 2.1. One-dimensional and two-dimensional (2D) transmission-line models are outlined in § 2.2. Also introduced in this section are the so called band diagrams ($k-\beta$ diagrams) and the corresponding attenuation diagrams ($k-\alpha$ diagrams) which characterize the propagating and evanescent modes of periodic structures, respectively. TL techniques deal with the equivalent voltages and currents along the periodic structure. Periodic network analysis is applied to these voltages and currents which allows for rapid production of dispersion and attenuation diagrams. § 2.3 presents different solution techniques from the area of CEM and discusses the salient features of each. CEM techniques, as opposed to transmission-line techniques, deal with the actual electromagnetic fields within the periodic structure and are therefore costly in terms of simulation time and memory requirements.

2.1 Fundamental Concepts

2.1.1 Maxwell's Equations

The basic equations of electromagnetic theory are Maxwell's equations. Assuming steady-state oscillations, these equations can be written in differential form [29] as,

$$\nabla \times \mathbf{E} = -j\omega\mathbf{B} \tag{2.1a}$$

$$\nabla \times \mathbf{H} = j\omega\mathbf{D} + \mathbf{J} \tag{2.1b}$$

$$\nabla \cdot \mathbf{D} = \rho \tag{2.1c}$$

$$\nabla \cdot \mathbf{B} = 0 \tag{2.1d}$$

where **E** is the electric field intensity, **B** is the magnetic flux density, **H** is the magnetic field intensity, and **D** is the electric flux density. The electric current density **J** and the electric charge density ρ are time-harmonic sources of the electromagnetic fields.

The electric charge density and the electric current density are related through the continuity equation

$$\nabla \cdot \mathbf{J} = -j\omega\rho \tag{2.2}$$

which is a statement of the conservation of charge. Moreover, for linear and isotropic media, the constitutive relations

$$\mathbf{D} = \epsilon_r\epsilon_0\mathbf{E} \tag{2.3a}$$

$$\mathbf{B} = \mu_r\mu_0\mathbf{H} \tag{2.3b}$$

provide the dependency between **E**, **D** and **B**, **H** where ϵ_0, μ_0, ϵ_r, and μ_r are the free-space permittivity, free-space permeability, relative permittivity, and relative permeability, respectively.

The four Maxwell's equations (2.1), together with the equation of continuity (2.2), and the constitutive relations (2.3) provide the necessary framework to predict all macroscopic electromagnetic interactions. With the assumption that there are no free charges and currents in the periodic medium, Eqns. (2.1a) and (2.1b) may be combined to obtain the governing wave equation:

$$\nabla \times \frac{1}{p}\nabla \times \mathbf{F} - k_0^2 q\mathbf{F} = 0 \tag{2.4}$$

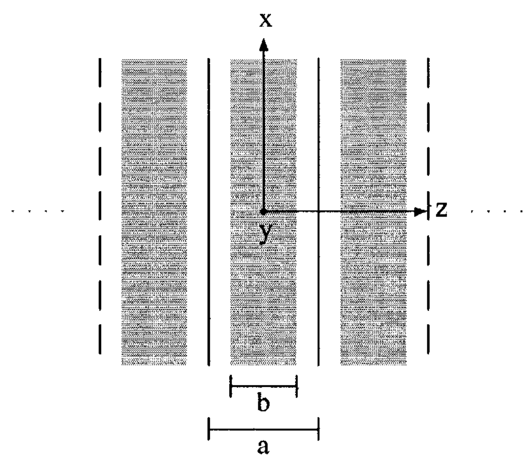

Fig. 2.1 One-dimensional array of dielectric slabs of width b in a periodic lattice with period a.

where $k_0 = \omega\sqrt{\mu_0\epsilon_0}$ is the free-space wave number, and $p = \mu_r$, $q = \epsilon_r$ for $\mathbf{F} = \mathbf{E}$ and $p = \epsilon_r$, $q = \mu_r$ for $\mathbf{F} = \mathbf{H}$. Eq. (2.4) along with the essential boundary conditions governs the propagation of electromagnetic waves in periodic media.

2.1.2 Flouqet's Theorem

The starting point in solving the problems of periodic structures is the Floquet's theorem. Floquet solved differential equations with periodic coefficients [30]. Bloch further extended Floquet's work to cases with periodic boundary conditions [31]. Floquet's theorem states that the wave solution in periodic media consists of an infinite number of *spatial harmonics.*

Consider the one-dimensional periodic array of dielectric slabs shown in Fig. 2.1. It has been found [31] that the fields at a point in an infinite periodic structure differ from those a period a away by a propagation factor $e^{-\gamma a}$. That is,

$$\mathbf{F}(x, y, z + a) = e^{-\gamma a}\, \mathbf{F}(x, y, z) \tag{2.5}$$

where $\gamma = \alpha + j\beta$ is the complex propagation constant along the z-axis. Consequently, the field solution $\mathbf{F}$, subject to the constraint (2.5), may be written as

$$\mathbf{F}(x, y, z) = e^{-\gamma z}\, \mathbf{F}_p(x, y, z) \tag{2.6}$$

where $\mathbf{F}_p(x, y, z)$ is a periodic function of z with period a.

From Eq. (2.6) we see that at some point $z + a$ the electromagnetic field is related to the one at z by:

$$\begin{aligned}\mathbf{F}(x, y, z + a) &= e^{-\gamma(z+a)}\ \mathbf{F}_p(x, y, z + a) \\ &= e^{-\gamma a} \cdot e^{-\gamma z}\ \mathbf{F}_p(x, y, z) \\ &= e^{-\gamma a}\ \mathbf{F}(x, y, z)\end{aligned} \tag{2.7}$$

which satisfies the repetitive pattern required by Eq. (2.5). Expanding $\mathbf{F}_p(x, y, z)$ into its infinite Fourier series [32],

$$\mathbf{F}_p(x, y, z) = \sum_n \mathbf{F}_{pn}(x, y) e^{-j\frac{2n\pi}{a}z} \tag{2.8}$$

the field solutions can then be represented as:

$$\begin{aligned}\mathbf{F}(x, y, z) &= \sum_n \mathbf{F}_{pn}(x, y) e^{-\gamma z} e^{-j\frac{2n\pi}{a}z} \\ &= \sum_n \mathbf{F}_{pn}(x, y) e^{-\gamma_n z}\end{aligned} \tag{2.9}$$

where $\gamma_n = \alpha + j(\beta + \frac{2n\pi}{a})$ and $\mathbf{F}_{pn}(x, y)$ are the expansion coefficients, given by:

$$\mathbf{F}_{pn}(x, y) = \frac{1}{a} \int_0^a \mathbf{F}_p(x, y, z)\ e^{j\frac{2n\pi}{a}z}\ \mathrm{d}z. \tag{2.10}$$

Each term in the expansion (2.9) is called a spatial harmonic. The n^{th} harmonic has a phase constant $\beta_n = \beta + \frac{2n\pi}{a}$, often referred to as the Floquet's mode numbers.

Therefore the exact solution for the one-dimensional periodic problem involves finding the complex mode numbers γ_n and the Floquet periodic vector variable $\mathbf{F}_p$. This method is termed the *plane wave expansion* method [33] and ordinarily results in an eigenvalue equation whose solution is obtained by equating the Fourier series coefficients on both sides of the equation. Finding expansion coefficients for two- and three-dimensional (3D) periodic structures is a mathematically rigorous task and closed form formula are only available for specific unit cell shapes [34]. Therefore, alternative solution techniques, such as simple transmission-line models or numerical methods, should be used for general cases.

The possibility of expressing the fields in a periodic structure in the form given by Eq. (2.5) means that we can restrict the analysis domain to a unit cell of the structure and find the field solution $\mathbf{F}$, itself, instead of $\mathbf{F}_p$. In this approach, those solutions which satisfy the (2.5) constraint on the unit cell surfaces are sought. Indeed, in a more general sense, Eq. (2.5) is a type of boundary condition that should be imposed on the tangential field components on the unit cell closures in such analysis. Once the solution is found within one period, say $0 \leq z \leq a$, the field everywhere else in the structure is given by:

$$\begin{aligned} \mathbf{F}(x, y, z + ma) &= \left(e^{-\gamma a}\right)^m \mathbf{F}(x, y, z) \\ &= e^{-\gamma ma}\, \mathbf{F}(x, y, z). \end{aligned} \tag{2.11}$$

Throughout this thesis, the latter approach will be followed and the modal characteristics of periodic structures will be explored by applying the Bloch analysis to a unit-cell. Modeling the electromagnetic fields within a unit-cell thus forms a major part of our analysis and is discussed in the subsequent sections.

2.2 Equivalent Transmission-Line Models

It is a common practice in electromagnetic theory to model dielectric properties like permittivity and permeability by distributed L–C networks. A prime example is the transmission-line matrix (TLM) method [35]. This concept has been widely used in various areas of electromagnetics including the propagation of waves in periodic media. Transmission-line theory allows one to formulate a simple solution for the propagation of transverse electromagnetic waves (TEM) through periodic media.

The use of equivalent TL models in the area of periodic structures was primarily introduced for modeling waveguides that were periodically loaded with capacitive/inductive discontinuities [3]. Since then, many L–C loaded planar transmission-line grids [36, 37], metal-dielectric periodic structures [14] and metamaterials [15, 38, 39] were investigated using TL techniques. What follows outlines briefly the basic ideas behind the TL modeling of periodic structures. General 1D and 2D transmission-line models are discussed here which are applicable to both periodic dielectric and printed-circuit structures. Chapter 3 is dedicated to implementation of this approach for 2D printed-circuit and TL-based structures.

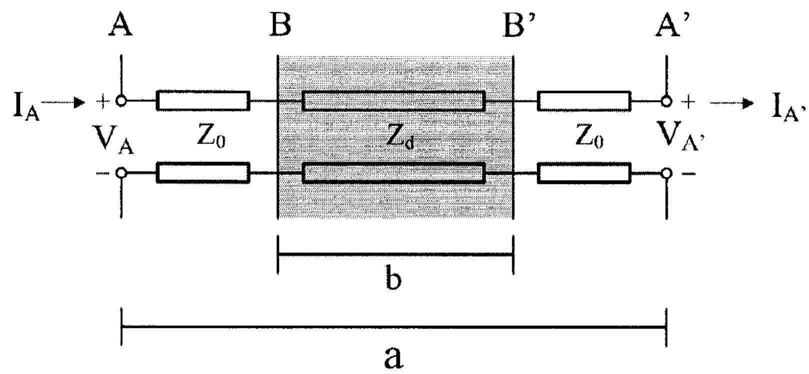

Fig. 2.2 Loaded transmission-line model for a unit cell of the one-dimensional array of dielectric slabs of width b and relative permittivity ϵ_{rd} in a periodic lattice with period a.

2.2.1 One-Dimensional Periodic Structures

Fig. 2.2 illustrates the equivalent transmission-line model for one unit cell of the one-dimensional array of dielectric slabs shown in Fig. 2.1. The dielectric slabs and free-space regions are modeled by short sections of transmission-line as seen in the figure where b is the length of the shorter section BB' with characteristic impedance Z_d and propagation constant $\gamma_d = j\beta_d = jk_0\sqrt{\epsilon_{rd}}$, a is the length of the entire transmission-line section AA', Z_0 is the characteristic impedance of the free-space transmission-line sections, and $\gamma_0 = j\beta_0 = jk_0$ is the propagation constant of the free-space sections of length $d = \frac{a-b}{2}$. A similar, but slightly different, model is applicable to 1D periodically loaded TL structures where transmission-lines sections are loaded by lumped L-C components instead of TL sections of different characteristics.

The propagation characteristics of such periodic media can be easily determined by analyzing the voltage and current waves that may propagate along the cascade connection of the three TL sections. Multiplying the ABCD transfer matrix of each transmission line section, yields

$$\begin{aligned}\begin{bmatrix} V_A \\ I_A \end{bmatrix} &= \begin{bmatrix} c_0 & jZ_0s_0 \\ \frac{j}{Z_0}s_0 & c_0 \end{bmatrix}\begin{bmatrix} c_d & jZ_ds_d \\ \frac{j}{Z_d}s_d & c_d \end{bmatrix}\begin{bmatrix} c_0 & jZ_0s_0 \\ \frac{j}{Z_0}s_0 & c_0 \end{bmatrix}\begin{bmatrix} V_{A'} \\ I_{A'} \end{bmatrix} \\ &= \begin{bmatrix} A & B \\ C & D \end{bmatrix}\begin{bmatrix} V_{A'} \\ I_{A'} \end{bmatrix}\end{aligned} \tag{2.12}$$

where $c_0 = \cos\beta_0 d$, $s_0 = \sin\beta_0 d$, $c_d = \cos\beta_d b$ and $s_d = \sin\beta_d b$. Moreover, V_A, I_A and $V_{A'}$, $I_{A'}$ represent the voltage and current waves at the input and output terminals of the unit cell, respectively. The ABCD parameters are given by

$$A = \cos\beta_d b \cos 2\beta_0 d - \left(\frac{Z_d^2 + Z_0^2}{2Z_d Z_0}\right) \sin\beta_d b \sin 2\beta_0 d \tag{2.13a}$$

$$B = jZ_0 \cos\beta_d b \sin 2\beta_0 d + j\sin\beta_d b \left(\frac{Z_d^2}{Z_0}\cos^2\beta_0 d - \frac{Z_0^2}{Z_d}\sin^2\beta_0 d\right) \tag{2.13b}$$

$$C = \frac{j}{Z_0}\cos\beta_d b \sin 2\beta_0 d + j\sin\beta_d b \left(\frac{Z_0^2}{Z_d}\cos^2\beta_0 d - \frac{Z_d}{Z_0^2}\sin^2\beta_0 d\right) \tag{2.13c}$$

$$D = \cos\beta_d b \cos 2\beta_0 d - \left(\frac{Z_d^2 + Z_0^2}{2Z_d Z_0}\right) \sin\beta_d b \sin 2\beta_0 d \tag{2.13d}$$

Due to the periodic nature of the structure, the voltage $V_{A'}$ and current $I_{A'}$ at the A' plane are required to be the same, except for a propagation factor, as the value of V_A and I_A at the A plane, that is

$$\begin{bmatrix} V_A \\ I_A \end{bmatrix} = \begin{bmatrix} e^{\gamma a} & 0 \\ 0 & e^{\gamma a} \end{bmatrix} \begin{bmatrix} V_{A'} \\ I_{A'} \end{bmatrix} \tag{2.14}$$

where $\gamma = \alpha + j\beta$ is the propagation constant along the structure and a is the length of the unit cell. Combining Eqns. (2.12), (2.14) yields

$$\begin{bmatrix} A - e^{\gamma a} & B \\ C & D - e^{\gamma a} \end{bmatrix} \begin{bmatrix} V_{A'} \\ I_{A'} \end{bmatrix} = \underline{0} \tag{2.15}$$

Nontrivial solutions of (2.15) are obtained by setting the determinant of the above matrix to zero which gives the following transcendental equation for the propagation constant γ,

$$\cosh\gamma a = \cos\beta_d b \cos 2\beta_0 d - \left(\frac{Z_d^2 + Z_0^2}{2Z_d Z_0}\right) \sin\beta_d b \sin 2\beta_0 d \tag{2.16}$$

The frequencies where the right hand side of Eq. (2.16) returns a value greater than unity and γ is purely real ($\gamma = \alpha$), define the stopband of the structure. At frequencies where $\cosh\gamma a < 1$, the propagation constant is purely imaginary ($\gamma = j\beta$). These frequencies define the passband of the structure.

In Fig. 2.3 is plotted the real and the imaginary parts of the complex propagation constant γ for a periodic array of dielectric slabs with filling fraction $b/a = \frac{1}{3}$ and relative

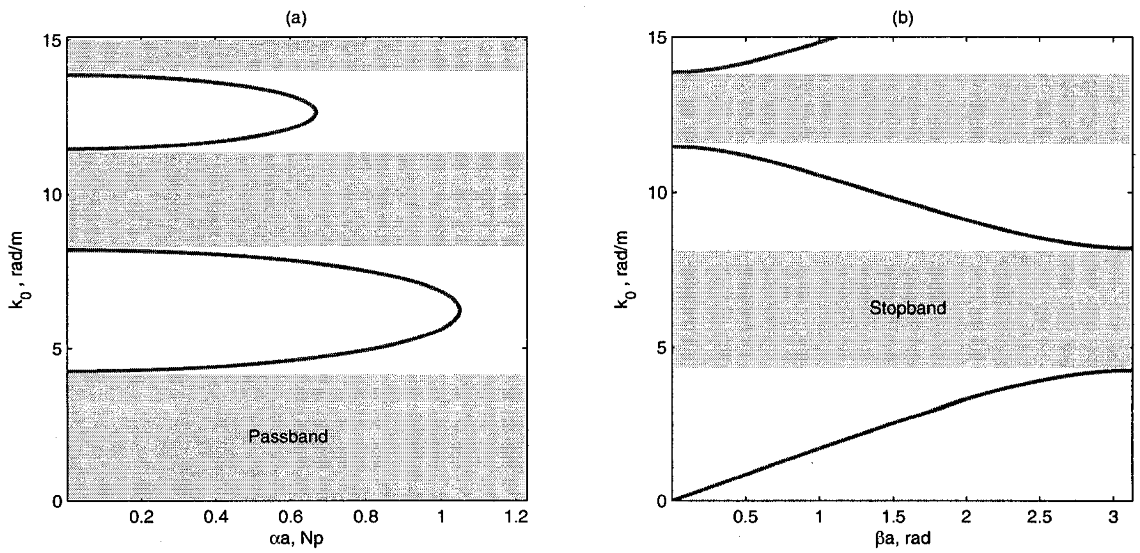

Fig. 2.3 Complex propagation constant for TEM modes of the one-dimensional array of dielectric slabs. (a) real part (attenuation diagram) and (b) imaginary part (band diagram).

dielectric constant $\epsilon_r = 9$. The accuracy of these results is verified against exact analytical solutions and numerical findings from FEM in Chapter 4. The band diagram (Fig. 2.3(b)) is shown for normalized propagation values $\beta a \in [0, \pi]$. The band diagram repeats itself every 2π. Moreover, if γ is a solution of Eq. (2.16), obviously $-\gamma$ is also a solution. Thus only normalized propagation values between 0 and π need to be calculated to determine all of the propagating modes in the structure. This region is often referred to as the *irreducible Brillouin zone* [1]. For one-dimensional periodic structures, this is a trivial determination. For two-dimensional structures, however, the irreducible Brillouin zone becomes more complicated. Further description of the Brillouin zone for two-dimensional square lattices will be given in the following section. The attenuation diagram (Fig. 2.3(a)) provides the stopband behavior and is plotted for the normalized values αa.

2.2.2 Two-Dimensional Periodic Structures

Structures with periodicity in two directions can also be represented conveniently by their equivalent transmission line models. A two-dimensional periodic array of air holes (edge length b) drilled in a dielectric medium with period a is depicted in Fig. 2.4. Also shown

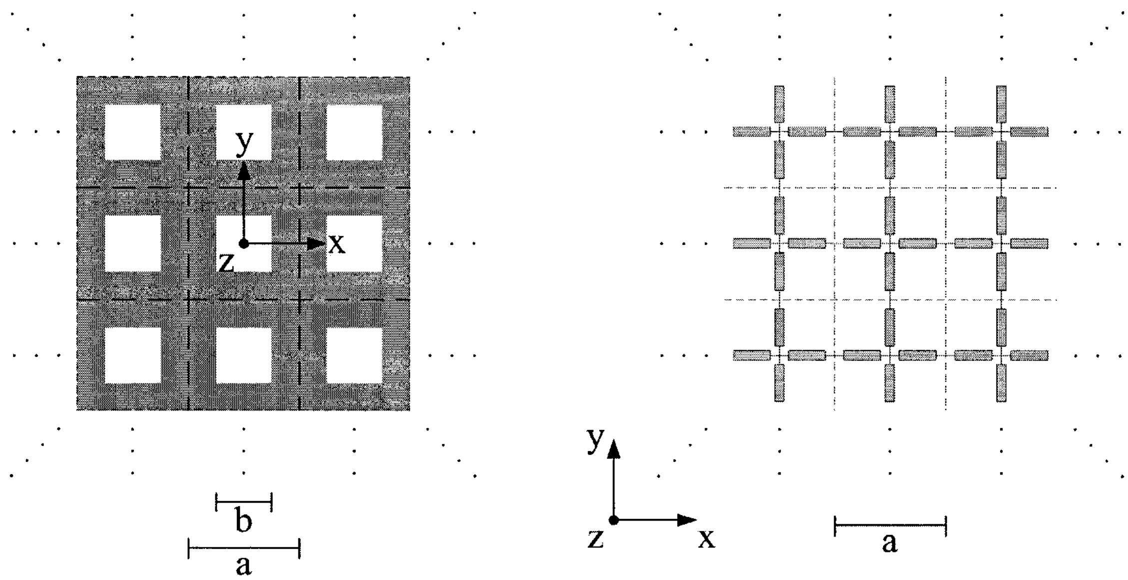

Fig. 2.4 Cross-sectional view of two-dimensional array of air holes of edge length b drilled in a dielectric medium with period a. (a) The actual periodic structure and (b) its equivalent transmission-line network representation.

in the figure is the equivalent TL network of the structure representing the TM_z[1] waves that may propagate along the x and y axes. Owing to the specific arrangement of the electric and magnetic fields for TE_z[2] modes, they cannot be captured by the transmission line model and therefore are not considered here.

The unit cell of the TL model comprises of four orthogonally arranged transmission line sections of length $a/2$ (see Fig. 2.5). In each branch the air hole and the dielectric regions are modeled by short sections of transmission line as seen in Fig. 2.5(b) where $b/2$ is the length of the free-space section with characteristic impedance Z_0 and propagation constant $\gamma_0 = j\beta_0 = jk_0$. Dielectric TL sections have a length of $d = (a - b)/2$, characteristic impedance of Z_d and propagation constant $\gamma_d = j\beta_d = jk_0\sqrt{\epsilon_{rd}}$. It is worth noting that whereas the 1D TL model is exact, this 2D model is not. The 2D TL model neglects the effect of sharp edges at the corners of the drilled air holes within the unit cell.

The ABCD matrix of each branch is obtained by multiplying the transfer matrix of the

[1]If the electric field has only an axial (or z-directed) component, the mode is transverse magnetic to z and is denoted TM_z.

[2]If the electric field has only components in the transverse x-y plane, the mode is transverse electric to z and is denoted TE_z.

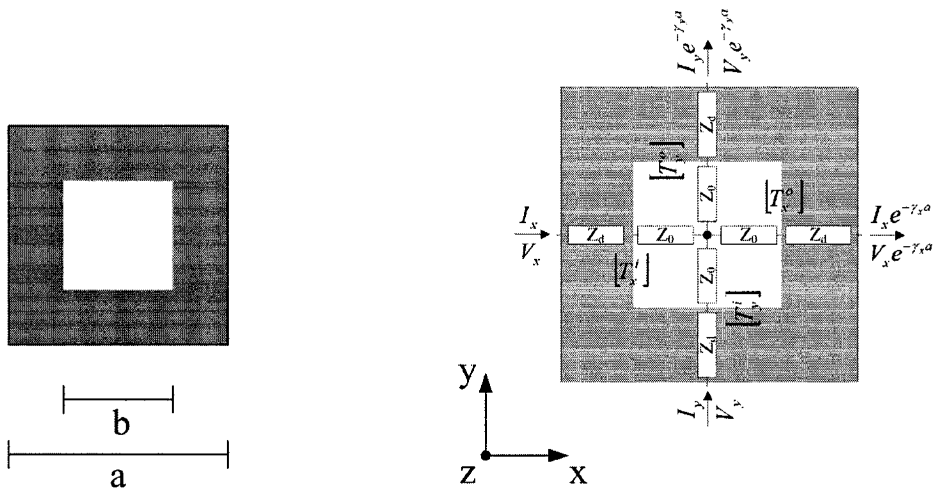

Fig. 2.5 Top view of a unit cell of the two-dimensional periodic array of air holes drilled in a dielectric medium. (a) The actual periodic dielectric unit cell and (b) its equivalent transmission-line network representation.

two transmission line sections yielding

$$T_k^i = \begin{bmatrix} A_k^i & B_k^i \\ C_k^i & D_k^i \end{bmatrix} = \begin{bmatrix} \cos\beta_d d & jZ_d \sin\beta_d d \\ \frac{j}{Z_d}\sin\beta_d d & \cos\beta_d d \end{bmatrix} \begin{bmatrix} \cos\beta_0 \frac{b}{2} & jZ_0 \sin\beta_0 \frac{b}{2} \\ \frac{j}{Z_0}\sin\beta_0 \frac{b}{2} & \cos\beta_0 \frac{b}{2} \end{bmatrix} \tag{2.17}$$

$$T_k^o = \begin{bmatrix} A_k^o & B_k^o \\ C_k^o & D_k^o \end{bmatrix} = \begin{bmatrix} \cos\beta_0 \frac{b}{2} & jZ_0 \sin\beta_0 \frac{b}{2} \\ \frac{j}{Z_0}\sin\beta_0 \frac{b}{2} & \cos\beta_0 \frac{b}{2} \end{bmatrix} \begin{bmatrix} \cos\beta_d d & jZ_d \sin\beta_d d \\ \frac{j}{Z_d}\sin\beta_d d & \cos\beta_d d \end{bmatrix} \tag{2.18}$$

where $k = x, y$. Note the order in which the matrices are multiplied for input/output stages. Applying Bloch boundary conditions to the voltages and currents at the ports of the unit cell, along with Kirchhoff's voltage and current laws at the intersection yields the following system of linear equations:

$$(D_x^i/\Delta_x^i - A_x^o e^{-\gamma_x a})V_x - (B_x^i/\Delta_x^i - B_x^o e^{-\gamma_x a})I_x = 0 \tag{2.19a}$$

$$(D_y^i/\Delta_y^i - A_y^o e^{-\gamma_y a})V_y - (B_y^i/\Delta_y^i - B_y^o e^{-\gamma_y a})I_y = 0 \tag{2.19b}$$

$$(A_x^o e^{-\gamma_x a})V_x + (B_x^o e^{-\gamma_x a})I_x - (A_y^o e^{-\gamma_y a})V_y - (B_y^o e^{-\gamma_y a})I_y = 0 \tag{2.19c}$$

$$\begin{aligned} &(C_x^i/\Delta_x^i + C_x^o e^{-\gamma_x a})V_x + (C_y^i/\Delta_y^i + C_y^o e^{-\gamma_y a})V_y \\ -&(A_x^i/\Delta_x^i - D_x^o e^{-\gamma_x a})I_x - (A_y^i/\Delta_y^i - D_y^o e^{-\gamma_y a})I_y = 0 \end{aligned} \tag{2.19d}$$

where $\Delta_k^i = A_k^i D_k^i - B_k^i C_k^i$, $(k = x, y)$ and $\gamma_x = \alpha_x + j\beta_x$, $\gamma_y = \alpha_y + j\beta_y$ denote the propagation constants along x and y, respectively. Eliminating I_x, I_y from (2.19) we obtain the homogeneous matrix equation

$$(G)\begin{pmatrix} V_x \\ V_y \end{pmatrix} = \begin{pmatrix} g_{1x} & -g_{1y} \\ g_{2x} & g_{2y} \end{pmatrix}\begin{pmatrix} V_x \\ V_y \end{pmatrix} = \underline{0} \tag{2.20}$$

where

$$g_{1k} = \frac{B_k^i A_k^o + B_k^o D_k^i}{B_k^i + B_k^o \Delta_k^i e^{-\gamma_k a}}\, e^{-\gamma_k a} \tag{2.21a}$$

$$g_{2k} = \frac{1 + \Delta_k^o \Delta_k^i e^{-2\gamma_k a} - \left(C_k^i B_k^o + C_k^o B_k^i + A_k^i A_k^o + D_k^o D_k^i\right) e^{-\gamma_k a}}{B_k^i + B_k^o \Delta_k^i e^{-\gamma_k a}} \tag{2.21b}$$

with $\Delta_k^o = A_k^o D_k^o - B_k^o C_k^o$, $(k = x, y)$. The system (2.20) admits a nontrivial solution if $\det(G) = 0$, which yields the dispersion equation

$$\cosh \gamma_x a + \cosh \gamma_y a = 2\cos\left(\beta_0 b + 2\beta_d d\right) + \left(2 - \frac{Z_0}{Z_d} - \frac{Z_d}{Z_0}\right)\sin \beta_0 b \sin 2\beta_d d \tag{2.22}$$

for the two-dimensional periodic dielectric structure.

The propagating modes of the structure are found by specifying the propagation vector ($\gamma_x = j\beta_x$, $\gamma_y = j\beta_y$) and seeking the frequency solutions. The solutions of the frequencies of the unique propagation vectors in the structure are found for specific values of $\{\beta_x a, \beta_y a\} \in [0, \pi]$ according to the irreducible Brillouin zone of the unit cell. For the square lattice, all of the possible directions of propagation are grouped into eight regions with particular symmetry (refer to Fig. 2.6). Symmetry considerations of the square lattice reveals that the number of unique regions of propagation is one [1]. The shaded area in Fig. 2.6 is the irreducible Brillouin zone of the isotropic square lattice and represents the smallest region where propagation within the lattice is unique. This region is typically defined by symmetric points on the edges of the lattice denoted Γ, X, and M. In order to completely determine all the admitted modes, every possible vector that falls into the irreducible Brillouin zone must be checked. Fortunately, the band structure can be determined approximately by sweeping the edges of the zone. Along the Γ–X line modes of the form $\beta = \beta_x \hat{x} + 0\hat{y}$ are examined. The X–M line is for modes of the form $\beta = \frac{\pi}{a}\hat{x} + \beta_y \hat{y}$ and the M–Γ line is for modes of the form $\beta = \beta_x \hat{x} + \beta_y \hat{y}$ where $\beta_x = \beta_y$.

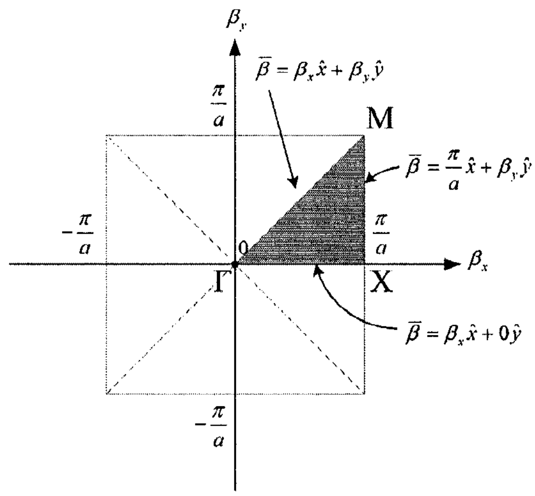

Fig. 2.6 Irreducible Brillouin zone of the isotropic square lattice with lattice constant a.

The full band structure (TM_z) for a periodic array of air holes with $b/a = 0.25$ drilled in a dielectric medium with $\epsilon_r = 13$ is shown in Fig. 2.7. A complete TM band gap exists over a significant range of frequencies. Certainly, larger incomplete bands exist (particularly in the Γ–X direction) where propagation is allowed for specific directions and these gaps can be effectively used in designs that do not need total omni-directional stopbands. The accuracy of these results is verified against plane wave expansion method [34]. A good agreement between both results was found up to certain frequencies.

Other two-dimensional periodic structures, such as the one shown in Fig. 1.1(b), can also be investigated using the preceding formulation. In Chapter 3, we have investigated a number of printed periodic structures using the above TL techniques. In particular, power distribution networks with periodic embodiments/loading are modeled using their equivalent two-dimensional TL networks and complex modes of such periodic networks are investigated. Transmission-line models, despite their limitations, are still fast and reasonably accurate. They're useful for gaining a qualitative insight into the problem of modeling electromagnetic fields in periodic structures. They offer an efficient means for analysis of printed-circuit periodic structures and can be easily integrated into circuit simulators. A major downside of these models is that they are typically tailored for specific types of unit cell geometries. TL modeling of more complex geometries such as the two-dimensional periodic array of dielectric rods shown in Fig. 2.8 is difficult and in some

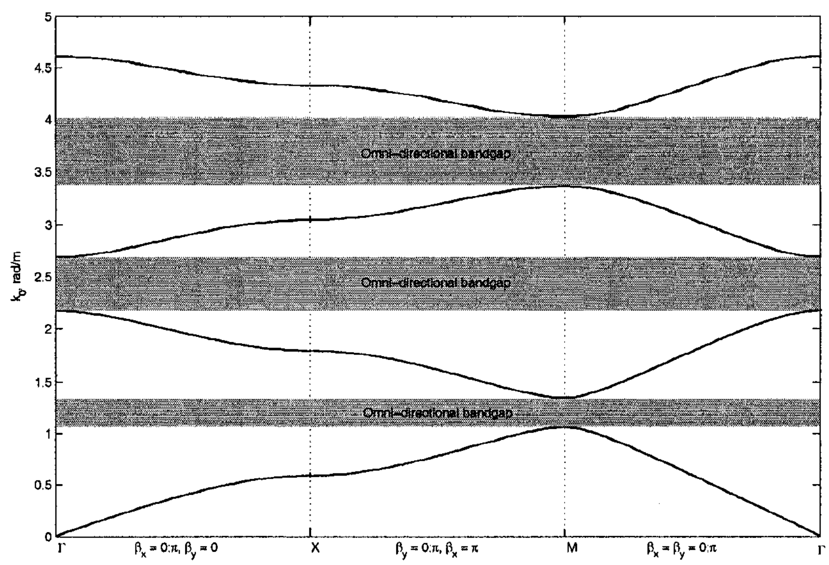

Fig. 2.7 Dispersion curves of the two-dimensional periodic array of air holes drilled in a dielectric medium with $\epsilon_r = 13$ and filling fraction $b/a = 0.25$.

cases, like three-dimensional periodic volumes, is impossible. Moreover, these models are only valid under certain assumptions and for specific fields configurations. Therefore, more accurate models are required which can be applied to a variety of unit cell geometries and are capable of capturing all the propagating modes of these structures. Accurate modeling of periodic structures calls for numerical methods that deal with the actual electromagnetic fields in the unit cell rather than the equivalent voltages and currents. These methods are briefly reviewed in the following section.

2.3 Field Analysis Techniques

CEM methods that are widely utilized for modeling the electromagnetic behavior of periodic structures are the transmission-line matrix method [40], the finite difference methods in both time (FDTD) [41] and frequency domains (FDFD) [42], the method of moments

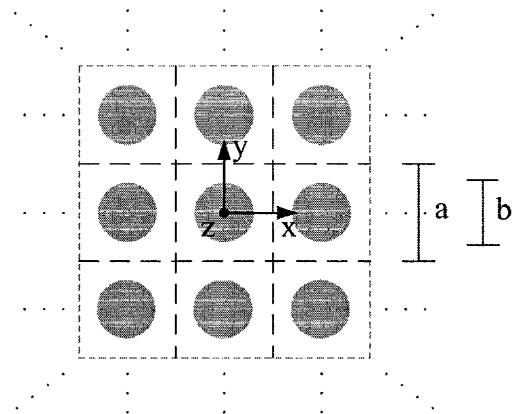

Fig. 2.8 Cross sectional view of two-dimensional array of dielectric rods of diameter b in a periodic square lattice with period a [34].

(MoM) [11] and the finite element (FE) method [12]. Depending on the architecture or the application of the structure, as well as the ease of implementation of the numerical model itself, a specific technique may be preferred in each particular case.

This section outlines two of the mostly used techniques for numerical modeling of electromagnetic fields in infinite periodic structures: the finite-difference time-domain method and the finite element method. The FDTD method directly simulates the time evolution of the characteristic equation of the problem. The FEM solves for the time harmonic eigenmodes, i.e. the dispersion relation in the frequency domain. A more complete survey of the CEM techniques for periodic modeling may be found in [43].

2.3.1 Finite-Difference Time-Domain Method

The finite-difference time domain method solves Maxwell's equations by discretizing them in both time and space. Yee [44] first introduced this novel approach of replacing Maxwell's equations with finite difference equations. Taflove [45] further developed this method and ever since its conception, the FDTD method has dramatically progressed and gained in popular use.

Many research works dealing with FDTD modeling of periodic dielectric materials and incorporation of periodic boundary conditions in this analysis technique have been published (see, e.g., [10, 46, 47, 48, 49]). To apply the FDTD procedure to periodic media, the problem domain is truncated to one unit cell of finite size. Then using an electric-field (**E**)

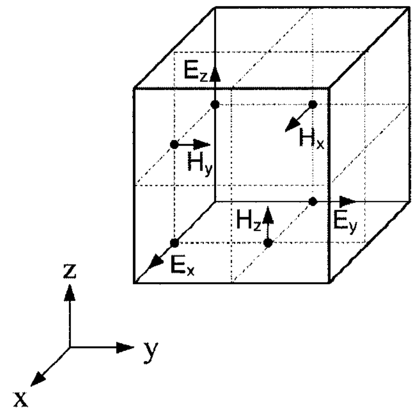

Fig. 2.9 Positions of the field components in a standard 3D Yee cell.

grid, which is offset both in space and time from a magnetic-field (**H**) grid (see Fig. 2.9), one obtains the update equations that yield the present fields (n^{th} time step) throughout the computational domain, in terms of the past fields ($n - 1^{\text{th}}$ time step). The update equations are used in a leap-frog scheme, to incrementally march the **E** and **H** fields forward in time [50].

Implementation of the time-domain periodic boundary conditions (PBCs) in the FDTD algorithm is not as trivial as the frequency-domain Floquet's constraints. Assuming a doubly periodic structure, the frequency domain PBC is given by

$$\mathbf{F}(x + a_x, y + a_y, \omega) = \mathbf{F}(x, y, \omega)e^{-j\beta_x a_x}e^{-j\beta_y a_y} \tag{2.23}$$

where a_x and a_y are the spatial periodicities in the x- and y-coordinate directions, respectively. When translated into the time-domain, the above condition becomes

$$F(x + a_x, y + a_y, t) = F(x, y, \frac{a_x}{v_{phx}} + \frac{a_y}{v_{phy}} + t) \tag{2.24}$$

The phase shifts $\beta_x a_x$ and $\beta_y a_y$ in (2.23) now become time shifts equal to the periodic dimensions divided by the appropriate phase velocities. A time shift can be modeled in the FDTD algorithm by storing a sufficient number of time samples of the fields at the periodic boundaries [47]. Therefore, the update equations for the fields on the slave surfaces of periodic boundary pairs (see Fig. 2.10) should be modified according to the fields on the master surfaces shifted forward in time.

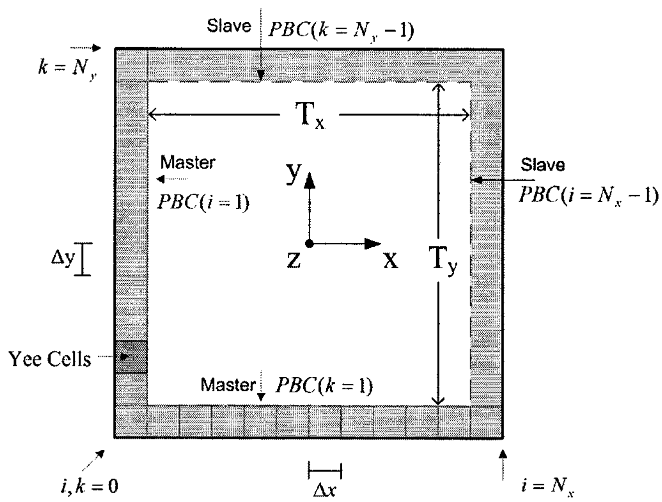

Fig. 2.10 Two-dimensional FDTD mesh for one periodic cell. Only one layer of Yee cells in both the x- and y-coordinate directions is shown.

FDTD is particularly well-suited to computing transient responses in periodic structures. It does that by illuminating the unit cell by a sinusoidal plane wave and recording the transient response. Eigen frequencies are then obtained by taking a fast Fourier transform (FFT) of the response; the peaks in the frequency spectrum correspond to eigen frequencies. Another advantage of FDTD is that it can easily handle complex, inhomogeneous geometries with anisotropic materials. Moreover, the resulting matrices from a FDTD analysis are sparse, structured matrices that can be solved efficiently by iterative solvers [51].

Despite these advantages, there are major drawbacks to the FDTD method. One is the use of Cartesian grids that conform poorly to curved geometries and introduce the so-called staircase error. The other is the spatial displacement of the **E** and **H** grids in a FDTD discretization which makes the implementation of the boundary conditions difficult and brings up the stability constraints. In general, the FDTD method cannot be used for simulations with strict accuracy constraints owing to the approximation errors introduced by the finite difference operators [51]. Another drawback, particularly relevant to the present thesis, is that with the FDTD method it would not be possible to treat the propagation constant as an unknown since it results in update equations involving future (unknown) field values [17].

2.3.2 Finite Element Method

When it comes to computing steady-state responses in electromagnetics, the finite element method (FEM) is preferred to the method of finite differences. FEM is a popular numerical modeling technique that can be applied to any boundary value problem. FEM was first applied to electromagnetic problems in 1968 [52] and since then the method has been employed in diverse areas of electromagnetics such as antennas, microwave circuits and scattering applications [53].

FE techniques usually deal with a variational formulation (or equivalently a weighted residual) of the governing differential equation. The stationary point of the variational formulation yields the solution to the boundary value problem. It is obtained by discretizing the problem domain into small subdomains (finite elements) and then approximating the unknown variable over each finite element using subdomain expansion functions.

A number of Flouquet-based FEM analyses of periodic structures have been reported in the literature [54, 55, 56, 57, 58, 12]. Incorporation of the frequency-domain periodic boundary conditions (e.g. Eq. (2.23)) in the FEM is straight forward. PBCs are introduced to the discretized form of the functional (residual) by modifying the expansion coefficients (unknowns of the system of equations) associated with the subdomain regions that lie on the periodic boundary pairs. Indeed, the unknown coefficients for a slave surface are determined from their counterparts on the master surface (see Fig. 2.11). Therefore, slave unknowns can be eliminated from the system of equations, provided their contribution is accounted for in the system through master unknowns.

There are advantages and disadvantages associated with the FEM. Firstly, the FE matrices tend to be less sparse and structured than those produced by the FDTD approach. Furthermore, in the FEM, a matrix must be inverted. Current linear-algebra technology limits the size of the matrix that can be inverted and, thus, limits the number of unknowns that the FEM can handle. On the other hand, the FEM, regardless of its implementation challenges, bears several advantages in terms of flexibility and accuracy over the FDTD method. The FEM can easily model inhomogeneous materials bounded by curved surfaces and it avoids the staircasing error introduced in standard finite difference methods. Moreover, with FEM, the eigen frequencies are directly obtained from the resulting eigenvalue equation and therefore no postprocessing of the data (such as the Fourier transforms required in FDTD method) is involved.

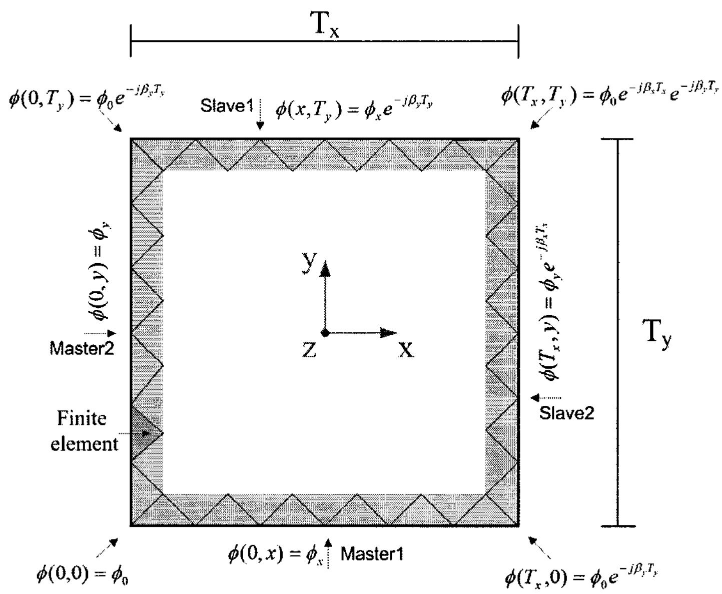

Fig. 2.11 Two-dimensional FEM mesh for one periodic cell. Only one layer of triangular elements in both the x- and y-coordinate directions is shown.

Concluding, for the particular modeling problem presented in this thesis, the FE method has been chosen. The deciding factor for this choice has been that various experiments on the frequency-selective features of periodic structures are carried out in the frequency-domain much easier than the time-domain. Moreover, the goal here is, in particular, the treatment of the stopband behavior and, in general, extraction of complex propagation constants. This information cannot be extracted from a field analysis of a unit cell of a periodic structure with FDTD at all while it can be easily obtained using FEM. A complete treatment of the finite element modeling of complex eigenmodes in periodic structures is presented in Chapter 4.

Chapter 3

Transmission-Line Modeling

Periodic structures that operate in the microwave range of the electromagnetic spectrum are commonly composed of arrays of metal patches [59], or aperture elements within a metallic screen [60], patterned on a grounded dielectric substrate. Such geometries are generally referred to as metallo-dielectric electromagnetic bandgap structures and can be analyzed using equivalent transmission-line models.

Due to the ease of implementation in printed-circuit technology, EBG structures are increasingly used in PDNs of high-speed circuits for global suppression of simultaneous switching noise (SSN). Such applications have directed much attention to the bandgap behavior of these structures. Indeed, prediction of the insertion loss in the bandgap along with dispersion characteristics has become an important part of their design process.

Primarily, the transverse resonance technique (TRT) was used to determine the dispersion characteristics of a parallel-plate waveguide (PPW) with an EBG surface replacing one of the conductor plates [20]. This technique predicts an approximate 1D dispersion diagram. 1D transmission-line model for such covered EBG structure was introduced in [61, 62]. This model assumes that the propagation of electromagnetic waves is only along one principal axis and uses a lumped-element equivalent circuit to represent the EBG structure. This single stage lumped-element model is a modification of the effective sheet impedance model originally proposed by Sievenpiper in [27] for the mushroom-type EBG configurations. In these analytical and modeling approaches no explicit information about the 2D nature of excitation of the periodic structure is included. Therefore, a complete analysis for all possible directions of signal propagation has not yet been realized.

The focus of this chapter is on 2D transmission-line modeling of microwave periodic structures which allows for stopband characterization of periodic structures in all azimuthal directions. The TL model employs a 2D network of transmission-line section that are periodically loaded by lumped L–C components. § 3.1 briefly overviews the theory of operation for 2D periodic TL networks. Complex eigenmode analysis of such electrical networks is discussed in this section. The TL model has been shown to be capable of capturing evanescent modes and predicting the stopband behavior of periodic structures. Simulation results for a number of representative EBG structures are presented in § 3.2. Complex propagation constants along arbitrary directions of propagation are plotted versus frequency. The results confirm the capability of the developed TL model in modal characterization of the periodic structures at all frequencies and in particular the attenuation behavior in the bandgap regions. § 3.3 discusses the extraction of insertion loss information from attenuation diagrams.

3.1 Theory of TL modeling

Grbic and Eleftheriades [14] proposed the modal analysis of 2D transmission-line structures with periodic L–C loadings. They employed Bloch analysis to examine the propagation characteristics of a 2D negative refractive index (NRI) transmission-line structure. In [15], Caloz and Itoh presented a 2D anisotropic metamaterial, exhibiting positive refractive index (PRI) in one direction and NRI in the orthogonal direction using a similar TL model.

The dispersion analyses presented in both [14, 15] follow the same approach given in Chapter 2, i.e. a purely imaginary propagation vector ($\boldsymbol{\gamma} = j\boldsymbol{\beta} = j\beta_x\hat{x} + j\beta_y\hat{y}$) is specified and the frequency solutions (k_0) are sought. The band structure and thus the propagating modes of the TL network are easily found this way by plotting $k - \beta$ diagrams. However, this approach does not let the propagation constant (γ) be treated as an unknown of the characteristic equation. Therefore, modes of the form $\boldsymbol{\gamma} = \boldsymbol{\alpha}$ (evanescent modes) or in general $\boldsymbol{\gamma} = \boldsymbol{\alpha} + j\boldsymbol{\beta}$ (complex modes) cannot be captured.

In the methodology presented here, frequency is specified and the characteristic equation is solved for the complex propagation constants ($\gamma_x = \alpha_x + j\beta_x, \gamma_y = \alpha_y + j\beta_y$). Thus, all the propagating ($\boldsymbol{\gamma} = j\boldsymbol{\beta}$), the evanescent ($\boldsymbol{\gamma} = \boldsymbol{\alpha}$) or even the complex ($\boldsymbol{\gamma} = \boldsymbol{\alpha} + j\boldsymbol{\beta}$) modes of the structure can be found. The band diagrams and the attenuation diagrams are then obtained by plotting the imaginary and real parts of $\boldsymbol{\gamma}$ versus frequency.

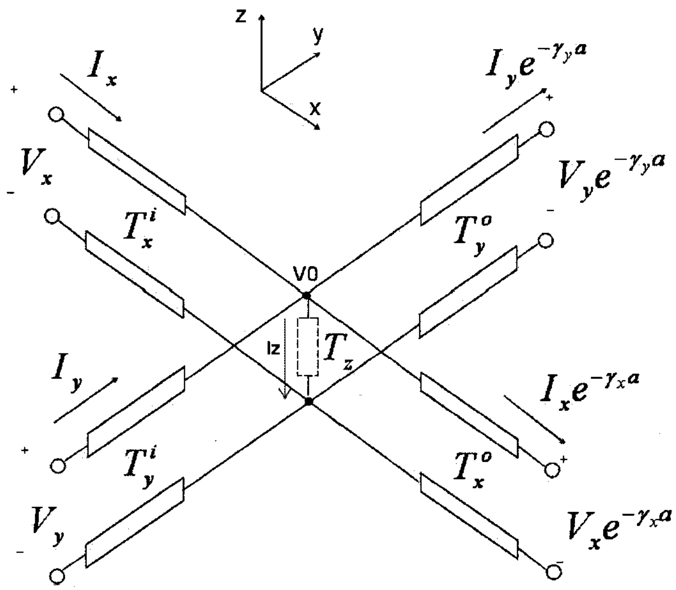

Fig. 3.1 The network representation of the unit cell of a 2D TL periodic structure. Each branch is denoted by its transmission matrix T = [ABCD].

3.1.1 Characteristic Equation

As explained in § 2.2, the transmission-line analysis of such periodic structures involves constructing an equivalent TL circuit for a unit cell of the structure. Thereafter, the Bloch theorem is applied to the voltages and currents at the terminals of the unit cell to obtain the characteristic equation of the structure. The γ solutions of the characteristic equation thus determine the waves that may propagate along the cascade connection of the basic cells.

An equivalent transmission-line model for a unit cell of a 2D periodic structure is shown in Fig. 3.1 where each TL branch is represented by its ABCD transfer matrix labeled T_x^i, T_x^o, T_y^i and T_y^o. The overall structure can be viewed as an infinite array of unit cells in both x and y directions. In general, the TL branches are loaded transmission-line sections where the loading may be represented by either series and/or parallel lumped components or transmission-line sections with different characteristics impedance or a combination of both. In either case, the loading effect is accounted for in the overall transfer matrix of the branch. At their intersection, the two ladder TL networks can also share a common parallel component which is represented by its transfer matrix $T_z = [\text{ABCD}]_z$.

Applying Bloch boundary conditions to the voltages and currents at the four ports of the unit cell, along with Kirchhoff's voltage and current laws at the intersection yields the following system of linear equations, as suggested in [14, 15]:

$$V_0 = \frac{D_x^i V_x - B_x^i I_x}{A_x^i D_x^i - B_x^i C_x^i} \tag{3.1a}$$

$$V_0 = \frac{D_y^i V_y - B_y^i I_y}{A_y^i D_y^i - B_y^i C_y^i} \tag{3.1b}$$

$$V_0 = \left(A_x^o V_x + B_x^o I_x\right) e^{-\gamma_x a} \tag{3.1c}$$

$$V_0 = \left(A_y^o V_y + B_y^o I_y\right) e^{-\gamma_y a} \tag{3.1d}$$

$$V_0 = -\frac{B_z I_z}{A_z D_z - B_z C_z} \tag{3.1e}$$

$$\begin{aligned}\sum_{n=1}^{5} I_n = {} & \frac{A_z I_z}{A_z D_z - B_z C_z} + \frac{-C_x^i V_x + A_x^i I_x}{A_x^i D_x^i - B_x^i C_x^i} + \frac{-C_y^i V_y + A_y^i I_y}{A_y^i D_y^i - B_y^i C_y^i} \\ & - \left(C_x^o V_x + D_x^o I_x\right) e^{-\gamma_x a} - \left(C_y^o V_y + D_y^o I_y\right) e^{-\gamma_y a} = 0 \end{aligned} \tag{3.1f}$$

Eliminating I_z and V_0, the above set of equations reduces to

$$\left(\frac{D_x^i}{\Delta_x^i} - A_x^o e^{-\gamma_x a}\right) V_x - \left(\frac{B_x^i}{\Delta_x^i} + B_x^o e^{-\gamma_x a}\right) I_x = 0 \tag{3.2a}$$

$$\left(\frac{D_y^i}{\Delta_y^i} - A_y^o e^{-\gamma_y a}\right) V_y - \left(\frac{B_y^i}{\Delta_y^i} + B_y^o e^{-\gamma_y a}\right) I_y = 0 \tag{3.2b}$$

$$(A_x^o e^{-\gamma_x a}) V_x + (B_x^o e^{-\gamma_x a}) I_x - (A_y^o e^{-\gamma_y a}) V_y - (B_y^o e^{-\gamma_y a}) I_y = 0 \tag{3.2c}$$

$$\begin{aligned} & \left(\frac{C_x^i}{\Delta_x^i} + C_x^o e^{-\gamma_x a} + \frac{A_z}{B_z}\frac{D_x^i}{\Delta_x^i}\right) V_x + \left(\frac{C_y^i}{\Delta_y^i} + C_y^o e^{-\gamma_y a}\right) V_y \\ - & \left(\frac{A_x^i}{\Delta_x^i} - D_x^o e^{-\gamma_x a} + \frac{A_z}{B_z}\frac{B_x^i}{\Delta_x^i}\right) I_x - \left(\frac{A_y^i}{\Delta_y^i} - D_y^o e^{-\gamma_y a}\right) I_y = 0 \end{aligned} \tag{3.2d}$$

where $\Delta_k^i = A_k^i D_k^i - B_k^i C_k^i$, $(k = x, y)$. Further simplifications are obtained if the networks representing the series branches are reciprocal, where $\Delta_k^i = 1$ [28] and

$$\begin{cases} A_k = A_k^i = D_k^o \\ B_k = B_k^i = B_k^o \\ C_k = C_k^i = C_k^o \\ D_k = D_k^i = A_k^o, \qquad \text{for} \quad k = x, y \end{cases} \tag{3.3}$$

In that case, Eq. (3.2) can be rewritten in matrix form as

$$(\mathbf{M}) \begin{pmatrix} V_x \\ I_x \\ V_y \\ I_y \end{pmatrix} = \begin{pmatrix} a_x & b_x & 0 & 0 \\ 0 & 0 & a_y & b_y \\ f_x & g_x & -f_y & -g_y \\ h_x & i_x & c_y & d_y \end{pmatrix} \begin{pmatrix} V_x \\ I_x \\ V_y \\ I_y \end{pmatrix} = \underline{0} \tag{3.4}$$

where the elements of $\mathbf{M}$ are given at the bottom of the page[1]. Nontrivial solutions of Eq. (3.4) can then be found by setting the determinant of $\mathbf{M}$ to zero which yields the dispersion equation. The dispersion equation for networks with reciprocal series branches, is given by

$$P_y \cosh \gamma_x a + P_x \cosh \gamma_y a = R \tag{3.6}$$

where

$$R = P_x(1 + 2Q_y) + P_y(1 + 2Q_x) + P_x P_y \frac{A_z}{B_z} \tag{3.7}$$

with

$$\begin{cases} P_k = B_k D_k \\ Q_k = B_k C_k \ , \qquad \text{for} \quad k = x, y. \end{cases} \tag{3.8}$$

In Eq. (3.6), P_x, P_y, and R are explicitly known in terms of frequency and γ_x, γ_y are unknown functions of frequency. One way to treat Eq. (3.6) is to specify a propagation

---

1

$$\begin{array}{ll} a_k = D_k(1 - e^{-\gamma_k a}) & f_k = D_k - a_k \\ b_k = -B_k(1 + e^{-\gamma_k a}) & g_k = -B_k - b_k \\ c_k = C_k(1 + e^{-\gamma_k a}) & h_k = \frac{A_z}{B_z} D_k + c_k \\ d_k = -A_k(1 - e^{-\gamma_k a}) & i_k = -\frac{A_z}{B_z} B_k + d_k \end{array} \tag{3.5}$$

vector ($\boldsymbol{\gamma} = j\boldsymbol{\beta} = j\beta_x\hat{x} + j\beta_y\hat{y}$) and find the frequency solutions of the admitted modes [14, 15]. In fact, specifying a propagation vector, the dispersion equation reduces to a nonlinear equation in terms of frequency which can be numerically solved using mathematic software (e.g. MATLAB). On the other hand, given a frequency, the propagation vector $\boldsymbol{\gamma}$ can be treated as an unknown of the equation. The latter approach, which we are more interested in, allows us to find complex modes of the periodic structure. For a specified frequency and a direction of propagation, complex modes are obtained by solving the nonlinear equation in terms of propagation constant γ, as discussed in the next section.

3.1.2 Solution of the Characteristic Equation

Let $\hat{r} = \cos\phi\hat{x} + \sin\phi\hat{y}$ be the unit vector along an arbitrary direction where ϕ denotes the angle that $\hat{r}$ forms with the x-axis. For any propagation vector $\boldsymbol{\gamma} = \gamma\hat{r}$ along that direction one may write

$$\boldsymbol{\gamma} = \gamma\hat{r} = \underbrace{\gamma\cos\phi}_{\gamma_x}\,\hat{x} + \underbrace{\gamma\sin\phi}_{\gamma_y}\,\hat{y} \tag{3.9}$$

which constraints γ_x and γ_y by

$$\frac{\gamma_x}{\cos\phi} = \frac{\gamma_y}{\sin\phi} = \gamma \tag{3.10}$$

Therefore, Eq. (3.6) can be rewritten in terms of scalar γ as

$$P_y\cosh(\gamma a\cos\phi) + P_x\cosh(\gamma a\sin\phi) - R = 0 \tag{3.11}$$

Eq. (3.11) is now ready to be treated with MATLAB as a nonlinear equation in terms of γ, once frequency (f) and direction of wave propagation ($\hat{r}$) are specified. Obviously, all the unique directions of propagation within the irreducible Brillouin zone of the square lattice (the shaded area in Fig. 3.2) should be inspected to completely determine the complex eigenmodes of the periodic structure. However, as explained in § 2.2.2, sweeping the edges of the zone provides the band structure and predicts the attenuation along certain directions. Therefore, the only directions which are examined here correspond to the edges of the irreducible Brillouin zone, as follows.

Γ–X line is for modes directed along the x-axis with $\boldsymbol{\gamma} = \gamma_x\hat{x} + 0\hat{y}$; i.e., $\hat{r} = \hat{x}$ and γ_y is

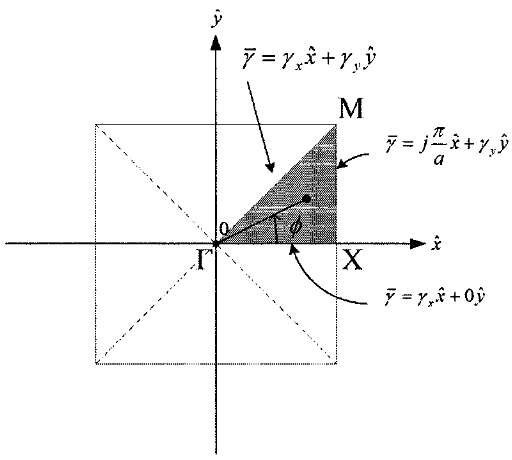

Fig. 3.2 γ constraints on the edges of the irreducible Brillouin zone of the symmetric square lattice with lattice constant a.

forced to 0 ($\alpha_y = \beta_y = 0$). Therefor Eq. (3.6) reduces to

$$\cosh \gamma_x a = \frac{R - P_x}{P_y} \tag{3.12}$$

which can be solved for γ_x as a function of frequency. X–M line is for modes of the form $\gamma = \frac{j\pi}{a}\hat{x} + \gamma_y\hat{y}$; that is γ_x is set to $0 + j\frac{\pi}{a}$ ($\alpha_x = 0$, $\beta_x a = \pi$) or equivalently γ is constrained to vectors with $|\gamma a \cos\phi| = \pi$, and $0 \leq \sin\phi \leq \frac{1}{\sqrt{2}}$. Thus, Eq. (3.6) becomes

$$\cosh \gamma_y a = \frac{R + P_y}{P_x} \tag{3.13}$$

which is solved for γ_y likewise. Finally, M–Γ is for the propagation direction of $\hat{r} = \frac{\hat{x}+\hat{y}}{\sqrt{2}}$, and γ_x is set equal to γ_y yielding

$$\cosh \gamma_x a = \cosh \gamma_y a = \frac{R}{P_x + P_y} \tag{3.14}$$

Therefore, Eq. (3.11) once inspected on the edges of the irreducible Brillouin zone, is expected to predict the band structure of the propagating modes while providing the attenuation constant of the evanescent modes within the forbidden frequency regions. At each frequency, the real and the imaginary parts of the complex propagation constant γ yield the attenuation and the phase constant of the corresponding mode, respectively.

3.2 Simulation Models and Results

The formulation presented in § 3.1 can be easily applied to a variety of metallo-dielectric EBG structures. This section presents simulation results for a number of EBG structures that are particularly employed in power distribution networks. The first structure considered is the mushroom-type EBG structure. The second example investigates the mushroom EBG once it is embedded in a parallel-plate waveguide. Lastly, an array of interconnected metallic patches patterned on a grounded dielectric substrate is examined. For each model, complex propagation constants along different directions of propagation are obtained. Plots of the real and imaginary parts of the propagation constant are presented which characterize the passband and stopband behavior of the periodic structures.

3.2.1 Mushroom Structure

Sievenpiper *et al.* [27] originally used the mushroom structure in low-profile antenna designs to improve the gain and directivity of the antenna. Later in [20], Abhari and Eleftheriades employed this structure to suppress the power/ground noise induced in a parallel-plate power distribution network.

The mushroom EBG structure is shown in Fig. 3.3(a). It consists of a lattice of metal patches, connected to a solid metal sheet by conducting vias. An equivalent transmission-line model of the unit cell of the structure is also depicted in Fig. 3.3(b). This model assumes strong field concentration in the dielectric substrate, below metallic patches, and neglects the fields penetrating into the open region. The fringing field between patches is accounted for by the series capacitors shown in Fig. 3.3(b). The resulting series impedance $z_1 = \frac{1}{j\omega 2C_g}$, thus, represents the gap between the patches. It is cascaded to a TL section of length $d = \frac{w}{2}$ with characteristic impedance of Z_d and propagation constant of $\gamma_d = j\beta_d$. The TL section represents the parallel-plate transmission line formed by each patch and the lower ground plane. Multiplying the transfer matrices of z_1 and the TL section yields the overall [ABCD] matrix of the series branch. Furthermore, the via at the center of each patch is modeled by a single impedance $z_2 = j\omega L_v$. With z_1 and z_2 normalized to the characteristic impedance of the TL sections, the transmission matrices of the series and

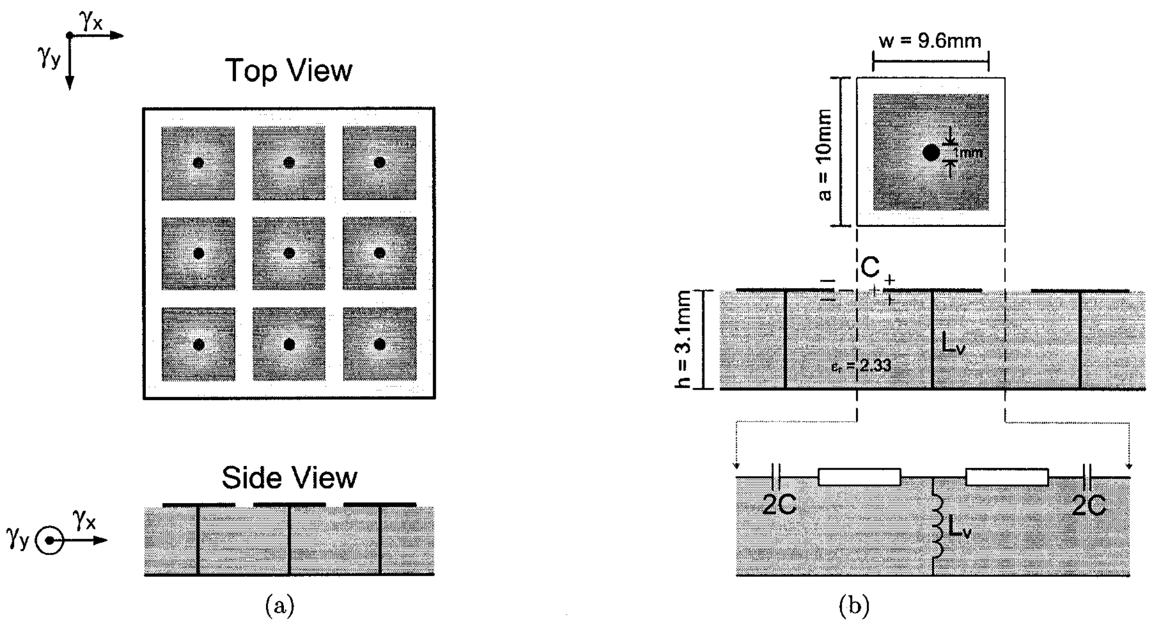

Fig. 3.3 The mushroom-type EBG structure: (a) top view and side view, (b) equivalent transmission-line model of one unit cell of the structure.

shunt branches are given by

$$T_{\text{series}} = \begin{bmatrix} \cos\beta_d d + j\bar{z}_1 \sin\beta_d d & j\sin\beta_d d + \bar{z}_1\cos\beta_d d \\ j\sin\beta_d d & \cos\beta_d d \end{bmatrix} \tag{3.15}$$

$$T_{\text{shunt}} = \begin{bmatrix} A_z & B_z \\ C_z & D_z \end{bmatrix} = \begin{bmatrix} 1 & \bar{z}_2 \\ 0 & 1 \end{bmatrix} \tag{3.16}$$

Note that the series branches are represented by reciprocal networks, therefore Eq. (3.6) along with Eqns. (3.15), (3.16) yield the following dispersion equation for the mushroom structure

$$\cosh\gamma_x a + \cosh\gamma_y a = (2 + \frac{\bar{z}_1}{2\bar{z}_2})\cos\beta_d w + j(2\bar{z}_1 + \frac{1}{2\bar{z}_2})\sin\beta_d w + \frac{\bar{z}_1}{2\bar{z}_2} \tag{3.17}$$

The characteristic impedance and propagation constant of the TL sections are those of a lossless parallel-plate transmission line, given by

$$Z_d = \frac{\eta_0}{\sqrt{\epsilon_r}} \frac{h}{w}$$
$$\gamma_d = j\beta_d = j\frac{\omega}{c}\sqrt{\epsilon_r} \tag{3.18}$$

where η_0 is the characteristic impedance of free space (377Ω), c is the speed of light in vacuum, ϵ_r is the relative permittivity of the substrate and ω is the radian frequency. Moreover, the values of L_v and C_g are obtained using approximate formulas [61, 63, 64]

$$C_g = \frac{w\epsilon_0(1+\epsilon_r)}{\pi} \cosh^{-1}(\frac{2w}{g}) \tag{3.19}$$
$$L_v = \frac{\mu h}{4\pi}(\log(\frac{1}{q}) + q - 1) \tag{3.20}$$

with

$$q = \pi \left(\frac{r}{a}\right)^2 \tag{3.21}$$

where w is the width of the patches, g is the gap between patches, r is the radius of the cylindrical vias, h is the thickness of the dielectric substrate and a is the lattice constant.

Initially, the developed formulation was applied to the loaded transmission-line geometry presented in [14] for validation purposes and identical dispersion diagram was obtained. In this thesis that the parallel-plate PDNs are discussed the EBG structure shown in Fig. 3.3(a) is analyzed since it has been previously employed in the design of PDNs [20].

Two sets of experiments were carried out. In the first set of numerical experiments, the propagation vector β was specified and the frequency solutions (f) were obtained. Fig. 3.4 shows the band structure obtained from this analysis. Each region of Fig. 3.4 corresponds to a distinct set of phase constants (β_x,β_y). As seen in the figure, there are three omni-directional stopbands within the plotted frequency range where the propagation of electromagnetic waves is forbidden for every possible direction.

In the second set of numerical solutions (Figs. 3.5– 3.7), frequency was specified and the propagation constants were found from Eqns. (3.12–3.14). Fig. 3.5(a) is a plot of the imaginary part of the propagation constant along the x-axis (γ_x) which corresponds to the Γ–X region of Fig. 3.4. Fig. 3.5(b) represents the real part of γ_x within the Γ–X region for the frequency range considered in Fig. 3.4. Fig. 3.6 corresponds to the X–M region and is a plot of the imaginary and real part of the complex propagation constant γ_y once $\gamma_x a$ is fixed to $j\pi$. Finally, Fig. 3.7 depicts the imaginary and real part of γ_x (γ_y) corresponding to the M–Γ region of the band diagram. In all three diagrams, the imaginary part of the complex propagation constants matches the respective region in the dispersion curves obtained from the first set of solutions.

The real part of the complex propagation constant in each region of the irreducible Brillouin zone represents the attenuation constant of the evanescent modes in the incurring stopbands. The unit of the horizontal axis in the attenuation diagrams is in Neper's since $\alpha_x a$ and $\alpha_y a$ parameters are plotted versus frequency. In other words, the attenuation diagram provides the decay rate per unit cell in Nepers. Stopbands exist when the attenuation constants α_x or α_y are nonzero. For instance, in the $\Gamma - X$ region, $\alpha_x \neq 0$ in the $0 - 1.56$, $2.81 - 3.3$ and $6.48 - 12$ GHz frequency bands (evanescence regions), while in the $1.56 - 2.81$ and $3.3 - 6.48$ GHz frequency bands it equals to zero (propagation regions). In the $X - M$ region, $\alpha_y \neq 0$ in the $0 - 1.25$, $1.56 - 6.48$ and $10.24 - 12$ GHz frequency

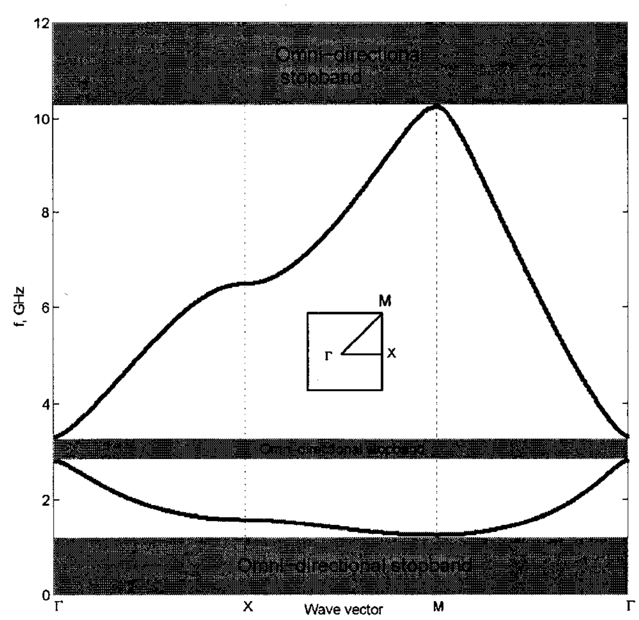

Fig. 3.4 Dispersion curves of the mushroom-type EBG structure of Fig. 3.3(b)

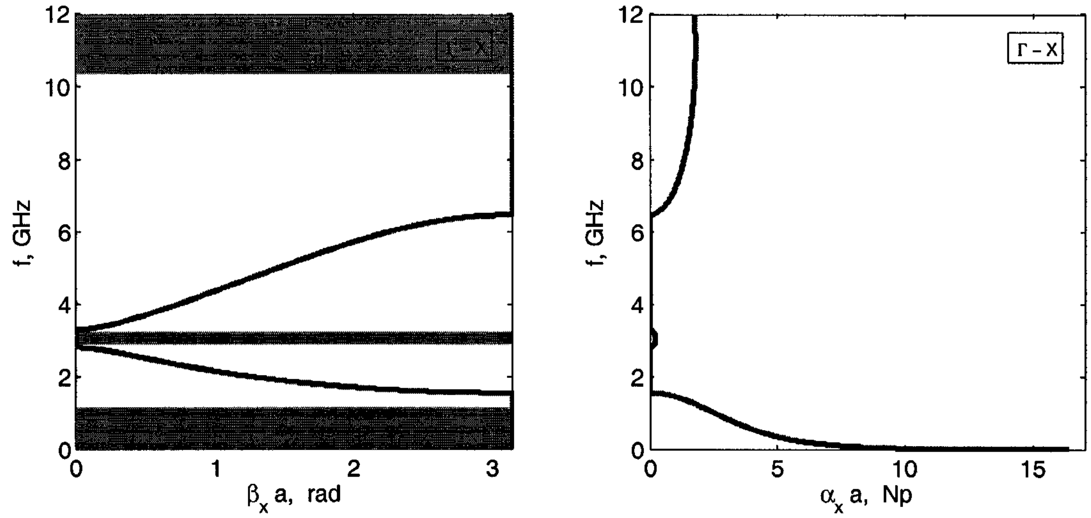

Fig. 3.5 Complex propagation constant of the mushroom structure in region Γ–X: (a) imaginary part, and (b) real part.

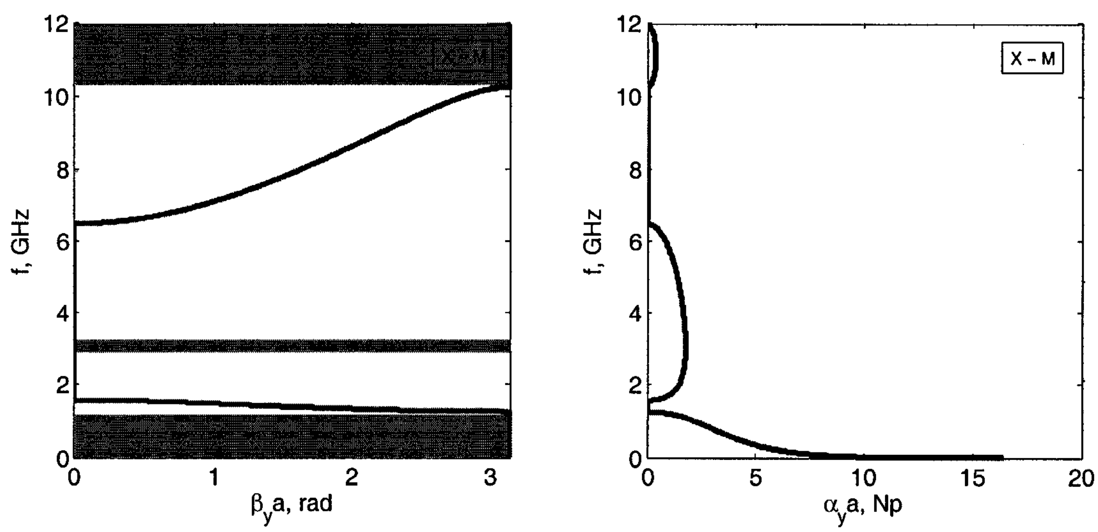

Fig. 3.6 Complex propagation constant of the mushroom structure in region X–M: (a) imaginary part, and (b) real part.

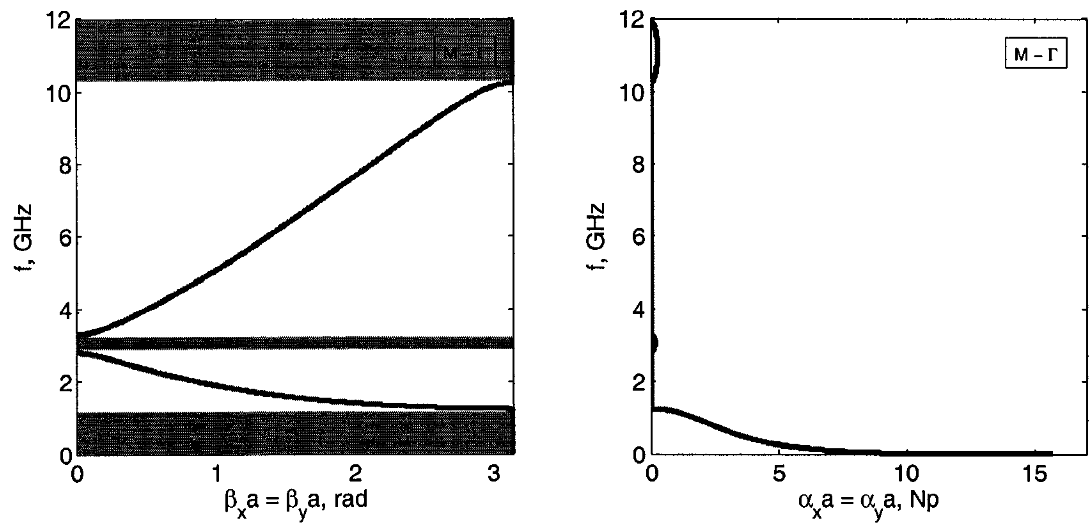

Fig. 3.7 Complex propagation constant of the mushroom structure in region M–Γ: (a) imaginary part, and (b) real part.

bands (evanescence regions) and it equals to zero in the $1.25 - 1.56$ and $6.48 - 10.24$ GHz frequency bands (propagation regions). Finally, in the $M - \Gamma$ region, α_x and α_y are both nonzero in the $0 - 1.25$, $2.81 - 3.3$ and $10.24 - 12$ GHz frequency bands (evanescence regions) and $\alpha_x = \alpha_y = 0$ in the $1.25 - 2.81$ and $3.3 - 10.24$ GHz frequency bands (propagation regions). It should be noted here that in the omnidirectional stopbands α_x and α_y are simultaneously nonzero, namely the $0 - 1.25$, $2.81 - 3.3$ and $10.24 - 12$ GHz ranges.

3.2.2 Shielded Mushroom Structure

The next example considered was a PDN containing an EBG structure, that is a PDN with textured ground plane. Fig. 3.8(a) shows the EBG structure of Fig. 3.3(a) once incorporated in the PDN of an electronic circuit. The top plate of the PDN is isolated from the embedded EBG structure by a dielectric layer of thickness t_1 and dielectric constant ϵ_{r1}. Therefore, the host parallel-plate medium is composed of two dielectric layers, with the lower layer containing the conductive vias. The lower layer has a thickness of t_2 and a dielectric constant of ϵ_{r2}. As shown in [61], the most broad-band performance is achieved when $t_1 \ll t_2$ and $\epsilon_{r1} \gg \epsilon_{r2}$.

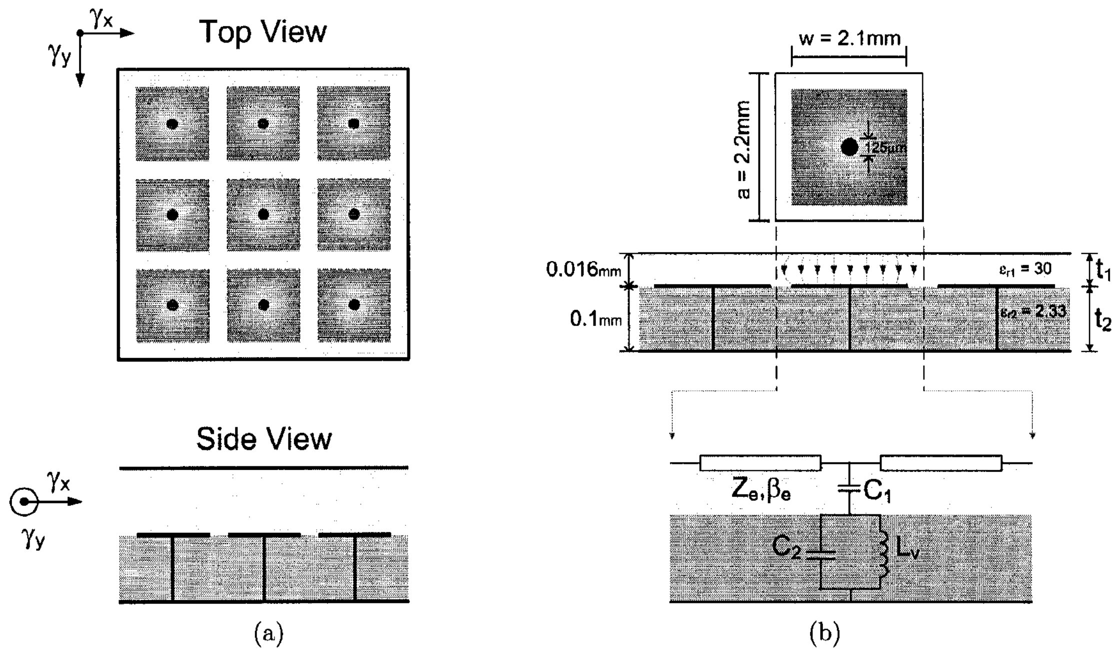

Fig. 3.8 The mushroom EBG structure embedded in parallel-plate power planes: (a) top view and side view, (b) equivalent transmission-line model of one unit cell of the structure.

In this configuration, the top and the bottom solid conductor planes form an inhomogeneously filled PPW in which the dominant mode is identified as a longitudinal section magnetic (LSM)[2] mode [3]. This lowest order quasi-TEM mode can be modeled by a simple transmission-line with an effective dielectric constant of

$$\epsilon_{r,e} = \frac{t_1 + t_2}{\frac{t_1}{\epsilon_{r1}} + \frac{t_2}{\epsilon_{r2}}} \tag{3.22}$$

as suggested in [61]. An equivalent transmission-line model of one unit cell of the structure is shown in Fig. 3.8(b). The characteristic impedance and the phase constant of the TL sections are given by Eq. (3.18) along with the ϵ_r obtained from Eq. (3.22). The parallel

[2]Hybrid TM_z modes also referred to as LSM modes have no axial (z-directed) magnetic field component.

plates are periodically loaded with a lumped impedance of

$$z_2 = \frac{1}{j\omega C_1} + \frac{1}{j\omega C_2 + \frac{1}{j\omega L_v}} \tag{3.23}$$

representing the EBG structure. The patches and the vias of the EBG structure are modeled by a shunt L–C branch. The value of L_v is obtained from Eq. (3.20) and the top and the bottom capacitances, C_1 and C_2, are approximated by parallel-plate capacitors. With z_1 set to 0 (since there's no discontinuity in the top shield), Eq. (3.17) reduces to

$$\cosh \gamma_x a + \cosh \gamma_y a = 2 \cos \beta_e a + \frac{j}{2\bar{z}_2} \sin \beta_e a \tag{3.24}$$

resulting in the band diagram of the modified PDN.

Again two sets of numerical experiments were carried out. Firstly, propagating modes of the structure were obtained by specifying $\boldsymbol{\beta}$ vectors and finding frequency solutions. Fig. 3.9 presents the $k - \beta$ diagrams obtained for the modified PDN of Fig. 3.8(a). As shown in the figure, a stopband is induced over the frequency range 2.47 – 13.23 GHz. Achievement of such a wide bandgap is an important feature for noise suppression in modern broadband electronic applications.

Next, the complex modes of the modified PDN are obtained by specifying frequency and finding $\boldsymbol{\gamma}$ solutions (see Figs. 3.10– 3.12). As expected, the imaginary part of the complex γ (Figs. 3.10– 3.12) perfectly matches the corresponding region of the dispersion diagram shown in Fig. 3.9. The other useful engineering plots are the attenuation diagrams of Figs. 3.10(b) – 3.12(b) which represent the attenuation per unit cell along different directions of excitation. The attenuation constants α_x and α_y are of primary interest herein, since the EBG structure is employed to suppress the switching noise in the PDN by inducing an omni-directional wide stopband. Moreover, these graphs can be used to qualitatively investigate port isolation and insertion loss characteristics achieved by inserting the EBG in the parallel-plate configurations. The attenuation diagrams show that the maximum noise mitigation occurs at $f_0 = 2.785$ GHz within the Γ–X region with a value of 8.69 Neper/unit cell or −75 dB for one unit cell.

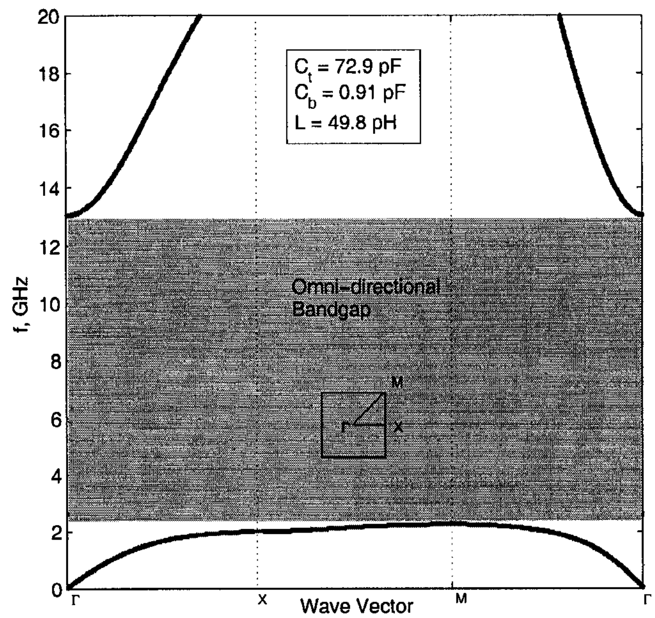

Fig. 3.9 Dispersion curves of the modified PDN with a textured ground plane of Fig. 3.8(b)

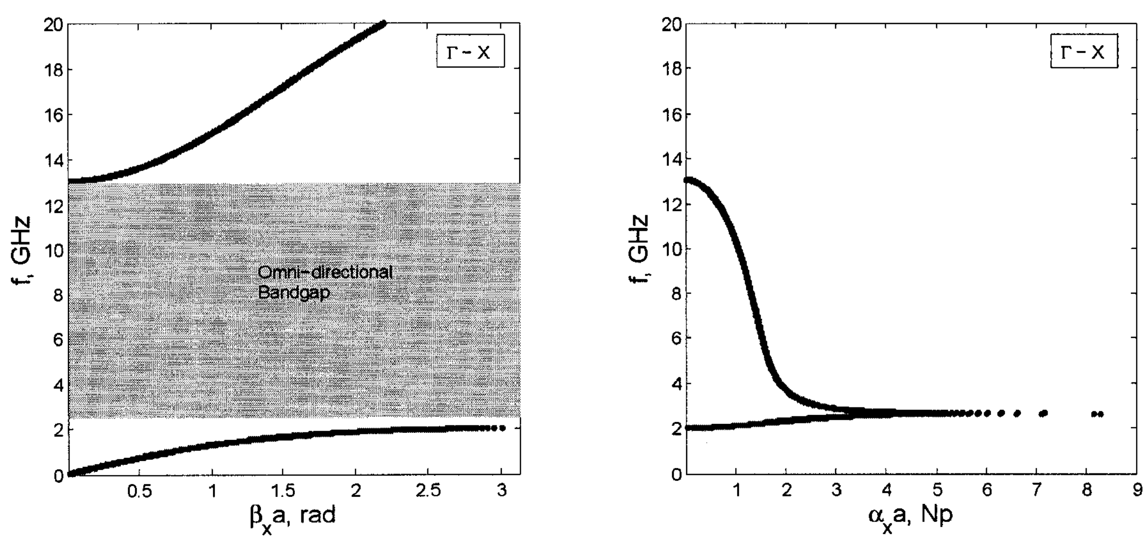

Fig. 3.10 Complex propagation constant of the shielded mushroom structure in region Γ–X: (a) imaginary part, and (b) real part.

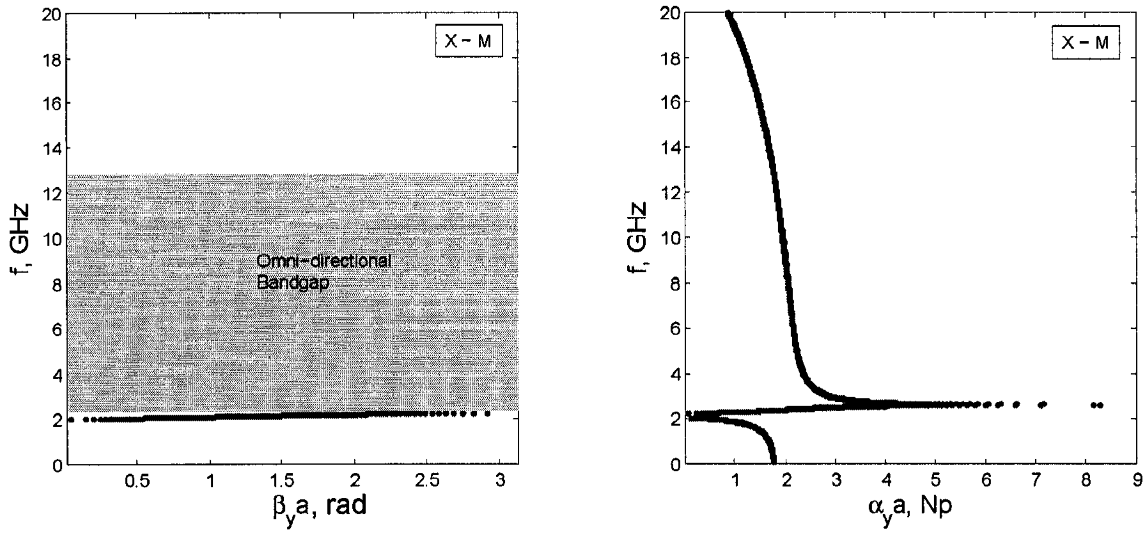

Fig. 3.11 Complex propagation constant of the shielded mushroom structure in region X–M: (a) imaginary part, and (b) real part.

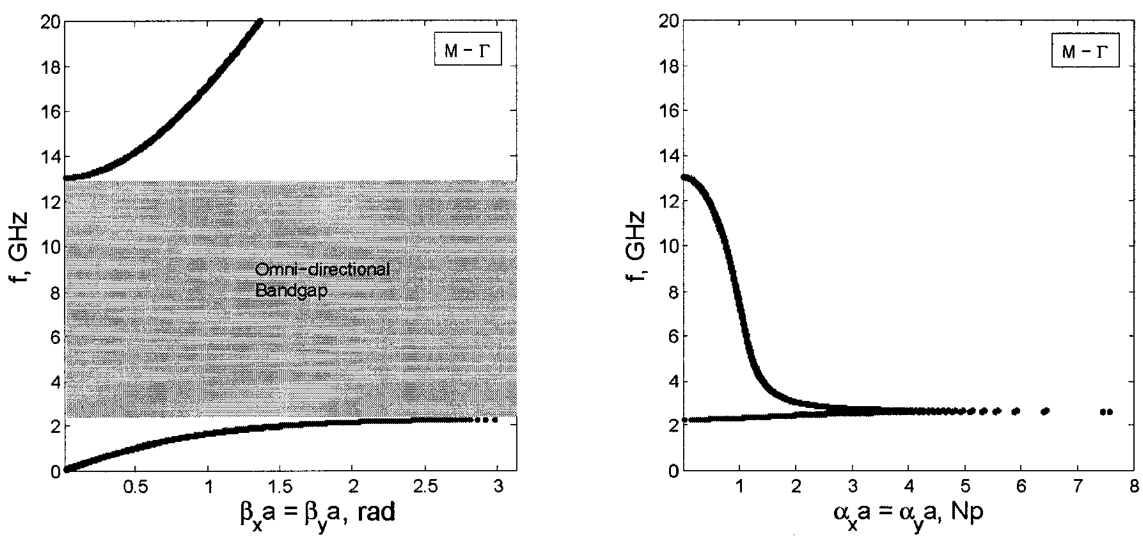

Fig. 3.12 Complex propagation constant of the shielded mushroom structure in region M–Γ: (a) imaginary part, and (b) real part.

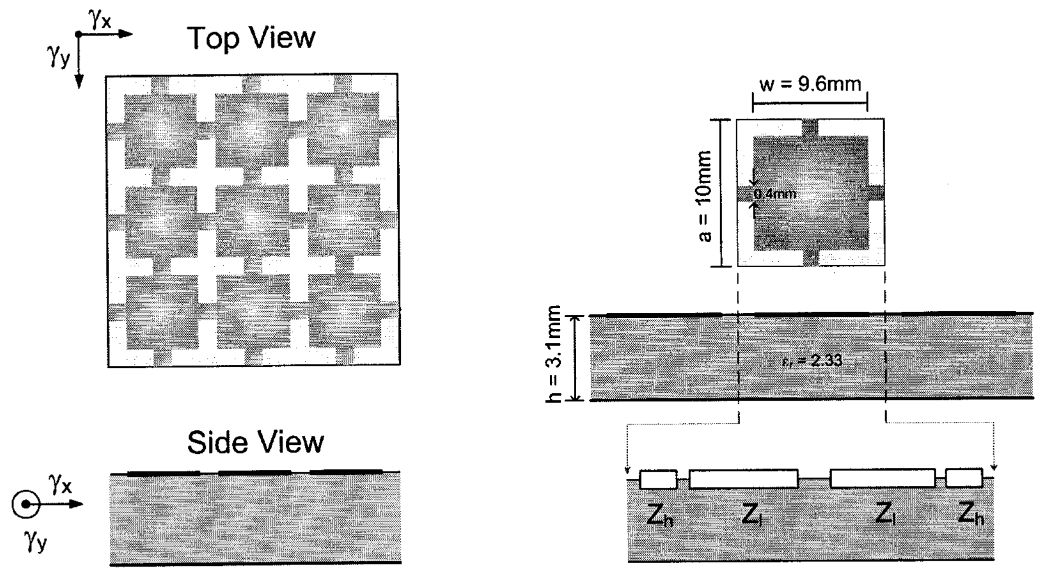

(a) (b)

Fig. 3.13 The PDN with a perforated power plane: (a) top view and side view, (b) equivalent transmission-line model of one unit cell of the structure.

3.2.3 PDN with Patterned Power Plane

Lastly, a PDN with a perforated metallic power plane was investigated which is an array of interconnected metallic patches patterned on a dielectric substrate (see Fig. 3.13(a)). The unit cell of the periodic structure and its equivalent transmission line model is shown in Fig. 3.13(b). In the TL model metallic patches are represented by low-impedance ($Z_l = \frac{\eta_0}{\sqrt{\epsilon_r}}\frac{h}{w}$) transmission-line sections of length $d = \frac{w}{2}$ and microstrip interconnects are modeled by high-impedance ($Z_h = \frac{\eta_0}{\sqrt{\epsilon_r}}\frac{2h}{g}$) transmission-line sections of length $\frac{g}{2} = \frac{a-w}{2}$. The propagation constants of both transmission-line sections are the same and are given by $\gamma_d = j\beta_d = j\frac{\omega}{c}\sqrt{\epsilon_r}$. Using Eq. (2.22), the characteristic equation of the TL model reads

$$\cosh\gamma_x a + \cosh\gamma_y a = 2\cos(\beta_d a) + \left(2 - \frac{Z_l}{Z_h} - \frac{Z_h}{Z_l}\right)\sin\beta_d w \sin\beta_d(a-w) \tag{3.25}$$

which can now be solved using both approaches.

Fig. 3.14 shows the propagating modes of the structure obtained by specifying the propagation vector $\boldsymbol{\beta}$ and solving Eq. (3.25) for admitted frequencies. Further inspection

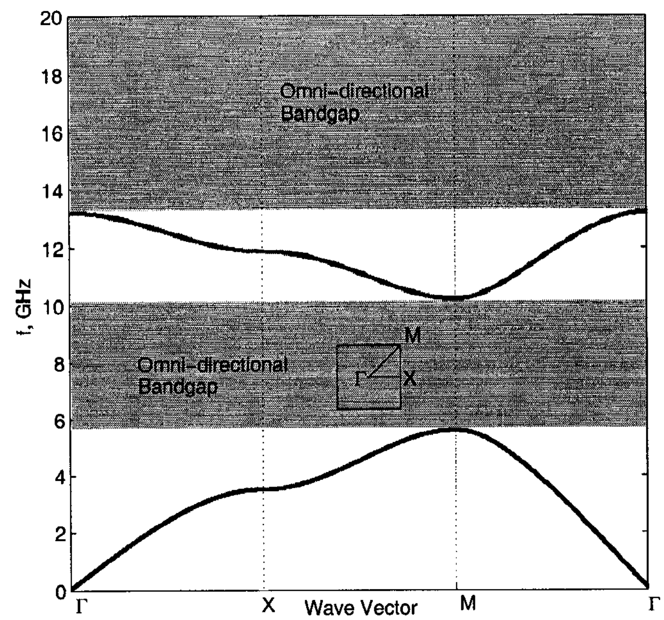

Fig. 3.14 Dispersion curves of the PDN with a perforated power plane of Fig. 3.13(b)

of the dispersion curves reveals that there are two omni-directional stopbands within the frequency range plotted here.

In the second set of trials, the complex modes of the structure were obtained by specifying frequency and finding propagation constants. Corresponding to each region of the Brillouin zone (Γ–X, X–M, M–Γ), complex propagation constants are obtained and plotted in Figs. 3.15–3.17, respectively. The real part of the complex propagation constant in each region predicts the stopband behavior of the PDN within each omni-directional bandgap.

It can be noted that the dimensions used in the design of Fig. 3.13(b) do not lead to optimum characteristics. As can be seen in Fig. 3.14, the current design of Fig. 3.13(b) yields a fundamental stopband extending over the frequency range 6–10 GHz while a wider bandgap with lower cut-off frequency (around 1 GHz) is required for such applications in PDNs. The developed TL model can now be used to determine the required specifications for a proper design as it provides a fast means of design optimization and bandgap characterization.

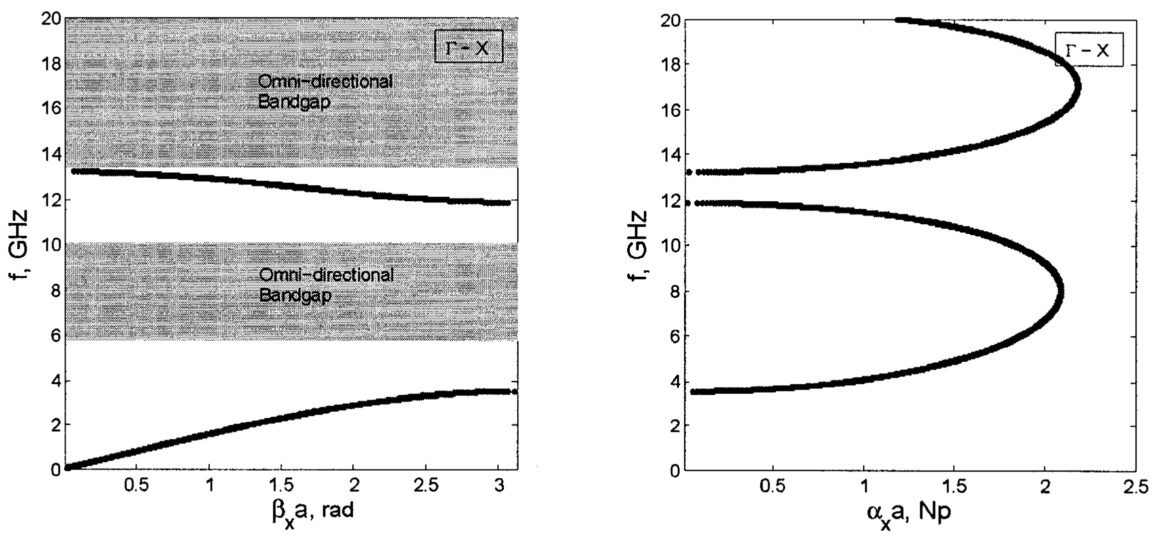

Fig. 3.15 Complex propagation constant of the interconnected patched in region Γ–X: (a) imaginary part, and (b) real part.

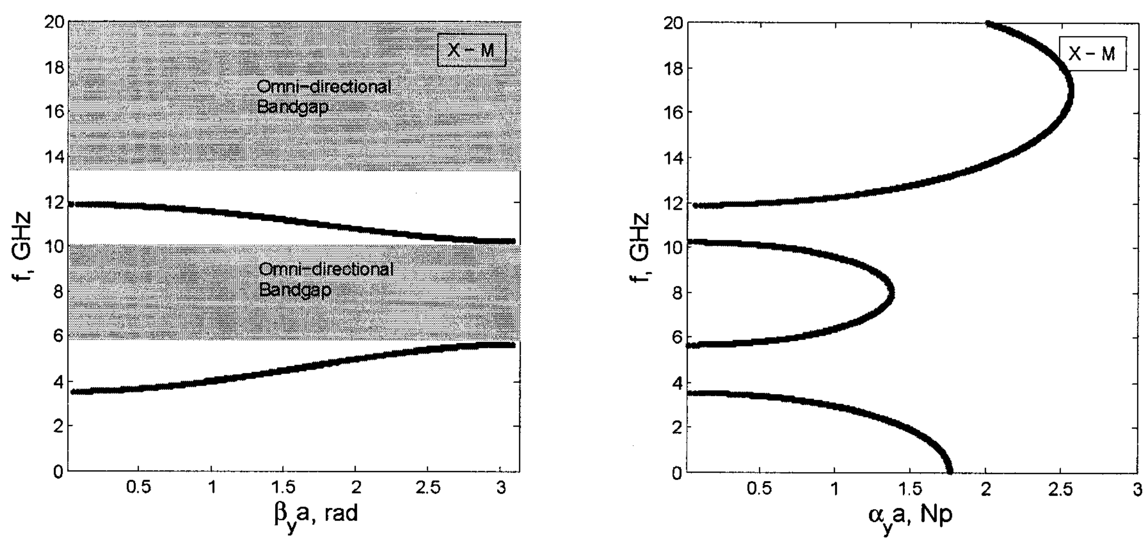

Fig. 3.16 Complex propagation constant of the interconnected patched in region X–M: (a) imaginary part, and (b) real part.

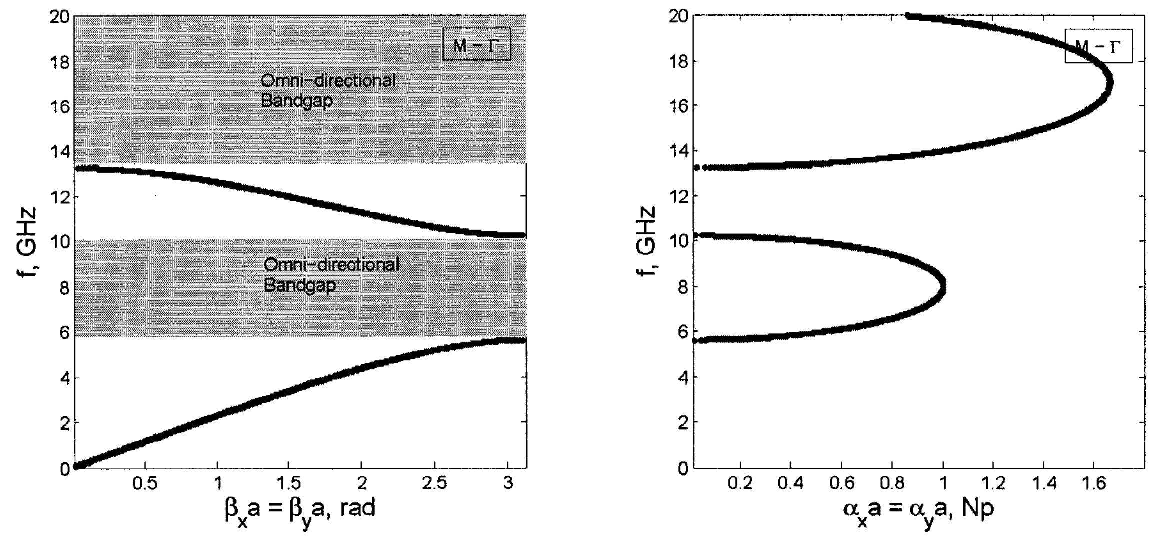

Fig. 3.17 Complex propagation constant of the interconnected patched in region M–Γ: (a) imaginary part, and (b) real part.

3.3 Extraction of Insertion Loss Information from $k - \alpha$ Diagrams

The attenuation diagrams presented in the preceding sections can be efficiently used to investigate port isolation and insertion loss characteristics between two measurement ports placed arbitrarily in such modified PDN boards.

To obtain the power attenuation along each direction of propagation one should find the insertion loss between two measurement ports as given by

$$S_{21} = 20 \log \left(e^{-\boldsymbol{\alpha}(f) \cdot \hat{\mathbf{r}}\ na} \right) \tag{3.26}$$

where n is the number of unit cells along the considered direction and S_{21} has the unit of decibel. The attenuation values (αa) are obtained from the $k - \alpha$ diagram associated with the corresponding region of the irreducible Brillouin zone for that direction. Indeed, Eq. (3.26) expresses the overall incurred losses in signal (noise) transmission through PDNs containing an EBG structure.

For instance, in Fig. 3.18 the insertion loss along x-direction for four unit cells of the PDN shown in Fig. 3.8(a) is presented. A representative diagram of this structure depicting

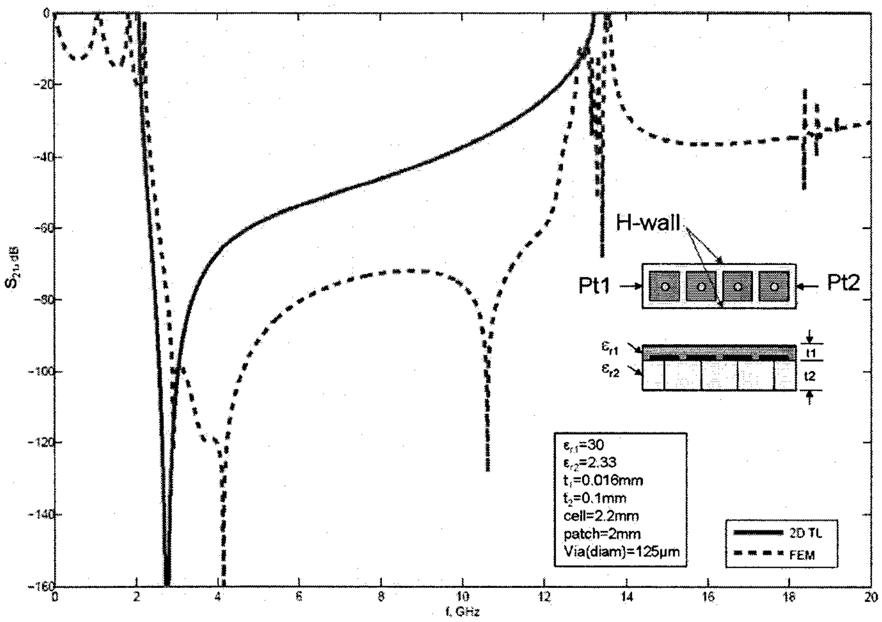

Fig. 3.18 Insertion loss along four unit cells of the modified PDN of Fig. 3.8(a) in the x-direction. The simulation setup for the FEM analysis is presented in the inset diagram.

the locations of port 1 and port 2 is shown in the inset of Fig. 3.18. This S_{21} response is generated using Eq. (3.26) along with the attenuation values ($\alpha_x a$) obtained from Fig. 3.10 for the Γ–X region of the irreducible Brillouin zone. Also presented in Fig. 3.18 is the insertion loss obtained from full-wave simulations using the commercial FE-based software, HFSS [65]. To simulate the 2D periodic structure, H-wall boundary conditions were considered for the sidewalls in FEM simulations. It can be observed from Fig. 3.18 that the 2D transmission-line model provides an accurate prediction of the bandgap as well as capturing the essence of insertion loss signature up to relatively high frequencies. Lastly, it should be mentioned that the 2D TL simulations were obtained in less than a couple of seconds while it took about half an hour for the commercial FEM solver to generate the insertion loss diagram using the same computational resources.

3.4 Discussion

The 2D transmission-line model presented in this chapter has been shown to be capable of capturing complex modes of PDNs containing EBG structures. Moreover, the transmission-line model results in a small matrix equation, namely the dispersion equation, which allows for rapid production (in a few seconds) of band diagrams. Therefore, a first-order estimation of the propagating modes within passbands as well as the evanescent/complex modes within stopbands is obtained through a simple formulation. Consequently, the band diagrams and the corresponding attenuation diagrams are generated in a fast and efficient fashion. Thus we may conclude that the question of modal behavior of 2D periodic structure within their forbidden frequency regions can be partially answered using simplified TL models.

However, as discussed before, the transmission-line models are of limited accuracy. Such models are generally valid up to certain frequencies and are suitable for specific field configurations in periodic structures. For instance, Fig. 3.19 reproduces the band diagrams of the shielded mushroom structure (Fig. 3.9) using HFSS. In the first passband there is excellent agreement between the transmission-line model and the FEM simulations. Furthermore, the 2D model predicts the induced stopband over the frequency range 2.47 – 13.23 GHz quite accurately (compared to full-wave simulations). In terms of simulations time, the TL model results are obtained in seconds while the FEM simulations take hours on the same computing platform. From the accuracy viewpoint, as the frequency increases, the higher order LSM and LSE[3] modes in the loaded PPW are excited and the quasi-TEM transmission-line model fails to accurately predict the full band structure of the modified PDN. It can be observed from Fig. 3.19, that the higher order modes (above 13 GHz) and the second stopband in the dispersion diagram obtained from FEM simulations are not captured by the circuit model. This suggests that the simple lumped-element substitute for the EBG structure within the PPW seems to be valid up to certain frequencies and a more accurate model is required for prediction of the band structure at higher frequencies.

Furthermore, a full-wave method is required that can capture complex modes of such periodic structures. Current state of the art of field analysis techniques (particularly commercial software packages), allows for finding propagating modes of periodic structures, solely. Available general purpose electromagnetic (EM) codes commonly obtain the band

[3]LSE stands for longitudinal section electric. Hybrid TE_z modes also referred to as LSE modes have no axial (z-directed) electric field component.

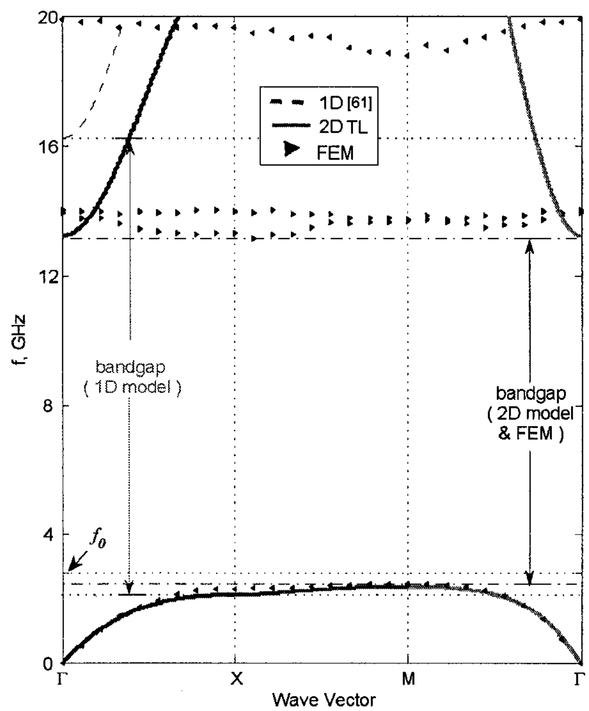

Fig. 3.19 Dispersion curves of the mushroom-type EBG embedded in a parallel-plate power plane (comparison with the FEM).

diagrams of periodic structures by specifying propagation vectors $\boldsymbol{\beta}$ and finding eigen frequencies. Therefore, the accuracy of dispersion curves presented in Figs. 3.4, 3.9, 3.14 can easily be validated using full-wave commercial softwares. However, in order to accurately predict the stopband behavior a field analysis technique is required that can treat the propagation constant as the unknown of the formulation. This particularly is needed to verify the accuracy of the attenuation diagrams (e.g. Figs. 3.5–3.7, 3.10–3.12, 3.15–3.17) obtained with transmission-line model using the latter approach as they cannot be validated by the available full-wave simulators. For that purpose, the author has developed a computer code based on the finite element method which can be applied to periodic structures to provide their bandgap information in all azimuthal directions. Development, implementation and testing of the finite element model is the subject of the following chapter.

Chapter 4

Finite Element Modeling

The finite element method is a popular electromagnetic modeling technique. FEM is particularly well suited for computing steady-state responses. This chapter concentrates on the FE modeling of periodic structures as opposed to the TL model that was discussed in Chapter 3. The FE model employs a weighted residual formulation, that is applicable to complex eigenmode analysis of the electromagnetic waves in periodic structures.

§ 4.1 briefly discusses the relevant electromagnetic theory and the weighted residual formulation of the problem. This section also outlines the resulting matrix polynomial and its assembly process. Implementation details of the finite element program and its integration in mesh generation and eigensolver modules are explained in § 4.2. Numerical results for different simulation models are presented in § 4.3. Plots of the imaginary and the real parts of the propagation constants versus frequency are shown. These plots demonstrate the efficiency and capability of the developed FE code in capturing complex modes.

4.1 Theory

Solutions of electromagnetic problems by the finite element method have well established procedures. FE formulations are worked out either using the Rayleigh-Ritz variational principle or using the Galerkin choice of the family of weighted residual methods [66]. Either method is ordinarily expected to give the same results. The common approach for high frequency vectorial FE formulations is via a variational route [67]. In the present work it is found that the treatment applicable to periodic constraints follows conveniently from a weighted residual analysis.

4.1.1 Vector Wave Equation

Consider Maxwell's equations in differential form. When applied to solving electromagnetic problems with steady-state oscillations, field variables are denoted by complex phasors [29]. We start from Faraday's and Ampère's laws, assuming magnetically and electrically linear media:

$$\begin{aligned} \nabla \times \mathbf{E} &= -\jmath\omega\mu\mathbf{H} && (4.1) \\ \nabla \times \mathbf{H} &= \jmath\omega\epsilon\mathbf{E} + \mathbf{J} && (4.2) \end{aligned}$$

where $\mathbf{E}$ is electric field, $\mathbf{H}$ is magnetic field, μ is permeability of the medium, ϵ is permittivity of the medium and $\mathbf{J}$ is current density.

Assuming there are no free charges and currents in the device, Eqns. (4.1) and (4.2) may be combined to obtain the vector wave equation:

$$\nabla \times \frac{1}{p}\nabla \times \mathbf{F} - k_0^2 q\mathbf{F} = 0 \tag{4.3}$$

where $k_0^2 = \omega^2\mu_0\epsilon_0$, $p = \mu_r$, $q = \epsilon_r$ for $\mathbf{F} = \mathbf{E}$ and $p = \epsilon_r$, $q = \mu_r$ for $\mathbf{F} = \mathbf{H}$. Eq. (4.3) along with essential boundary conditions governs the propagation of electromagnetic waves in a periodic structure [12].

A problem domain bounded by a closed surface is considered (see the unit-cell in Fig. 4.1). In general the bounding surface of the unit-cell may comprise any or all of the following: an electric wall on which $\mathbf{n} \times \mathbf{E} = 0$; a magnetic wall on which $\mathbf{n} \times \mathbf{H} = 0$; or periodic boundary pairs, over which the transverse fields are related by:

$$\begin{aligned} \mathbf{F}_t(D_x, y, z) = &\; C_x\mathbf{F}_t(0, y, z) \\ \mathbf{F}_t(x, D_y, z) = &\; C_y\mathbf{F}_t(x, 0, z) \\ \mathbf{F}_t(x, y, D_z) = &\; C_z\mathbf{F}_t(x, y, 0) \end{aligned} \tag{4.4}$$

where $C_x = e^{-\gamma_x D_x}$, $C_y = e^{-\gamma_y D_y}$, $C_z = e^{-\gamma_z D_z}$ and $\boldsymbol{\gamma} = (\gamma_x, \gamma_y, \gamma_z)$ is the Floqeut propagation vector and subscript t denotes tangential part of the vector $\mathbf{F}$. As implied by (4.4), the periodicity can be along each coordinate axis of the structure.

Finding an approximate solution $\tilde{\mathbf{F}}$ to the unknown vector variable $\mathbf{F}$ is the subject of the following sections. Throughout the rest of this thesis, we choose $\mathbf{E}$ as the working

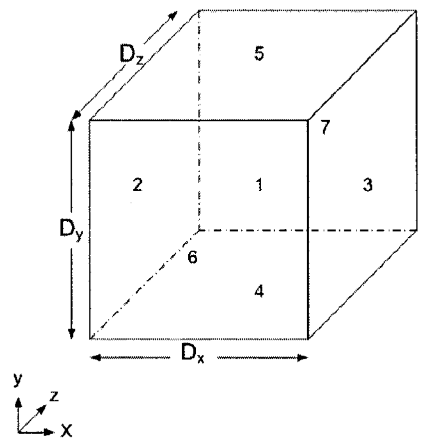

Fig. 4.1 The unit-cell of a 3D periodic problem.

variable; the formulation for **H** follows trivially.

4.1.2 Weighted Residual Formulation

In the weighted residual method, the approximate solution to a typical boundary value problem is sought by weighting the residual of the governing differential equation. The best approximation to the unknown quantity is the one that minimizes the residual error to the least value at all points of Ω [66]. Consider the weighted residual integral

$$R = \int_{\Omega} \left(\nabla \times \mathbf{W} \cdot \frac{1}{\mu_r} \nabla \times \tilde{\mathbf{E}} - k_0^2 \mathbf{W} \cdot \epsilon_r \tilde{\mathbf{E}} \right) \mathrm{d}\Omega. \tag{4.5}$$

Applying the vector form of Green's theorem [68] to Eq. (4.5) yields:

$$\begin{aligned} R &= \int_{\Omega} \mathbf{W} \cdot \left(\nabla \times \frac{1}{\mu_r} \nabla \times \tilde{\mathbf{E}} - k_0^2 \epsilon_r \tilde{\mathbf{E}} \right) \mathrm{d}\Omega \\ &- \oint_S \left(\mathbf{W} \times \frac{1}{\mu_r} \nabla \times \tilde{\mathbf{E}} \right) \cdot \mathbf{n} \ \mathrm{dS}. \end{aligned} \tag{4.6}$$

Thus, setting to zero the residual given in Eq. (4.5) for an arbitrary weight function **W**, requires that the governing curl-curl equation is satisfied

$$\nabla \times \frac{1}{\mu_r} \nabla \times \tilde{\mathbf{E}} - k_0^2 \epsilon_r \tilde{\mathbf{E}} = 0 \tag{4.7}$$

and
$$\oint_S \left(\mathbf{W} \times \frac{1}{\mu_r} \nabla \times \tilde{\mathbf{E}} \right) \cdot \mathbf{n} \, \mathrm{dS} = 0 \tag{4.8}$$
i.e. the surface integral vanishes for every weight function.

Further inspection of the surface integral reveals that (4.8) is naturally eliminated provided that the trial function $\tilde{\mathbf{E}}$ and weight functions $\mathbf{W}$ are subject to periodic constraints in a manner similar to [12]. For instance, consider the boundary closures associated with the x periodicity in Fig. 4.1. For this boundary pair, the trial functions are restricted to C_0 functions [69] whose transverse components are related by

$$\tilde{\mathbf{E}}_t(D_x, y, z) = C_x \tilde{\mathbf{E}}_t(0, y, z), \tag{4.9}$$

while the restriction on the transverse components of the weight functions is imposed by reciprocal exponential factors; i.e.

$$\mathbf{W}_t(D_x, y, z) = \frac{1}{C_x} \mathbf{W}_t(0, y, z). \tag{4.10}$$

Then because of the equal and opposite normal vector $\mathbf{n}$, the parts of the surface integral corresponding to this boundary pair yield:

$$\begin{aligned} &\int_{x=0} \mathbf{W}_t \times \left(\frac{1}{\mu_r} \nabla \times \tilde{\mathbf{E}} \right)_t \cdot \mathbf{n} \, \mathrm{dS} + \int_{x=D_x} \mathbf{W}_t \times \left(\frac{1}{\mu_r} \nabla \times \tilde{\mathbf{E}} \right)_t \cdot \mathbf{n} \, \mathrm{dS} = \\ &\int_{x=0} \mathbf{n} \times \mathbf{W}_{t0} \cdot \left[\left(\frac{1}{\mu_r} \nabla \times \tilde{\mathbf{E}} \right)_t (0, y, z) - \frac{1}{C_x} \left(\frac{1}{\mu_r} \nabla \times \tilde{\mathbf{E}} \right)_t (D_x, y, z) \right] \mathrm{dS} = 0 \end{aligned} \tag{4.11}$$

where $\mathbf{W}_{t0} = \mathbf{W}_t(0, y, z)$. The residual term given by (4.11) is naturally forced to zero for all $\mathbf{W}_{t0}$ since (4.1) and (4.4).

In a similar fashion, the transverse components of trial functions $\tilde{\mathbf{E}}$ and weight functions $\mathbf{W}$ can be constrained along the other two periodicity axes (y- and z-axis), eliminating the surface integral in Eq. (4.8). These constraints are given by:

$$\begin{aligned} \tilde{\mathbf{E}}_t(x, D_y, z) &= C_y \tilde{\mathbf{E}}_t(x, 0, z) \\ \tilde{\mathbf{E}}_t(x, y, D_z) &= C_z \tilde{\mathbf{E}}_t(x, y, 0) \end{aligned} \tag{4.12}$$

and

$$\begin{aligned}\mathbf{W}_t(x, D_y, z) &= \frac{1}{C_y}\mathbf{W}_t(x, 0, z)\\ \mathbf{W}_t(x, y, D_z) &= \frac{1}{C_z}\mathbf{W}_t(x, y, 0).\end{aligned} \tag{4.13}$$

In passing we notice that the trial function $\tilde{\mathbf{E}}$ and weight functions $\mathbf{W}$ are further restricted to vector functions whose transverse components on electric walls are specified as $\tilde{\mathbf{E}}_t = 0$ and $\mathbf{W}_t = 0$. The latter forces the surface integral to vanish on portions of S where homogeneous Dirichlet boundary condition ($\mathbf{n} \times \mathbf{E} = 0$) should be imposed [69]. Magnetic walls, however, do not need any special treatment since (4.8) naturally vanishes over those portions:

$$(\mathbf{W} \times \mathbf{H}) \cdot \mathbf{n} = -(\mathbf{n} \times \mathbf{H}) \cdot \mathbf{W} = 0. \tag{4.14}$$

Therefore, the residual

$$R = \int_\Omega \left(\nabla \times \mathbf{W} \cdot \frac{1}{\mu_r}\nabla \times \tilde{\mathbf{E}} - k_0^2 \mathbf{W} \cdot \epsilon_r \tilde{\mathbf{E}}\right) \mathrm{d}\Omega \tag{4.15}$$

applies to the whole region Ω. Setting to zero the expression given in Eq. (4.15) thus forms the basis for a weighted residual solution of the electromagnetic problem described here.

4.1.3 Selection of Interpolation Functions

The use of vector interpolation functions (also known as tangential or edge elements) in the solution of 3D electromagnetics is now well established. It prevents non-zero spurious solutions associated with nodal finite elements, from appearing. Edge elements have degrees of freedom (Dof) associated with edges rather than nodes. They enforce tangential continuity, but not normal continuity, on the trial vector variable. Relaxation of normal continuity is important in dealing with abrupt changes in ϵ_r and μ_r as well as conducting and dielectric sharp corners [70].

Here, vector finite elements, such as tetrahedral elements [71], are employed to set up the trial functions. Within a finite element e the vector variable $\tilde{\mathbf{E}}$ is expanded as:

$$\tilde{\mathbf{E}}^e = \sum_{j(e)} E_j^e g_j^e \mathbf{N}_j^e \tag{4.16}$$

where $\mathbf{N}_j^e$ are the vector interpolation functions and E_j^e are the corresponding scalar degrees of freedom. The constant g_j^e is introduced to impose the desired constraints. In Galerkin's option of weighted residual method, the weight functions are selected from expansion functions:

$$\mathbf{W}_i^e = \mathrm{c}_i^e \mathbf{N}_i^e \tag{4.17}$$

where c_i^e are arbitrary constants. This usually leads to the most accurate solutions and is therefore widely used in developing FE formulations [66].

The constants g_j^e and c_i^e are specified in a way that ensures the required constraints on $\mathbf{W}$ and $\tilde{\mathbf{E}}$ are satisfied [12]:

- If $\mathbf{N}_i^e$ corresponds to an element edge or face in an $\mathbf{n} \times \mathbf{E} = 0$ constrained surface, c_i^e is set to zero to satisfy the requirement $\mathbf{W}_t = 0$ on that surface.

- Otherwise, If $\mathbf{N}_j^e$ lies on an internal element boundary, g_j^e and c_j^e are chosen such that for any element e' sharing that face or edge, $\mathrm{g}_j^e = \mathrm{g}_j^{e'}$ and $\mathrm{c}_j^e = \mathrm{c}_j^{e'}$. A value of $\mathrm{g}_j^e = 1$ and $\mathrm{c}_j^e = 1$ may conveniently be chosen in that case.

- If $\mathbf{N}_j^e$ is associated with a degree of freedom E_j^e on the master surface of a periodic boundary pair (say geometric part 2 in Fig. 4.1), there is a degree of freedom $E_k^{e'}$ associated with $\mathbf{N}_j^{e'}$ on the corresponding slave surface (geometric part 3 in Fig. 4.1). Then choosing $\mathrm{g}_j^e = 1$, Eq. (4.9) implies that $\mathrm{g}_k^{e'} = C_x$. In a similar fashion, c_j^e is set to unity while Eq. (4.10) restricts $\mathrm{c}_k^{e'}$ to $\frac{1}{C_x}$.

The first two restrictions on g_j^e and c_i^e guarantee the C_0 continuity of $\mathbf{W}$ and $\tilde{\mathbf{E}}$ across inter-element boundaries, as well as the imposition of $\mathbf{n} \times \tilde{\mathbf{E}} = 0$ on electric walls. The third constraint, however, holds provided the finite element mesh is identical at periodic boundary pairs [12]. This way $E_j^{e'}$ can be set equal to E_j^e thereby eliminating it from the list of unknowns.

The system of equations that results from the discretization (4.16) and incorporation of the above constraints are explained next.

4.1.4 Assembly to Form the System of Equations

The next step, which is a major step in finite element analysis, is to set up the FE matrices. To formulate the system of equations, the elemental residual is formed first. Then through a process called *assembly*, this residual is summed over all elements. Finally the boundary conditions are imposed to obtain the final form of the FE matrices.

The C_0 continuity imposed on the trial functions assures safe use of:

$$R_i^e = \int_{\Omega_e} \left(\nabla \times \mathbf{W}_i^e \cdot \frac{1}{\mu_r} \nabla \times \tilde{\mathbf{E}}^e - k_0^2 \epsilon_r \mathbf{W}_i^e \cdot \tilde{\mathbf{E}}^e \right) \mathrm{d}\Omega \tag{4.18}$$

as the elemental residual. Indeed, the surface integrals associated with inter-element boundaries cancel in the summation over all elements and thereby need not be included in Eq. (4.18) [12]. In matrix notation Eq. (4.18) is represented by:

$$\{R^e\} = [\mathrm{C}^e]\left([\mathrm{S}^e] - k_0^2[\mathrm{T}^e]\right)[\mathrm{G}^e]\{E^e\} \tag{4.19}$$

where $\{R^e\}$ and $\{E^e\}$ are column vectors corresponding to $\mathbf{W}_i^e$ and E_j^e, respectively. Assuming that μ_r and ϵ_r are constant within Ω_e, the local matrix elements S_{ij} and T_{ij} are given by:

$$\mathrm{S}_{ij} = \frac{1}{\mu_r} \int_{\Omega_e} \nabla \times \mathbf{N}_i^e \cdot \nabla \times \mathbf{N}_j^e \, \mathrm{d}\Omega \tag{4.20}$$

$$\mathrm{T}_{ij} = \epsilon_r \int_{\Omega_e} \mathbf{N}_i^e \cdot \mathbf{N}_j^e \, \mathrm{d}\Omega. \tag{4.21}$$

Furthermore, $[\mathrm{C}^e]$ and $[\mathrm{G}^e]$ are diagonal matrices with nonzero elements c_i^e and g_j^e, respectively. Eq. (4.19) avoids building c_i^e and g_j^e into $[\mathrm{S}^e]$ and $[\mathrm{T}^e]$ which allows these constants to be treated as unknowns. Summing (4.19) over all elements, a global matrix equation:

$$\{R\} = [\mathrm{C}]\left([\mathrm{S}] - k_0^2[\mathrm{T}]\right)[\mathrm{G}]\{E\} = 0 \tag{4.22}$$

is assembled where $\{E\}$ is the column vector of degrees of freedom.

In order to incorporate the periodic constraints in the assembled global matrices, we notice that vector $\{E\}$ can be divided into four subvectors:

$$\{E\} = \left\{ \begin{array}{c} E_{Int} \\ E^z_{\mathrm{M,S}} \\ E^y_{\mathrm{M,S}} \\ E^x_{\mathrm{M,S}} \end{array} \right\} \tag{4.23}$$

where each subvector is associated with one of the geometric parts labeled in Fig. 4.1. $\{E_{Int}\}$ corresponds to degrees of freedom that do not lie on any of the periodic boundary pairs of the unit-cell closure (geometric part 1 in Fig. 4.1). $\{E^x_{\mathrm{M,S}}\}$ corresponds to Dofs associated with edges or faces that lie on periodic boundary pair (2,3) in Fig. 4.1 and $\{E^y_{\mathrm{M,S}}\}$ and $\{E^z_{\mathrm{M,S}}\}$ are associated with periodic boundary pairs (4,5) and (6,7), respectively.

Now, eliminating the degrees of freedom associated with slave surfaces of periodic boundary pairs (geometric parts 3, 5 and 7 in Fig. 4.1) and introducing periodic constraints in [C] and [G], the global matrix equation can be rewritten as:

$$\{\bar{R}\} = [\bar{\mathrm{C}}]\left([\mathrm{S}] - k_0^2[\mathrm{T}]\right)[\bar{\mathrm{G}}]\{\bar{E}\} = 0 \tag{4.24}$$

where $\{\bar{E}\} = \{E_{Int}\ E^z_{\mathrm{M}}\ E^y_{\mathrm{M}}\ E^x_{\mathrm{M}}\}^{\mathrm{T}}$ is the column vector of reduced degrees of freedom. $[\bar{\mathrm{G}}]$ and $[\bar{\mathrm{C}}]$ are rectangular matrices, represented in block form by:

$$[\bar{\mathrm{G}}] = \begin{bmatrix} \mathrm{I} & 0 & 0 & 0 \\ 0 & \mathrm{I} & 0 & 0 \\ 0 & C_z\mathrm{I} & 0 & 0 \\ 0 & 0 & \mathrm{I} & 0 \\ 0 & 0 & C_y\mathrm{I} & 0 \\ 0 & 0 & 0 & \mathrm{I} \\ 0 & 0 & 0 & C_x\mathrm{I} \end{bmatrix} \tag{4.25}$$

$$[\bar{\mathrm{C}}] = \begin{bmatrix} \mathrm{I} & 0 & 0 & 0 & 0 & 0 & 0 \\ 0 & \mathrm{I} & \frac{1}{C_z}\mathrm{I} & 0 & 0 & 0 & 0 \\ 0 & 0 & 0 & \mathrm{I} & \frac{1}{C_y}\mathrm{I} & 0 & 0 \\ 0 & 0 & 0 & 0 & 0 & \mathrm{I} & \frac{1}{C_x}\mathrm{I} \end{bmatrix} \tag{4.26}$$

where I stands for identity matrix of appropriate size. Hence, Eq. (4.24) becomes:

$$\{\bar{R}\} = \left([\bar{\mathrm{S}}] - k_0^2[\bar{\mathrm{T}}]\right)\{\bar{E}\} = 0 \tag{4.27}$$

where

$$[\bar{\mathrm{S}}] = [\bar{\mathrm{C}}]\,[\mathrm{S}]\,[\bar{\mathrm{G}}]\,, \tag{4.28}$$

$$[\bar{\mathrm{T}}] = [\bar{\mathrm{C}}]\,[\mathrm{T}]\,[\bar{\mathrm{G}}]\,. \tag{4.29}$$

Eq. (4.27) is now ready to be solved for the degrees of freedom $\{\bar{E}\}$, i.e. the unknown coefficients E_j^e used in (4.16) expansion.

4.1.5 Solution of the System of Equations

The final step in a finite element analysis is solving the system of equation. The resultant system may be divided into two categories: deterministic and eigenvalue types. Deterministic types are associated with electromagnetic problems where there exists a source or excitation. On the contrary, eigenvalue types are usually associated with source-free problems [66].

The electromagnetic problem that was investigated is source free. Therefore, Eq. (4.27) becomes an eigenequation. It potentially carries two different eigenvalue problem. One is posed as if γ is given and k_0 is sought, while specifying k_0 yields the other.

Fixed-γ eigenproblem

One way to solve Eq. (4.27) is to specify the Floquet propagation vector $\boldsymbol{\gamma} = (\gamma_x, \gamma_y, \gamma_z)$ and find the eigenvalues k_0^2 and eigenvectors $\{\bar{E}\}$ of the generalized eigenvalue problem (GEP):

$$[\bar{\mathrm{S}}]\{\bar{E}\} = k_0^2[\bar{\mathrm{T}}]\{\bar{E}\}. \tag{4.30}$$

Given $C_x = e^{-\gamma_x D_x}$, $C_y = e^{-\gamma_y D_y}$ and $C_z = e^{-\gamma_z D_z}$ the matrices $[\bar{\mathrm{G}}]$ and $[\bar{\mathrm{C}}]$ are accordingly built using Eqns. (4.25), (4.26). Thereafter one finds $[\bar{\mathrm{S}}]$ and $[\bar{\mathrm{T}}]$ from (4.28), (4.29) to form the above eigenequation.

A similar approach has been used in [12] with $\boldsymbol{\gamma} = j\boldsymbol{\beta}$. In [12], the Floquet propagation vector $\boldsymbol{\beta} = (\beta_x, \beta_y, \beta_z)$ is directly built into [S] and [T] to form the eigenequation without introducing $[\bar{\mathrm{G}}]$ and $[\bar{\mathrm{C}}]$. However, with this approach, only the unattenuated propagating modes of the structure, i.e. the passband characteristics, are captured. In order to obtain the stopband behavior and correspondingly the complex solutions of the propagation vector, one should treat Eq. (4.27) the other way around, leaving $\boldsymbol{\gamma}$ as an unknown of the equation. Introducing $[\bar{\mathrm{G}}]$ and $[\bar{\mathrm{C}}]$ into the system of equations, allows us to reformulate Eq. (4.27) in terms of $\boldsymbol{\gamma}$ and solve for it as explained in the next section.

Fixed-k_0 eigenproblem

The other eigenproblem, which here we are more interested in, is obtained by specifying a k_0 and seeking γ. For simplicity, assume the direction of wave propagation is solely along the x-axis, i.e. $\gamma = (\gamma_x, 0, 0)$. Carrying out the matrix multiplications given in Eq. (4.28) one may write:

$$\begin{aligned}
[\bar{\mathrm{S}}] &= [\bar{\mathrm{C}}]\,[\mathrm{S}]\,[\bar{\mathrm{G}}] \\
&= \begin{bmatrix} \mathrm{D}_c & 0 & 0 \\ 0 & \mathrm{I} & \frac{1}{C_x}\mathrm{I} \end{bmatrix} \begin{bmatrix} \mathrm{S}_{11} & \mathrm{S}_{12} & \mathrm{S}_{13} \\ \mathrm{S}_{21} & \mathrm{S}_{22} & \mathrm{S}_{23} \\ \mathrm{S}_{31} & \mathrm{S}_{32} & \mathrm{S}_{33} \end{bmatrix} \begin{bmatrix} \mathrm{D}_g & 0 \\ 0 & \mathrm{I} \\ 0 & C_x\mathrm{I} \end{bmatrix} \\
&= \begin{bmatrix} \mathrm{D}_c\mathrm{S}_{11}\mathrm{D}_g & \mathrm{D}_c\mathrm{S}_{12} + C_x\mathrm{D}_c\mathrm{S}_{13} \\ \mathrm{S}_{21}\mathrm{D}_g + \frac{1}{C_x}\mathrm{S}_{31}\mathrm{D}_g & \mathrm{S}_{22} + C_x\mathrm{S}_{23} + \frac{1}{C_x}\mathrm{S}_{32} + \mathrm{S}_{33} \end{bmatrix}
\end{aligned} \tag{4.31}$$

where [S] is represented in block form. Also, blocks of $[\bar{\mathrm{C}}]$ and $[\bar{\mathrm{G}}]$ associated with interior parts and y- and z-periodicity are denoted by D_c and D_g, respectively. Then, doing the same for $[\bar{\mathrm{T}}]$, Eq. (4.27) reads:

$$\begin{aligned}
\{\bar{R}\} &= ([\bar{\mathrm{S}}] - k_0^2[\bar{\mathrm{T}}])\{\bar{E}\} \\
&= ([\mathrm{M}_1] + C_x[\mathrm{M}_2] + \frac{1}{C_x}[\mathrm{M}_3])\{\bar{E}\} = 0
\end{aligned} \tag{4.32}$$

where

$$\begin{aligned}
[\mathrm{M}_1] &= \begin{bmatrix} \mathrm{D}_c(\mathrm{S}_{11} - k_0^2\mathrm{T}_{11})\mathrm{D}_g & \mathrm{D}_c(\mathrm{S}_{12} - k_0^2\mathrm{T}_{12}) \\ (\mathrm{S}_{21} - k_0^2\mathrm{T}_{21})\mathrm{D}_g & \mathrm{S}_{22} + \mathrm{S}_{33} - k_0^2(\mathrm{T}_{22} + \mathrm{S}_{33}) \end{bmatrix} \\
[\mathrm{M}_2] &= \begin{bmatrix} 0 & \mathrm{D}_c(\mathrm{S}_{13} - k_0^2\mathrm{T}_{13}) \\ 0 & \mathrm{S}_{23} - k_0^2\mathrm{T}_{23} \end{bmatrix} \\
[\mathrm{M}_3] &= \begin{bmatrix} 0 & 0 \\ (\mathrm{S}_{31} - k_0^2\mathrm{T}_{31})\mathrm{D}_g & \mathrm{S}_{32} - k_0^2\mathrm{T}_{32} \end{bmatrix}.
\end{aligned} \tag{4.33}$$

Eq. (4.32) is a quadratic eigenvalue problem (QEP) in C_x. Its eigenvalues yield the propagation constant γ_x which may now be a real, an imaginary or a complex value. We conclude that the above reformulation is expected to capture complex modes of the structure and thereby is capable of predicting the stopband behavior as well as passband.

In the above analysis, the contribution of C_y and C_z is accounted for in block matrices D_c and D_g which in this case are independent of C_x. However, there is no fundamental difficulty in treating the more general case with nonzero γ_y and γ_z. The bottom line is the same, yielding a nonlinear eigenvalue problem in C_x, but of higher order, where for a specific direction of wave propagation vector γ, C_y and C_z are written in terms of C_x.

4.2 Implementation

The present thesis integrates three software tools for computer implementation of the FE analysis outlined in § 4.1: Geompack++, P3D and MATLAB. Geompack++ [72] is a mesh generation package and is used for subdivision of the domain into finite elements. P3D [73] is a 3D finite element code for solving Maxwell's equations in time-harmonic regime, employed for building the FE matrices. The matrix equation is finally solved using MATLAB's eigensolver [74].

In addition to the input/output files provided for proper functioning/integration of the three modules, the author has developed a number of routines for incorporation of the periodic analysis into the FE code.

4.2.1 Domain Discretization

The discretization of the problem domain is usually considered a preprocessing task which can be completely separated from the other steps. The manner in which the domain is subdivided into finite elements greatly affects the memory requirements, the computation time and the accuracy of the numerical simulations [66]. Thus considerable attention has been devoted to optimized FE discretization since its conception [75], [76].

Among the many public domain and commercial mesh generators, Geompack++ has been chosen in this thesis to perform meshing operations. Geompack++ is an object-oriented C++ successor of Geompack90[1] for the generation of 2D and 3D finite element meshes. Its capabilities include: generating a mesh given a region, generating a 3D mesh given a surface mesh and improving/refining a given mesh. Due to the efficient algorithms, Geompack++ runs very fast on Windows systems.

One of the advantages of Geompack++, over the other mesh generators, is that it allows

[1] Written in Fortran90 and first released in June 1999.

discretizing a fully 3D periodic unit-cell with identical boundary meshes for more than one master/slave pair. As mentioned in § 4.1.3 P. 54, it is a requirement that the finite element mesh at periodic boundary pairs be identical. Many mesh generators would not allow *any* periodic cases to be investigated or mostly restrict the analysis to singly periodic cases. With Geompack++, however, doubly and triply periodic cases can be easily investigated by enforcing identical meshes at each periodic boundary pair (see Fig. 4.2).

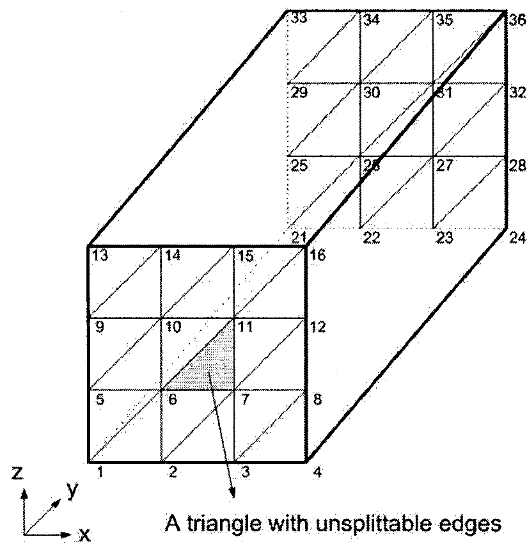

Fig. 4.2 Identical surface mesh at periodic boundary pairs.

Geompack++ is provided as a Windows executable that interfaces with applications via special file formats. Through input files one defines the geometry to be meshed and the desired meshing operations. The output file contains information about the subdivided geometry.

Geometry definition

The geometry is defined by two text (ASCII) files; `Region.rg3` and `CurveSurface.cs3`. The 3D region file consists of four groups of information: vertices coordinates, vertices extra-info records, loops and shells. The first logical record contains x, y and z coordinates of the nodes upon which the geometry is built. Miscellaneous information about nodes, if any at all, is saved in a separate group called vertices extra-info record. Loops (boundary of a simple face), once put together, define surfaces and shells (boundary of a subregion or interior space hole) are used to indicate different material types or interior holes within the geometry. Associated with each 3D region file, there is a 3D curve/surface file that consists of information on the curves and surfaces of the region. In the simplest case, curves are line segments connecting two or more nodes and surfaces are planar facets over which curves and loops topologically lie. Furthermore, each labeled surface can be assigned a boundary condition code for different types of boundary conditions. A detailed description of the region and curve/surface file formats is available in [77].

In order to have Geompack++ generate a mesh that is identical at periodic boundary pairs, similar grids are utilized for each master/slave pair. Then all the loops that topologically lie on these surfaces are defined using unsplittable edges and faces (Refer to [77] and Fig. 4.2). This way, it is ensured that no extra nodes are introduced to master/slave surfaces during the mesh generation process.

Meshing operation

Once the geometry is defined properly, many meshing operations can be performed on it by invoking the Geompack++ executable `zgp`. As input, `zgp` requires a text (ASCII) file `Oper.in` that contains the meshing operation code, operation-dependent meshing fields and names of region, curve/surface and mesh files. Operation code 302 generates a tetrahedral mesh given a 3D region of interest. More information on input/output file format and meshing operations carried out by Geompack++ is available in [78].

A mesh file `Mesh.msh3` will then be generated if no inconsistency errors occur during the meshing operation. The 3D mesh file format consists of five groups of information: vertices information, vertices extra-info record, element nodes, element faces and constrained mesh edges [77]. In `Mesh.msh3`, a region code is assigned to each element associated with various material types defined in `Region.rg3`. Element faces also have boundary condition codes according to those defined in `CurveSurface.cs3` for labeled surfaces.

The mesh file format produced by Geompack++, however, is not compatible with the tetrahedral mesh files accepted by P3D and therefore has to be further processed to comply with the required P3D formats. Postprocessing of `Mesh.msh3` yields two of the required input files to P3D: `Tets.dat` and `Topology.dat`. The former is initially read in by P3D to obtain the required mesh information such as actual nodes labeling and their spatial coordinates, tetrahedral elements and their associated boundary condition and region codes.

The latter is read in during Dofs generation and contains the same information as `Tets.dat` but this time with virtual node labels. In `Topology.dat` a mesh node that topologically lie on the slave surface of a periodic boundary pair is given the same label as the one it matches on the corresponding master surface. Therefore, a virtually wrapped geometry is formed by connecting the unit-cell closures at periodic boundary pairs (see Fig. 4.3). This way, the elements edges and faces that lie on master/slave surfaces share their associated degrees of freedom, as required by Eq. (4.24).

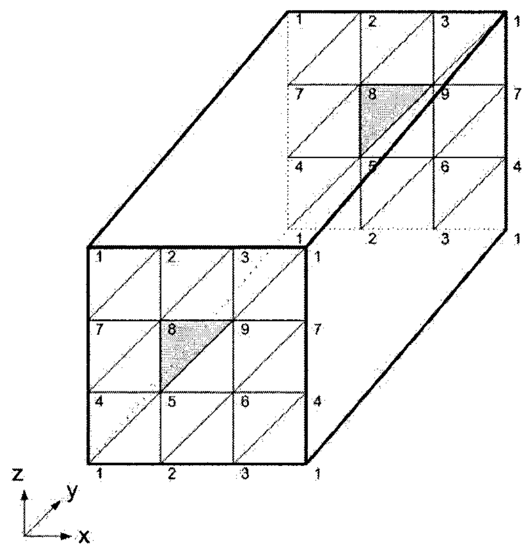

Fig. 4.3 Virtual node labels on slave surfaces.

4.2.2 Finite Element Code

Having discretized the unit-cell into tetrahedral elements, the next step is to generate the degrees of freedom associated with edges, faces and volume of each tetrahedron. In this work, a 3D finite element code, called P3D, is utilized for Dofs generation and FE matrix assembly. P3D is a FE-based code written mainly in C++ which solves Maxwell's equations in the time-harmonic regime. Essentially, it solves the vector wave equation for the electric field.

P3D was first released in 1999 [79] and originally developed to extract the scattering parameters of microwave devices [73]. It was further extended in [80] to handle eigenmode analysis of periodic structures. The latter is implemented using the formulation given in [12] and thereby is not suitable for a complex eigenmode analysis proposed in this thesis. To that goal, the author has added a number of routines to P3D that make the complex eigenmode analysis, and therefore the stopband characterization, feasible. Before we concentrate on the implementation details of P3D, some of the required input files for its correct functioning are outlined below.

Required input files

Along with `Tets.dat` and `Topology.dat`, three other input files are required by P3D to compile:

- `Matl.dat` defines material properties (permittivity, permeability) for each region. Material properties are considered symmetric tensors, thus six complex values are needed for each.

- `BCs.dat` assigns boundary conditions to labeled surfaces. P3D, obviously, imposes no constraints on the field on a surface labeled PMC since it solves for the electric field. On the contrary, the tangential electric field is forced to zero on a surface labeled PEC. Other boundary conditions are allowed [73]. Also note that the unit-cell closures are labeled PMC (natural boundary condition); Periodic constraints are imposed through the formulation, later on.

- `Univ.bin` contains various universal matrices used at run time to build the local matrices $[S^e]$ and $[T^e]$. The universal matrix approach, introduced in [81], allows for efficient computation of the integrals given in Eqns. (4.20) and (4.21), using symbolic mathematics softwares (e.g. Maple).

Generation of the degrees of freedom

One of the great advantages of object-oriented programming (OOP) languages like C++ is the ease with which object-oriented codes are modified. The magic of OOP mainly lies beyond the fact that data structures and functions are encapsulated into packages called *classes*. Objects are different instances of these classes and inherit some of the properties of the class from which they are instantiated. However, their implementation information is hidden in the object and is not accessible nor needed during the hand shake with other objects. Therefore, changes to existing modules (classes and their objects) does not introduce major modifications, if any at all, to other classes. Furthermore, new modules are easily integrated into the code using well-defined interfaces [82].

Classes that were reused from P3D are namely `Mesh`, `Topology`, `Field`, `Neighbor` and `SparseMatrix`. The FE code starts by instantiating a `Mesh` object and a `Topology` object which read mesh from `Tets.dat` and `Topology.dat`, respectively. A `Field` object is created next which is used for generating the degrees of freedom. Dofs are generated by calling `field->generateDofs()`. The degrees of freedom are associated with element edges, faces and volume. For each element, a list of neighboring elements is formed (using a `Neighbor` object) to check whether its edges or faces are shared by an earlier element; if an edge or face is shared with an earlier neighbor, the degree of freedom associated with that edge or face is taken from the list. If not, a new Dof is generated. The volume Dofs are not shared, therefore new ones are generated for each element. Thereafter, function `buildConstraints()` finds which Dofs should be constrained due to boundary conditions. Constrained Dofs are then set to zero and eliminated from the system of equations.

Finally, the sparsity pattern of the local matrices `localS` and `localT`, is built and the contribution of each element is added to the sparsity pattern of the global matrices `globalS` and `globalT`, respectively. In the main body of the code, P3D calls a function named `Assemble()` that instantiates local/global matrix objects using the `SparseMatrix` class. `SparseMatrix` is specifically defined for saving nonzero elements of the lower triangle of sparse symmetric matrices. `globalS` and `globalT` are then written to text files for transmission to the eigensolver.

Rearranging the degrees of freedom

As required by Eq. (4.30), identical Dofs should be assigned to the elements edges and faces that topologically lie on the slave surface of a periodic boundary pair and their counterparts on the master surface. This is achieved in [80] by replacing the `Topology` class during Dofs generation instead of the original `Mesh` class, which virtually connects the mesh at periodic boundary pairs. With this implementation, the contributions of the master and slave Dofs add to the same row of the global FE matrices $[\bar{\mathrm{S}}]$ and $[\bar{\mathrm{T}}]$; Therefore, the slave Dofs are automatically eliminated from the system of equations during the matrix assembly.

On the other hand, Eq. (4.32) requires that the contributions of the master and slave Dofs account for separate rows in the global FE matrices [S], [T] and the slave Dofs be reduced after the assembly process by introducing the matrices $[\bar{C}]$ and $[\bar{G}]$. For this purpose, two new functions were added to the `Field` class: `generateSlaveDofs()` and `reOrderDofs()` so that the available version of P3D could be exploited for the assembly process. The former assigns new labels to the degrees of freedom associated with the slave surface of the periodic boundary pair under consideration. Furthermore, it ensures that the orientation of new slave Dofs is identical to that of the existing master Dofs. The latter reorders the degrees of freedom in the Dofs list (array) so as to have interior Dofs first and then the master Dofs and slave Dofs respectively after, in the list. The degrees of freedom are generated on an element-by-element basis and therefore sorted in the Dofs list based on the numbering of elements. The function `reOrderDofs()` rearranges them according to the order given in (4.23) so that the resulting global matrices assembled by P3D can be treated the way shown in Eq. (4.33).

Order of elements

The use of high-order edge elements in solving vector electromagnetic problems by FEM, is now well-established and recognized as a computationally efficient approach [83]. In combination with the more conventional mesh refinement (h-adaption), increasing the order of elements (p-adaption) can lead to exceptional performance [84].

The general high-order elements have two separate function spaces for representing the interpolation bases: gradient and rotational. The gradient order represents irrotational functions with zero curl while the rotational order has a set of functions with nonzero curls. There are many advantages to this separation of function spaces. One such benefit is the optimal representation of a vector field in an electromagnetic problem where its curl dominates [79]. Note that if a field is represented as a polynomial of order p, its curl is a polynomial of order $p-1$. Thus, when the gradient and rotational spaces are both complete to pth order, the result is an element which is complete to order p. This is not necessarily an optimal choice. A better balance in the accuracy of representing the field and its curl is obtained by removing those degrees of freedom that do not affect the curl, i.e. when the gradient order is one less than the rotational order and the element is complete to $p-1$th order.

P3D makes use of tetrahedral edge elements of arbitrary order [79] to set up the vector trial functions. At run time, the elements order is decided first, by a function call `field->fixorders()` and then Dofs are generated according to that order. Each element has gradient and rotational degrees of freedom associated with its six edges, four faces and the interior volume. The high-order elements employed herein, allows the utilization of a coarse mesh with relatively low number of elements in the computer simulations.

4.2.3 Eigensolver

The proper choice of an eigensolver is mainly affected by the structure of the matrices defining the problem as well as the spectral properties of the eigenvalue problem itself. QEPs [85] are a class of nonlinear eigenvalue problems that are less familiar and less routinely solved than the standard GEPs [86]. Furthermore, Eq. (4.32) is an ill-posed eigenvalue problem, due to the singularity of $[\mathrm{M}_2]$ and $[\mathrm{M}_3]$. Therefore, great attention has to be devoted to the numerical solution of the eigenvalue problem raised here.

Solution technique

The QEP is to find scalars λ and nonzero vectors x, y satisfying

$$(\lambda^2 M + \lambda C + K)x = 0, \qquad y^*(\lambda^2 M + \lambda C + K) = 0 \tag{4.34}$$

where M, C and K are $n \times n$ matrices with complex entries and x, y are the right and left eigenvectors, respectively, corresponding to the eigenvalue λ.

A major division in the solution methods for the QEP is between those that deal with the original form of the QEP [87], [88] and those that first linearize it into a GEP of twice the dimension and then apply GEP techniques [86]. Most of the numerical methods that treat the problem in its original form are variants of Newton's method [89]. There are two drawbacks to these Newtonian variants: (a) they compute one eigenpair at a time and (b) even for a good initial guess, there is no guarantee that the method converges to the desired eigenvalue. Here, we concentrate on the alternative option, i.e. methods that compute *all* the eigenvalues and eigenvectors of the QEP through one of its linearizations. The cost is to solve a problem of twice the dimension of the original problem.

The easiest way to construct a linearization, also employed in this thesis, is to use a substitution such as $u = \lambda x$ in $(\lambda^2 M + \lambda C + K)x = 0$ and rewrite the equation as

$\lambda Mu + Cu + Kx = 0$ [85]. This yields the GEP

$$\begin{bmatrix} 0 & I \\ K & C \end{bmatrix} \begin{bmatrix} x \\ u \end{bmatrix} - \lambda \begin{bmatrix} I & 0 \\ 0 & -M \end{bmatrix} \begin{bmatrix} x \\ u \end{bmatrix} = 0 \tag{4.35}$$

which has $2n$ eigenvalues/vectors. A linearization is not unique and the choice between different companion forms is problem-dependent. A more detailed description of the commonly used companion forms of a QEP is given in Appendix A.

There is a second division based on the properties of the matrices; direct methods [90] for dense, small- to medium-sized problems and iterative methods [91] for large scale problems. The former techniques compute all the eigenvalues while the latter compute a few eigenvalues and, upon request, eigenvectors. A major drawback to methods used for dense problems is that they usually destroy any sparsity in the matrices forming the problem. This leads to large memory requirements and high execution times for QEPs of large dimension. On the contrary, in large-scale applications, matrices are usually sparse and stored in spacial data structures. This limits the type of operations one can perform on matrices and often iterative methods require matrices with special properties (e.g., symmetric, positive definite) for their efficient functioning.

Owing to singularity of [M_2] and [M_3], the matrices yielded from the linearization of Eq. (4.32) are neither symmetric nor positive definite. Indeed, the resulting $2n \times 2n$ matrices in the linear problem inherit this singularity which diminishes the use of an iterative solver. Generalized singular value decomposition (GSVD) techniques for large sparse matrix pairs have been reported [92] but not realized as a software package, yet. Therefore, direct methods are preferred for the present work.

The crucial role of the higher-order finite elements utilized in this thesis, is now more vivid. With high-order elements, one avoids employing a fine mesh thus deals with a smaller number of unknowns. This leads to a medium-sized matrix equation that can be handled by direct solvers while still maintaining a good accuracy.

Software tool

Most linear algebra-related software packages include subroutines that implement a widely used decomposition method for the numerical solution of GEPs, called QZ algorithm [90].

This thesis exploits MATLAB's built-in functions to solve the QEP. In MATLAB, the `polyeig(`K, C, M`)` command is an implementation of the QZ algorithm which returns the $2n$ eigenvalues and, optionally, the right eigenvectors. The alternative way is to build the linearized GEP using Eq. (4.35) and use the command `eig(·)` to obtain the eigenpairs.

4.3 Simulation Results

This section presents the simulation results for different test cases. Three simulation models are investigated to verify proper functioning of the developed FE code. Firstly, a singly periodic structure is considered. The second model is a doubly periodic array of metal rods. Lastly, a triply periodic array of metal cubes is examined. In each experiment, complex propagation constants are obtained for different directions of propagation vector. Both real and imaginary parts of the propagation constant are plotted versus frequency which characterize the passband and stopband behavior of the periodic structures, respectively. For the case of a stratified periodic medium (singly periodic problem), numerical simulations are compared to analytical solutions. For the two last problems, the results obtained for the imaginary part of the propagation vector are compared to the dispersion curves presented in [12], [93]. There are no published results on the real part solutions for these two cases.

4.3.1 Electromagnetic Kronig-Penney (EKP) model

The first configuration considered was the electromagnetic equivalent of the Kronig-Penney model in quantum mechanics [94]. The EKP model is a repeated pattern of two infinite layers of given permittivity, permeability and width (Fig. 4.4(a)). Its 3D unit cell is shown in Fig. 4.4(b).

Two experiments were carried out to obtain the TEM modes of the configuration. In the first experiment (Fig. 4.5), the propagation vector β was specified and frequency solutions (k_0) were found using Eq. (4.30). In the second experiment (Fig. 4.6), k_0 was specified and the Floquet constant corresponding to periodic variations along x-axis (γ_x) was found using Eq. (4.32). Fig. 4.6(a) depicts the imaginary part of the complex propagation constant and Fig. 4.6(b) shows its real part. In both trials, we found a very good agreement between the FEM results and those of the analytic solution given in [12].

Further inspection of Fig. 4.6 reveals that $\mathrm{TEM}_{(2,0,0)}$ and $\mathrm{TEM}_{(3,0,0)}$ modes captured in higher frequency ranges are, indeed, continuations of the fundamental $\mathrm{TEM}_{(1,0,0)}$ mode. Depending on k_0 (frequency) , this TEM mode exhibits various characteristics. Up to

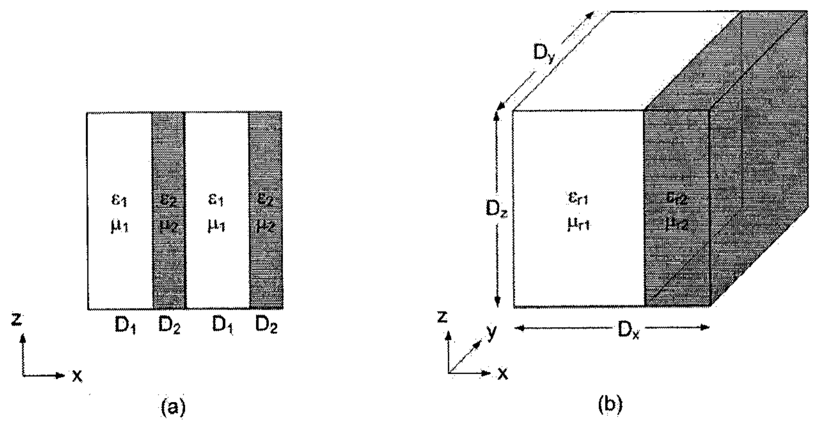

Fig. 4.4 EKP model: (a) side view, and (b) its 3D unit-cell. $D_x = 0.3$, $D_y = D_z = 0.1m$, $D_1 = 2D_2 = 0.2m$, $\epsilon_{r1} = \mu_{r1} = \mu_{r2} = 1$, $\epsilon_{r2} = 9$.

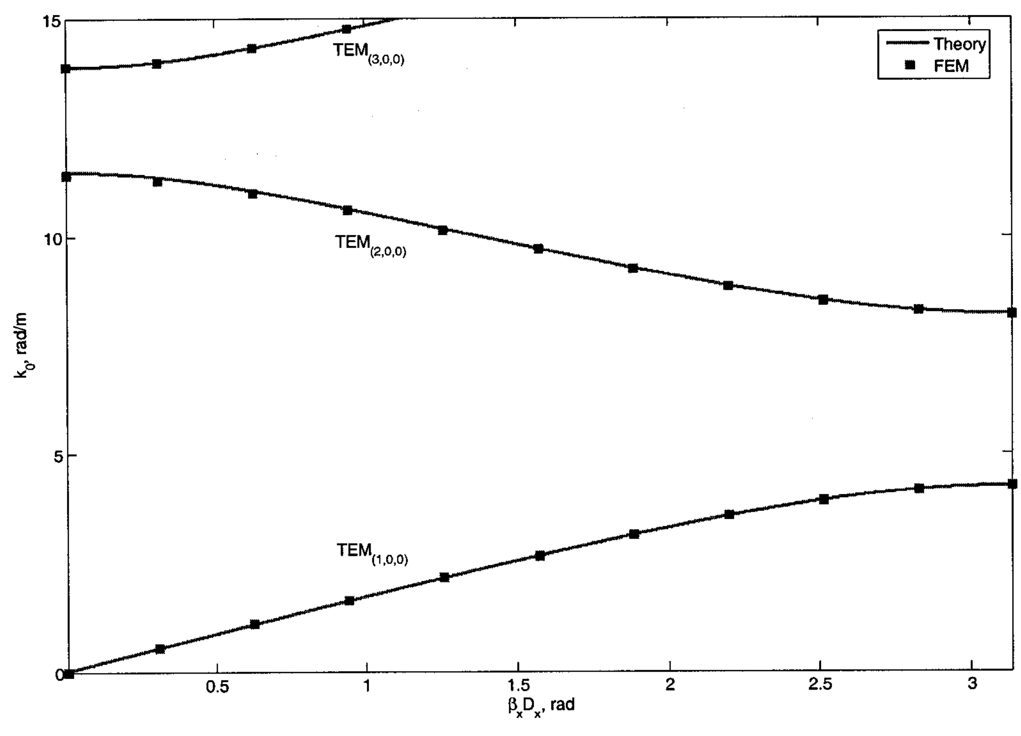

Fig. 4.5 Dispersion curves of the EKP model for TEM modes.

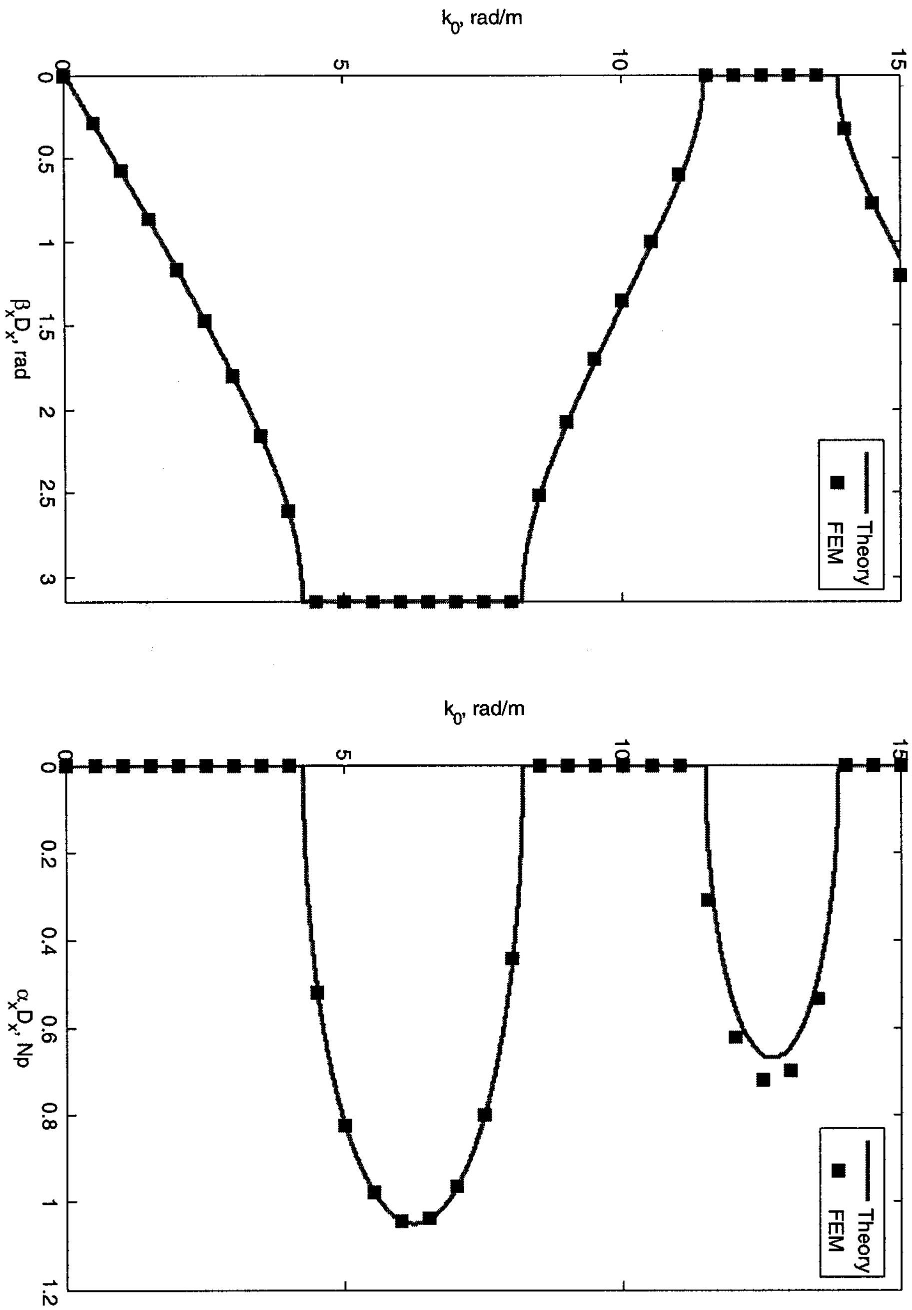

Fig. 4.6 Complex propagation constant of the EKP model: (a) imaginary part, and (b) real part.

4.24 rad/m, $\text{TEM}_{(1,0,0)}$ is a propagating mode with a purely imaginary propagation constant ($\gamma_x = j\beta_x$) and its phase constant ($\beta_x D_x$) increases from 0 to π radians. Within the range 4.24–8.18 rad/m, it becomes a complex mode ($\gamma_x = \alpha_x + j\beta_x$), maintaining a phase change of π along the unit-cell boundaries while its attenuation constant ($\alpha_x D_x$) changes between 0 and 1.1 Nepers. Beyond 8.18 rad/m it propagates again with the phase constant now decreasing from π to 0. At 11.38 rad/m attenuations start and the mode becomes evanescent ($\gamma_x = \alpha_x$) and so on for higher frequencies. This result proves the capability of the FE program in capturing complex modes in general and the stopband characterization in particular.

For both experiments, a mesh consisting of 18 tetrahedra was employed. High-order tetrahedral elements of gradient order 2 and rotational order 3, from now on referred to by a pair of indices (2,3), were utilized. The FE program assigns 45 degrees of freedom (16 gradDof and 29 rotDof) to each element which adds up to 324 for the entire unit-cell. Each point of the FEM curves is obtained in 68 seconds with a 1.53 GHz, 1 GByte RAM PC. In order to capture TEM modes, PEC and PMC boundary conditions were imposed on x-y, x-z surfaces (boundary closures) of the unit-cell, respectively. γ_y and γ_z were set to zero in the assembly process which, along with PEC and PMC boundary conditions, correspond to purely transverse field vectors, both **E** and **H**. In other words, we have been looking for solutions that have no variations with y and z.

4.3.2 Doubly Periodic Array of Metal Rods

The next simulation model considered was a doubly periodic array of infinitely long (in z-direction) and perfectly conducting metal rods (see Fig. 4.7(a)). The 3D unit cell of the geometry is shown in Fig. 4.7(b). Since we are only considering solutions that have no variations along z, field solutions in such structures are either transverse electric (TE) or transverse magnetic (TM). The TE modes are obtained by imposing PMC on the top and bottom planes of the unit-cell while imposing PEC on these planes yields the TM modes. Here, TM modes are investigated due to the smaller size of the resulting FE matrices –the degrees of freedom associated with top and bottom surfaces are forced to zero in this case (PEC boundary condition) and finally eliminated from the system of equations which yields a relatively smaller matrix equation compared to the one built for TE modes.

Again the problem was tackled in two different ways. Fig. 4.8 shows the first set of

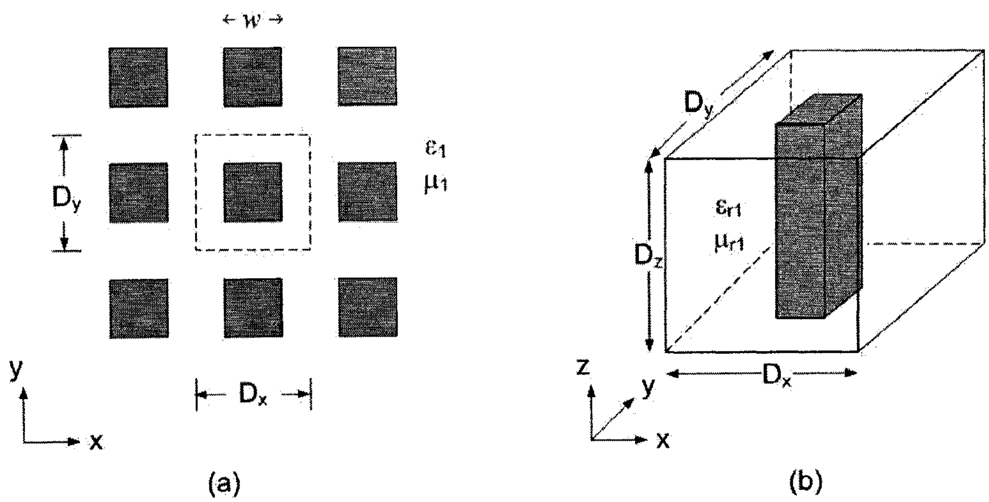

Fig. 4.7 Doubly periodic array of infinitely long metal rods: (a) top view, (b) its 3D unit-cell. $D_x = D_y = 1m$, $D_z = 0.75m$, $w = 0.5m$, $\epsilon_{r1} = \mu_{r1} = 1$.

dispersion curves obtained by specifying a propagation vector and solving for permitted frequencies. The accuracy of these results were verified by the FE code used in [80]. A very good agreement was found between the two results. The so called $k - \beta$ diagram of Fig. 4.8 has two regions; the first region (A $\rightarrow$ B), is generated by setting β_y to zero and varying $\beta_x D_x$ from 0 to π. In the second region (B $\rightarrow$ Γ), $\beta_x D_x$ is fixed to π and $\beta_y D_y$ varies from 0 to π. Simulation results revealed that no TM mode could propagate below $k_0 = 4.18$ rad/m. Therefore, the k_0 range shown in Fig. 4.8 was intentionally chosen for the following fixed-k_0 experiments.

The second set of curves (Figs. 4.9, 4.10), are obtained by specifying k_0 and finding complex propagation constants γ_x and γ_y, each at a time. Note that γ_z was set to zero in all experiments. Fig. 4.9(a) represents the imaginary part of γ_x and Fig. 4.9(b) depicts its real part. These curves were obtained by setting γ_y to zero. Indeed, Fig. 4.9(a) corresponds to region A $\rightarrow$ B of Fig. 4.8 and the TM modes found in both trials perfectly match. However, Fig. 4.9 provides more information on the origin of each mode and their behavior in different frequency regions.

Firstly, the complex eigenmode analysis (see Fig. 4.9) reveals that only three of the four TM modes encountering in the k_0 range shown here are independent. The fourth mode (blue squares) is in fact a continuation of the second mode. Moreover, as in the EKP model, each of these modes follows a different trend in each frequency range. For instance, TM1 (green

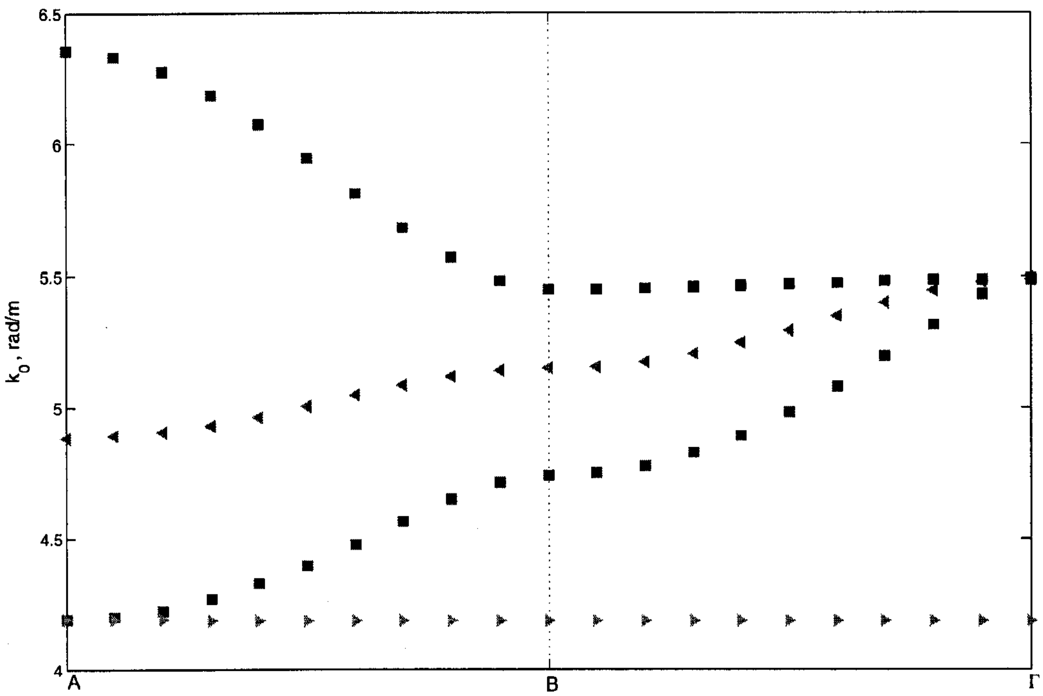

Fig. 4.8 Dispersion of TM modes of the doubly periodic array of metal rods.

triangles in Fig. 4.9) is a complex mode ($\beta_{1x}D_x = \pi$) with high attenuation ($\alpha_{1x}D_x \gg 1$) in low frequency regions. In a short frequency range it propagates ($\gamma_{1x} = j\beta_{1x}$) and experiences a phase change from π to 0. Thereafter, it becomes evanescent ($\gamma_{1x} = \alpha_{1x}$) and dies out rapidly ($\alpha_{1x}D_x \gg 1$). The second mode (TM2) is initially evanescent ($\gamma_{2x} = \alpha_{2x}$); then propagates ($\gamma_{2x} = j\beta_{2x}$) until it becomes a complex mode ($\gamma_{2x} = \alpha_{2x} + j\beta_{2x}$) with a phase change of π radians. At $k_0 = 5.4$ rad/m it starts to propagate again with the phase change now varying from π to 0, and finally it turns back evanescent at higher frequencies. Lastly, TM3 found to be evanescent ($\gamma_{3x} = \alpha_{3x}$) up to $k_0 = 4.85$ rad/m and propagates ($\gamma_{3x} = j\beta_{3x}$) in the range (4.85–5.15). Beyond $k_0 = 5.15$ rad/m, it supports a complex mode ($\gamma_{3x} = \alpha_{3x} + j\beta_{3x}$) with π phase change along the unit-cell.

Fig. 4.10 shows the imaginary and real parts of the complex propagation constant γ_y once $\gamma_x D_x = j\pi$. Here, $\frac{j\pi}{D_x}$ was chosen for γ_x, according to the value assigned to β_x in the second region of Fig. 4.8. We found excellent correspondence between Fig. 4.10(a) and region B $\rightarrow$ Γ of Fig. 4.8. The propagating TM modes of the structure can then be identified using Fig. 4.8 or Fig. 4.10(a); while, more information about the nature of each

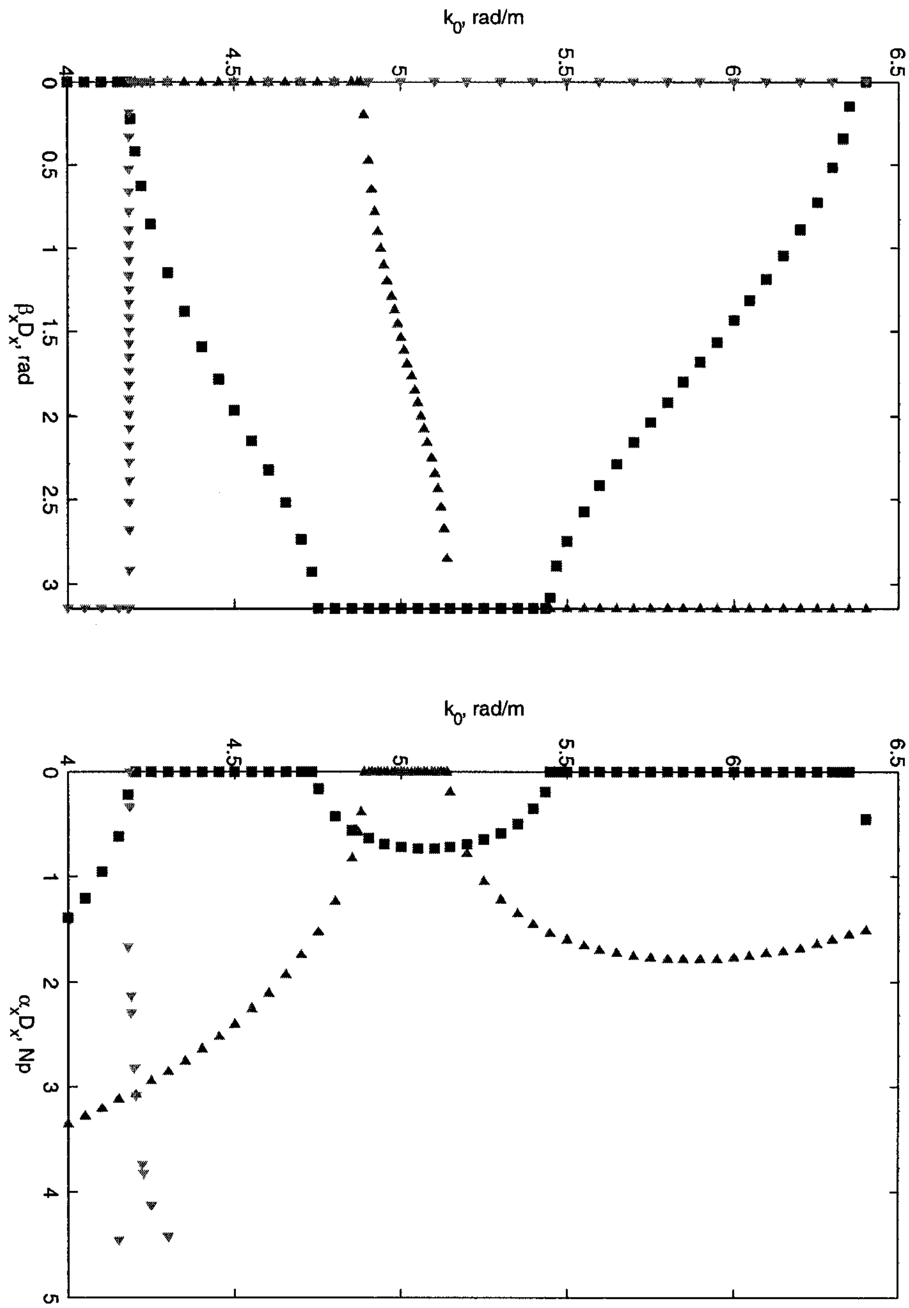

Fig. 4.9 Complex propagation constant of the doubly periodic array in region A → B: (a) imaginary part, and (b) real part.

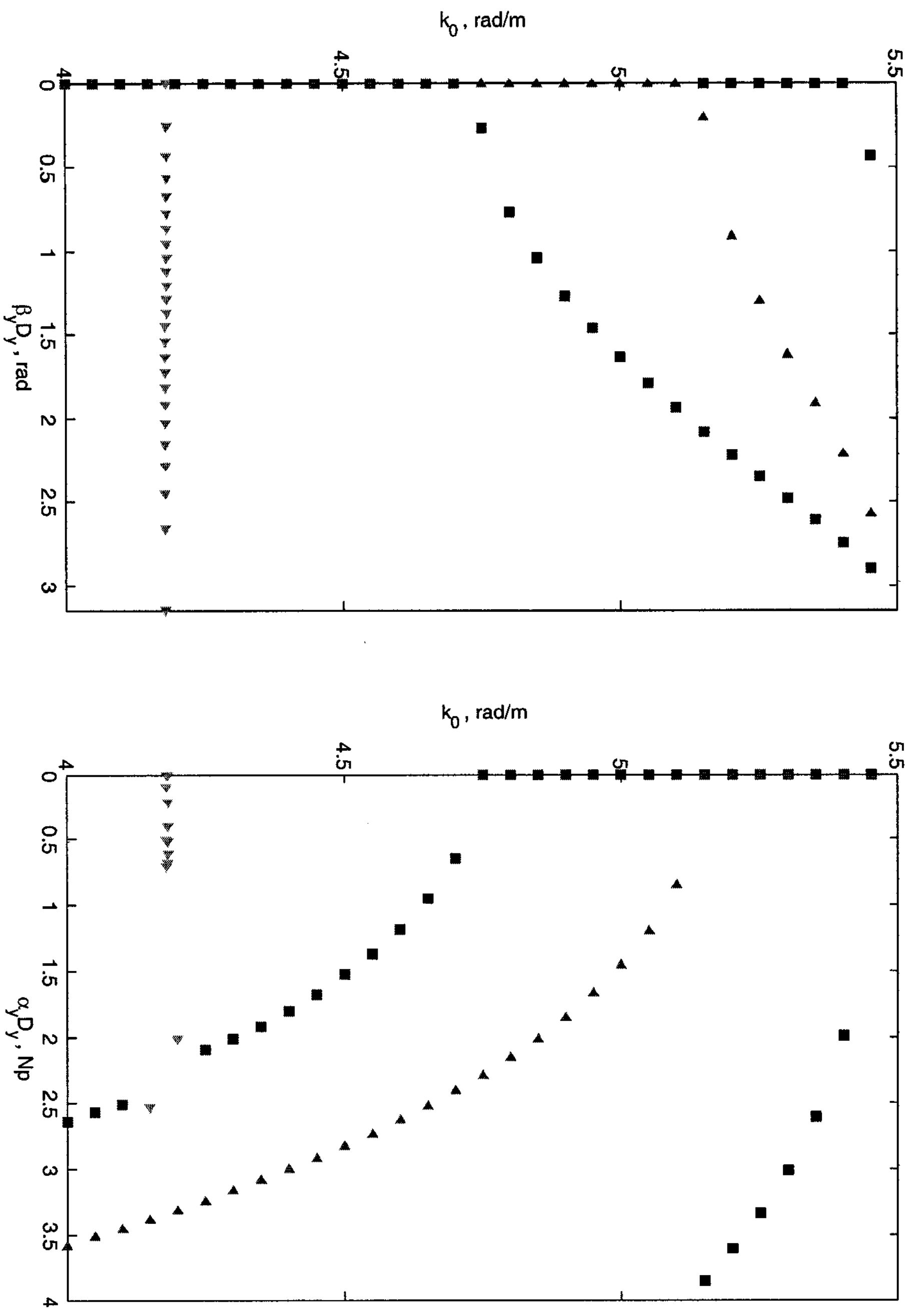

Fig. 4.10 Complex propagation constant of the doubly periodic array in region B $\rightarrow$ Γ: (a) imaginary part, and (b) real part.

mode, their behavior as a function of frequency and the attenuation along the unit-cell are given in Fig. 4.10(b).

In all trials, a mesh consisting of 84 tetrahedra of order (2,3) was employed. The resulting system of equations had a total 1185 degrees of freedom. Each point of the fixed-k_0 curves is obtained in 267 seconds on the same computing platform. Obviously, with a dense solver, simulations time increases as the number of Dofs increases. As a rule of thumb, n-times larger systems are solved in about n^3 greater time.

4.3.3 Triply Periodic Array of Metal Cubes

Lastly, the triply periodic array of perfectly conducting metal cubes in Fig. 4.11 was examined. Also shown in the figure is the 3D unit-cell of the structure. Simulation results are shown in Figs. 4.12– 4.15. Fig. 4.12 represents the dispersion curves obtained from fixed-γ experiments. These results are in a very good agreement with those presented in [93] for the same structure. In [93], only three of the five modes depicted here are presented.

Each region of Fig. 4.12 corresponds to a distinct set of Floquet triples (β_x,β_y,β_z). In the A $\rightarrow$ B, β_y and β_z are fixed to zero and $\beta_x D_x$ varies from 0 to π with an incremental step of $\frac{\pi}{10}$. In the B $\rightarrow \Gamma$, β_z is fixed to zero and β_x is set to $\frac{\pi}{D_x}$; in this case $\beta_y D_y$ varies from 0 to π with the same incremental step, $\frac{\pi}{10}$. Finally, in the $\Gamma \rightarrow \Delta$ region of the diagram, $\beta_x D_x$ and $\beta_y D_y$ are both set to π and $\beta_z D_z$ varies from 0 to π.

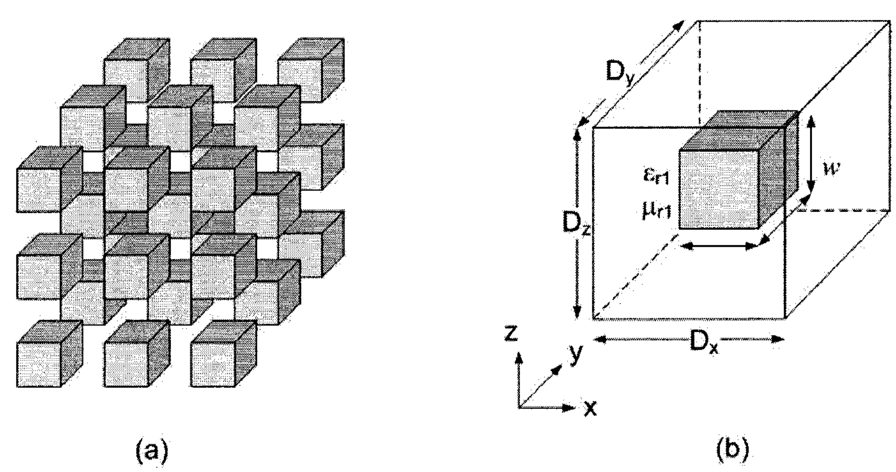

Fig. 4.11 Triply periodic array of perfectly conducting metal cubes: (a) 3D view, and (b) its unit-cell. $D_x = D_y = D_z = 1m$, $w = 0.5m$, $\epsilon_{r1} = \mu_{r1} = 1$.

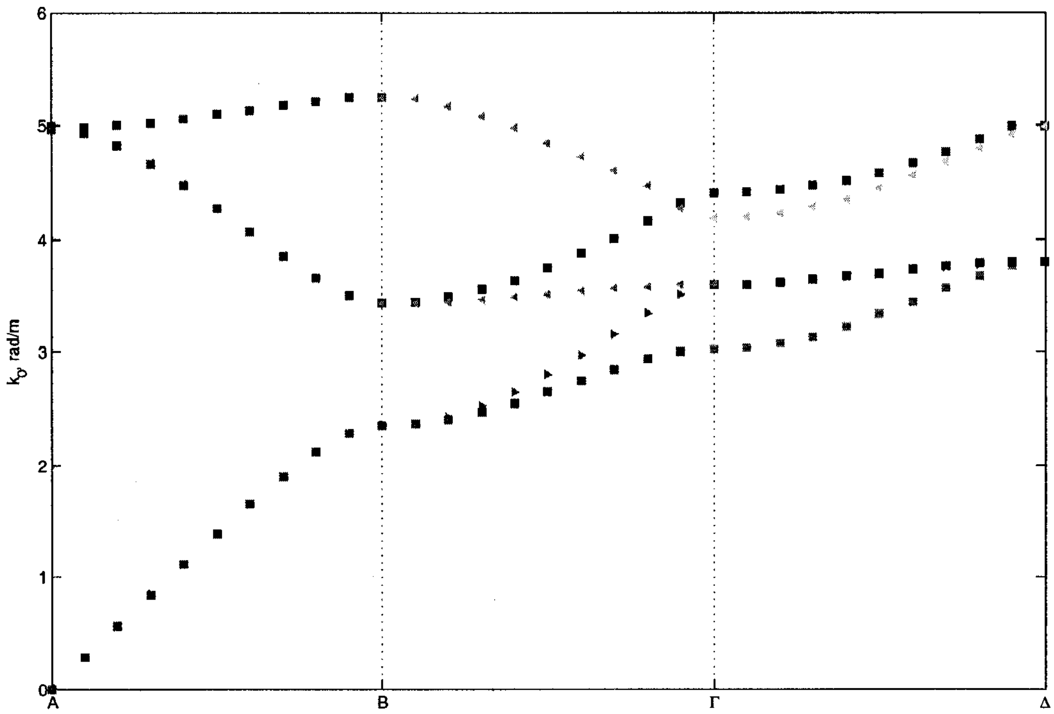

Fig. 4.12 Band structure of the triply periodic array of metal cubes.

Associated with each region of the $k-\beta$ diagram, we performed three separate trials. In each trial a k_0 value and two of the three components of the triple $(\gamma_x, \gamma_y, \gamma_z)$ were specified and the other component of the complex propagation vector was found. Fig. 4.13 shows the imaginary and real parts of γ_x as a function of frequency, where γ_y and γ_z were both set to zero. Subsequently, the imaginary and real parts of γ_y are plotted versus frequency in Fig. 4.14. These curves were obtained by setting γ_x equal to $\frac{j\pi}{D_x}$ while maintaining γ_z at zero. Finally, $\gamma_x D_x$ and $\gamma_y D_y$ are set to $j\pi$ and γ_z is sought, yielding Fig. 4.15. The challenge here was to trace each individual curve when two curves cross, as in Figs. 4.14 and 4.15.

The mesh employed here consisted of 154 tetrahedral (2,3) elements resulting in 2778 degrees of freedom. Owing to the large number of Dofs, the required time to solve each matrix equation dramatically increased compared to singly and doubly periodic models. Each point of the fixed-k_0 curves for the triply periodic array was found in 2900 seconds.

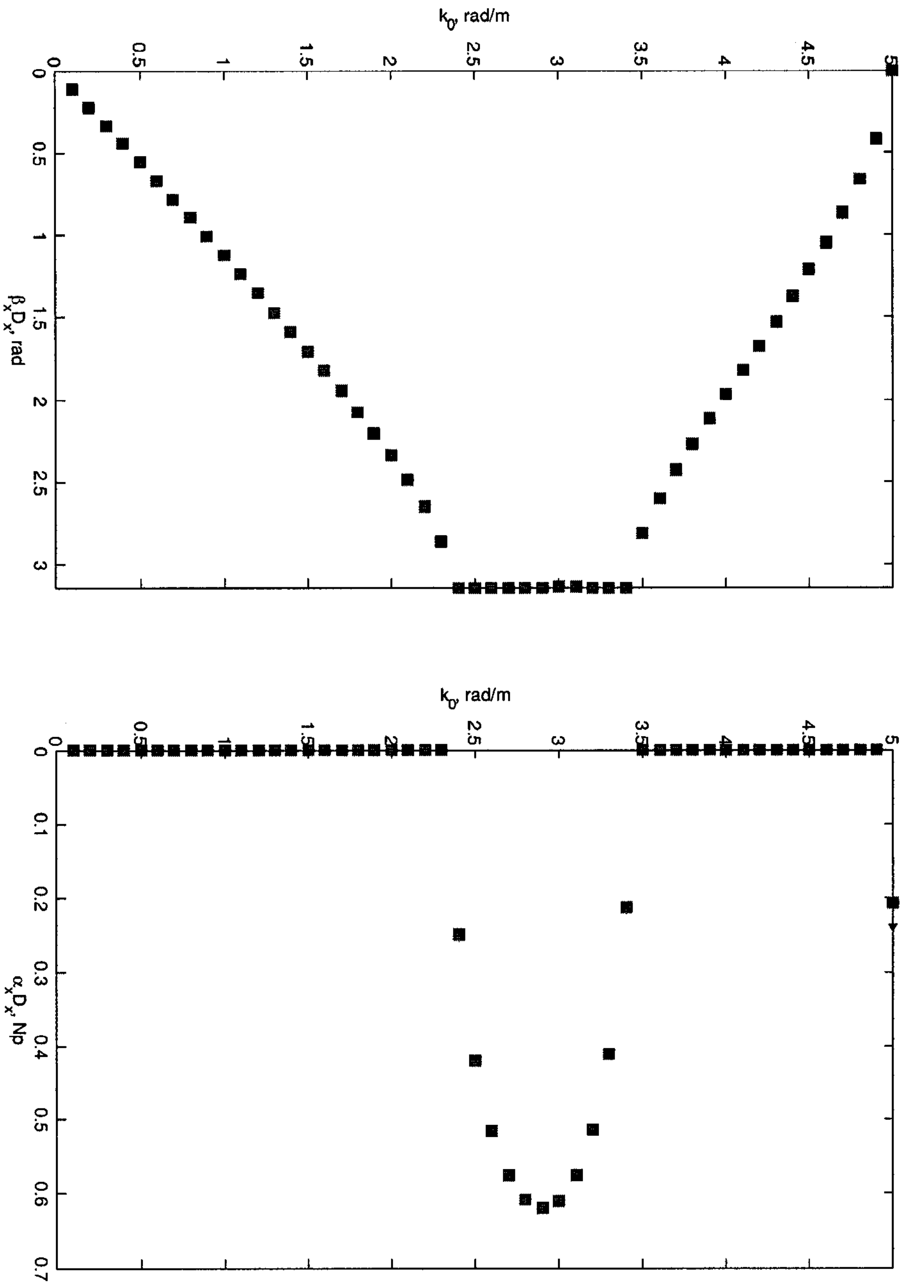

Fig. 4.13 Complex propagation constant of the triply periodic array in region A → B: (a) imaginary part, and (b) real part.

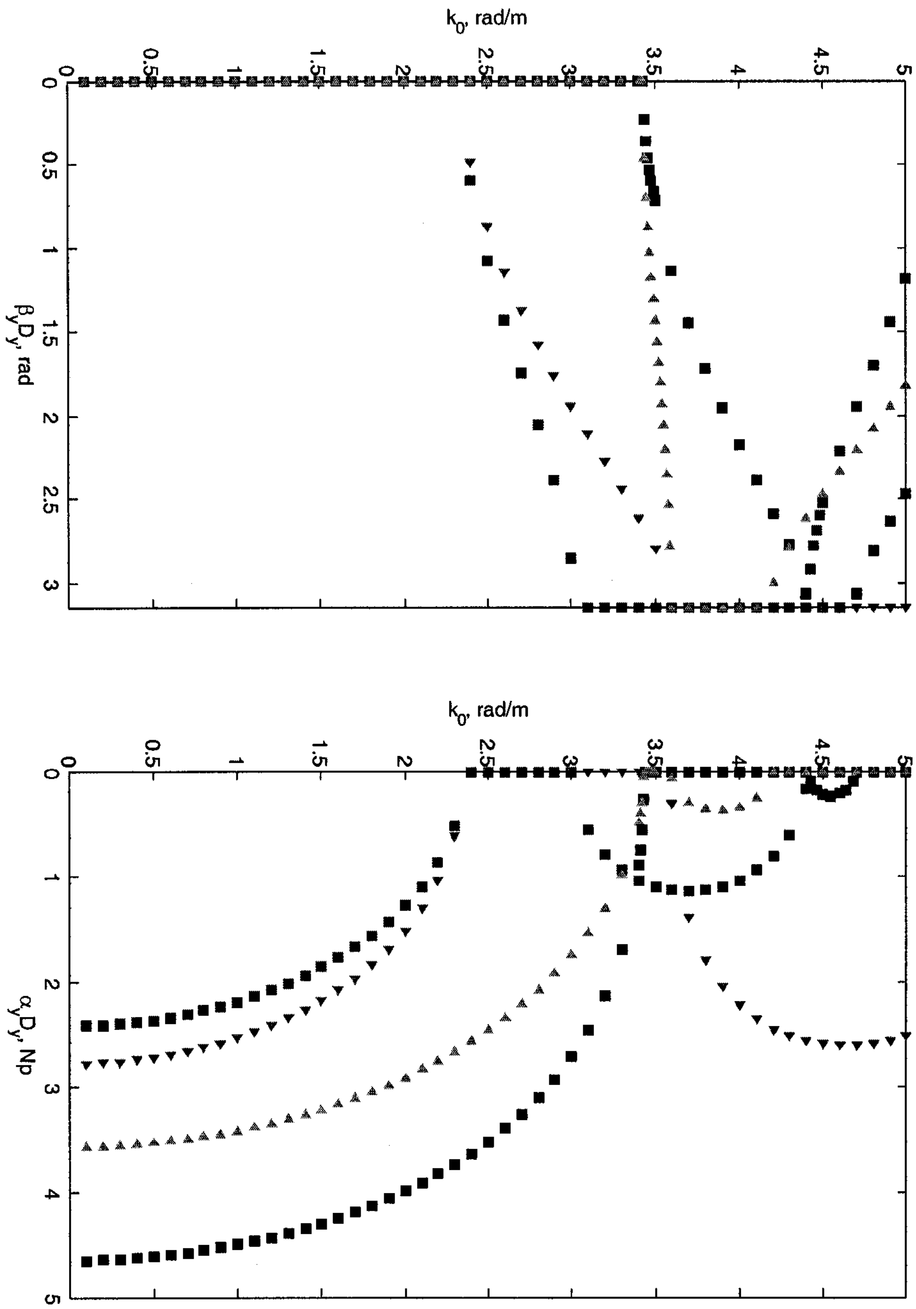

Fig. 4.14 Complex propagation constant of the triply periodic array in region B → Γ: (a) imaginary part, and (b) real part.

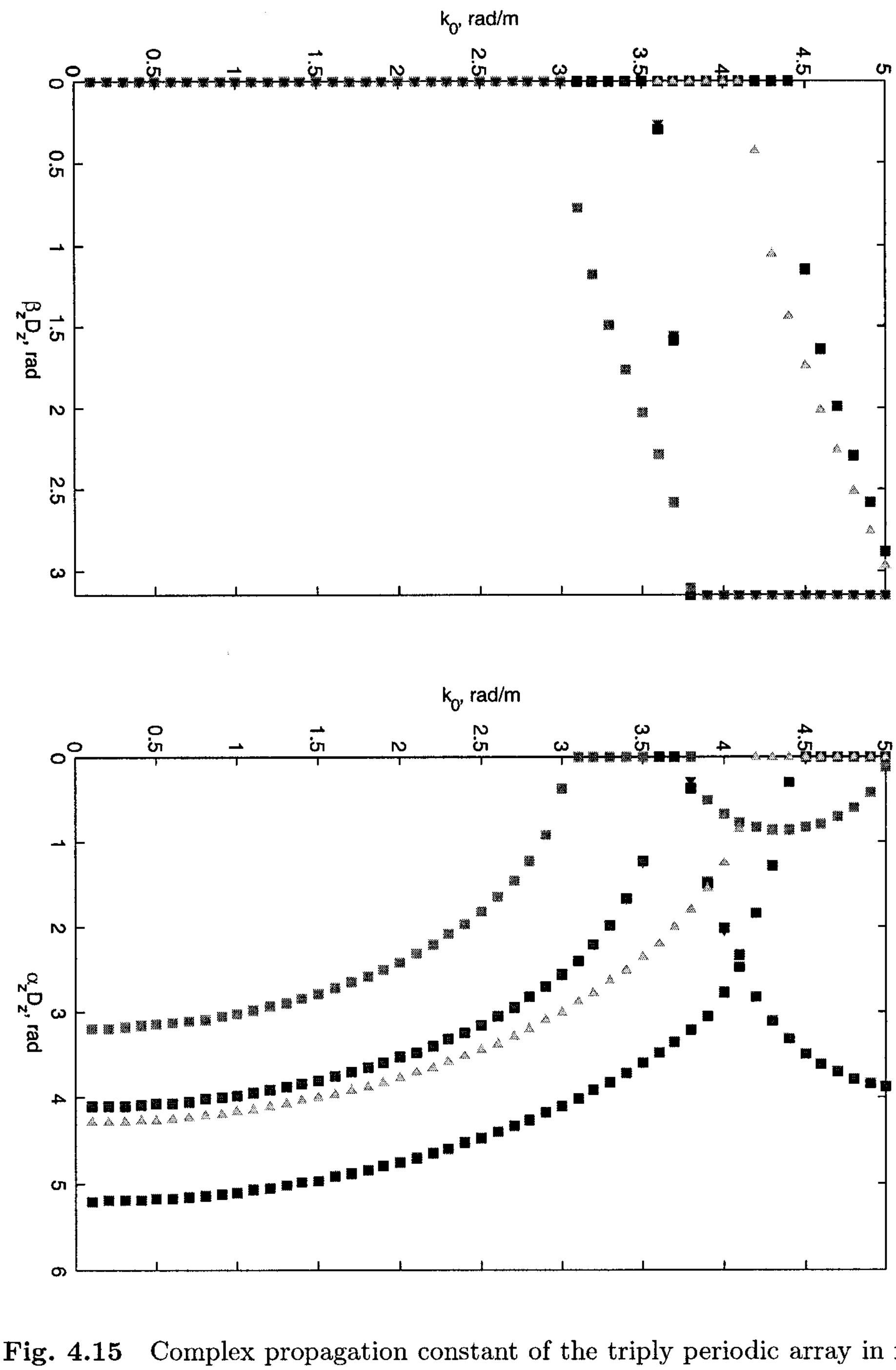

Fig. 4.15 Complex propagation constant of the triply periodic array in region $\Gamma \rightarrow \Delta$: (a) imaginary part, and (b) real part.

4.4 Discussion

The aim here was to develop a finite element system, capable of handling complex eigenmode analysis and predicting the stopband behavior of evanescent modes in periodic structures. That goal was achieved and the accuracy of the developed FE code was tested on different simple geometries with periodicity in one, two or three dimensions. However, its applicability to more complicated structures such as the mushroom structure investigated in Chapter 3 is another issue.

First of all, the mushroom structure has geometrical complications and is difficult to model with Geompack++. Even for the simple geometries of § 4.3, providing the necessary input files to perform meshing operations is a time-consuming task let alone the patch-via structure. Thus, its integration into the available software package requires more time and effort which is obviously out of the scope of a Master's thesis and its timeframe.

Geometry modeling aside, the more important downside is the use of a dense solver for solving the eigenvalue problem. The FE matrices, built during assembly process, are sparse. However, due to the lack of a suitable eigensolver for sparse singular matrices, at the final stage the matrix pair should be transformed and stored as full matrices so as to be analyzed by the eigensolver. As the complexity of the structure increases, the number of Dofs required for its accurate modeling gets larger. The larger the system of equations is, the longer computer simulations take. Moreover, the memory required to save these matrices is another issue that arises when dealing with many Dofs. The bottom line is that the simulation of the mushroom structure (open or shielded) is computationally costly and thus not feasible with the available computing platform and implementation.

A few attempts were made to explore ways of reducing the simulation time. One was to use lower-order elements. Tetrahedral edge elements of order (1,2) have relatively smaller number of Dofs ($6 + 14 = 20$) compared to (2,3) elements ($16 + 29 = 45$) and therefore may be used to assemble smaller FE matrices. Fig. 4.16 represents the result found for the region A $\rightarrow$ B of Fig. 4.12 using (1,2) elements with the same mesh used in §4.3.3 (154 elements) and 940 Dofs. Compared to Fig. 4.13, these results were obtained in a significantly shorter time –each point on the curves took the eigensolver 255 seconds to find. However, only one (blue squares) of the two degenerate modes of the structure was captured accurately. The eigenvalues obtained for the second mode (red triangles) were erroneous which is most likely due to the deficient number of elements. Reducing the order of elements while maintaining a coarse mesh is thereby not an option since a minimum number of Dofs is always required for accurate modeling in the FEM.

The alternative tried here was to store the matrix elements in single-precision format rather than the default double-precision format. With single-precision storing format the memory required to save the matrices is half of that of the double-precision format. It should, ordinarily, lead to faster simulations time. However, the simulation results were not accurate enough and therefore are not presented here.

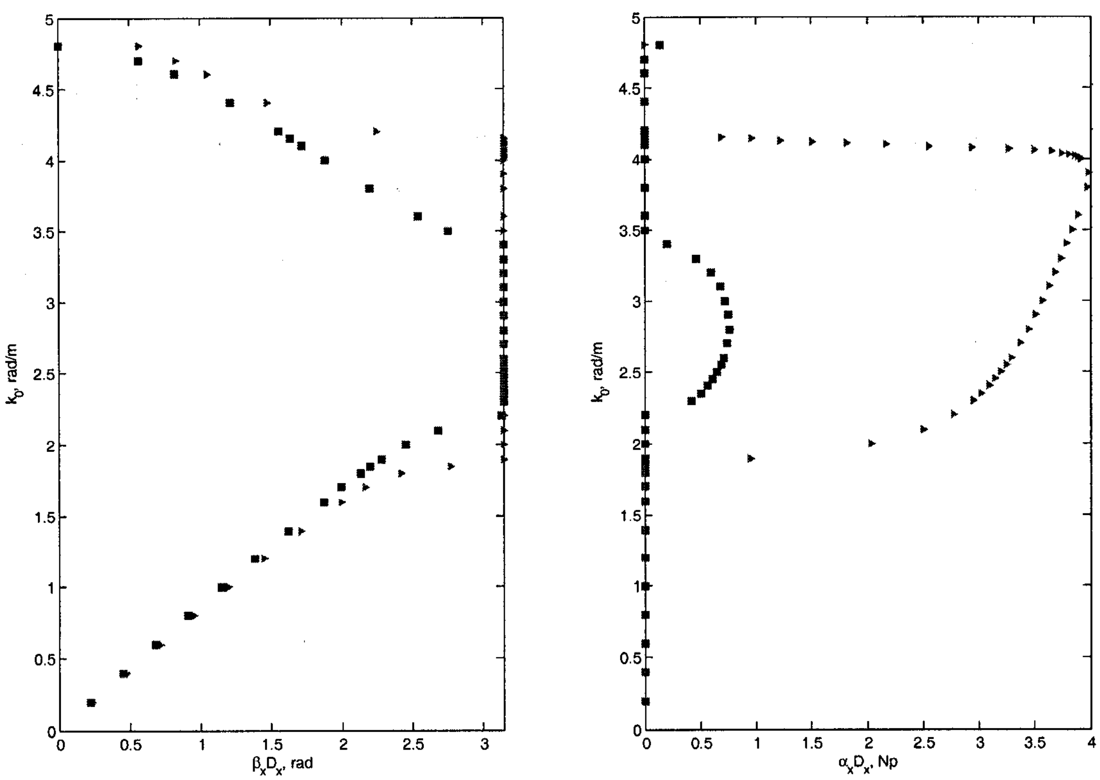

Fig. 4.16 Complex propagation constant of the triply periodic array in region A → B using (1,2) elements: (a) imaginary part, and (b) real part.

Chapter 5

Conclusion

5.1 Concluding Remarks

This thesis highlights the modal behavior of periodic structures in their forbidden frequency regions. The bandgap characterization was achieved using two different approaches: the transmission-line technique and the finite element method.

A transmission-line model for 2D periodic structures was investigated which allows for a complex formulation of the dispersion equation. The TL model was shown to be capable of capturing evanescent modes and predicting the stopband behavior of periodic structures.

Power distribution networks containing EBG structures can be efficiently modeled by 2D transmission line circuits. The developed TL model is exploited to investigate the band diagrams of the mushroom-type EBG structure embedded in a parallel-plate PDN; an arrangement which is commonly used for global suppression of switching noise in high-speed circuits. The transmission-line model allows for rapid production of band diagram and prediction of attenuation information within the induced bandgap regions. Fast characterization of the stopband behavior is particularly useful for investigation of the insertion loss achieved by inserting a prototype EBG in a parallel-plate PDN. Moreover, the developed TL model offers an efficient means of design optimization which can be used to determine the required specifications of an EBG structure for a target application. However, it was developed using major simplifications and is therefore of limited accuracy.

For accurate prediction of evanescent modes within the stopband, a finite element model was developed, implemented and verified. The FE simulation revealed various modal characteristics of periodic structures within their null transmission frequency ranges. Evanescent modes as well as complex modes have been shown to exist in the stopbands. The finite element code was tested on a few simple geometries. The FE results perfectly match those of the exact analytical solutions for one-dimensional periodic media. The band structure of doubly and triply periodic array of metal rods and cubes were investigated next. An excellent agreement was found between our results and those given in [12, 93], while the finite element formulation presented in this thesis allows for the prediction of bandgap behavior.

Lastly, both the TL model and the FE model have the advantage that the frequency is specified as an input parameter and the characteristic equation is solved for the complex propagation constant as an eigenvalue solution. This gives the applications great commercial potential as a software package.

5.2 Recommendations for Future Work

The accuracy of the generated band diagrams of the shielded mushroom structure investigated in § 3.2 can be further improved using a multiconductor transmission-line (MTL) [95, 96] model instead of a TL model with a simple lumped-element substitute for the EBG structure within the PPW. In [97], Elek and Eleftheriades presented a 1D MTL analysis of the shielded Sievenpiper structure that predicts the bandgap region as well as the dispersion characteristics of the lower order TM modes with accuracy comparable to finite element simulations. In that work, the shielded mushroom structure is investigated by applying Floquet analysis to the MTL structure formed by the parallel-plate conductors and mushroom patches. The future work from transmission-line viewpoint consists of modeling shielded EBG structures using a 2D MTL model.

The simulation models investigated in § 4.3 were simple periodic geometries. However, in practice, the periodic structures that are employed in power distribution network of PCBs are rather complex structures such as the patch-via EBG. The future work from finite-element viewpoint consists of modeling realistic and practical geometries such as those presented in § 3.2.

To be able to model realistic geometries, bigger matrices and more complex meshes are needed. Like all finite element analyses, the final step of the FE modeling, involves solving a large matrix equation. In this work, the resulting FE matrices were singular and the singular value decomposition (SVD) of the characteristic equation was carried out by MATLAB. MATLAB's built-in GSVD routines are not suitable for use with large, structured matrices as they are based on direct QZ algorithms and cannot handle large sparse matrices. Therefore, due to the singularity of matrices, the resulting characteristic equation could not be solved fast. This makes the FEM simulation of complex geometries with large number of Dofs inefficient. An alternative eigensolver which may be examined for this purpose is ARPACK++ [98]. ARPACK++ is an eigensolver for large sparse matrices which is capable of handling complex generalized eigenvalue problems. The matrices treated with ARPACK++ are not required to be Hermitian (nor positive definite) matrices. Therefore, GSVD can be carried out while the singular matrices are stored in compressed sparse column formats. However, for the class of complex generalized eigenvalue problems with singular matrices incurred here, the user is required to supply the necessary matrix-vector products by himself instead of passing them to ARPACK++ classes constructors.

Moreover, the FE formulation worked out in this thesis restricts the finite element mesh on opposite sides of unit cell to be exactly the same, referred to as periodic mesh. Consequently, for singly periodic structures two of the opposite boundary triangulations need to be identical in order to enforce the periodic boundary conditions (PBCs). For doubly and triply periodic structures, four and six boundary closures triangulations need to be matched, respectively, which makes the situation more restrictive. Periodic meshing of complex geometries critically limits the efficiency and reliability of the finite element model, as discussed in § 4.4. Vouvakis *et. al.* [99] proposed a new FEM method for analysis of infinite periodic structures which does not require a periodic mesh on either side of the PBC surfaces. In [99], the boundary value problem was transformed into a hybrid form and PBCs were weakly enforced on both sides of the Floquet cell through the use of the *cement* finite element method [100]. Therefore, a nonmatching triangulation can be employed which makes possible the use of other mesh generation packages.

Appendix A

Linearization of the Quadratic Eigenvalue Problem

Let $Q(\lambda) = \lambda^2 M + \lambda C + K$ be an $n \times n$ *matrix polynomial* of degree 2, where M, C and K are $n \times n$ complex matrices. $Q(\lambda)$ is often called a λ-matrix and its spectrum is denoted by $\Lambda(Q)$,

$$\Lambda(Q) = \{\lambda \in \mathbb{C} : \det Q(\lambda) = 0\} \tag{A.1}$$

which is the set of eigenvalues of $Q(\lambda)$. Two λ-matrices $P(\lambda)$ and $Q(\lambda)$ are *equivalent* if

$$P(\lambda) = E(\lambda)Q(\lambda)F(\lambda) \tag{A.2}$$

where $E(\lambda)$ and $F(\lambda)$ are λ-matrices with constant nonzero determinants. It follows that the the zeros of det $P(\lambda)$ and det $Q(\lambda)$ coincide [85].

The linearization for $Q(\lambda)$ involves finding its equivalent linear λ-matrix $A - \lambda B$. A $2n \times 2n$ linear λ-matrix $A - \lambda B$ is said to be a linearization of $Q(\lambda)$ [101] if

$$\begin{bmatrix} Q(\lambda) & 0 \\ 0 & I_n \end{bmatrix} = E(\lambda)(A - \lambda B)F(\lambda) \tag{A.3}$$

where $E(\lambda)$ and $F(\lambda)$ are $2n \times 2n$ λ-matrices with constant nonzero determinants. Obviously, the spectrum of $Q(\lambda)$ and $A - \lambda B$ coincide. A linearization is not unique and should be chosen with respect to the structural properties of $Q(\lambda)$ such as symmetry or definiteness, whenever possible.

The most popular linearizations used in practice are either from the first companion form [85]

$$L1: \qquad \begin{bmatrix} 0 & N \\ -K & -C \end{bmatrix} - \lambda \begin{bmatrix} N & 0 \\ 0 & M \end{bmatrix} \tag{A.4}$$

or of the second companion form

$$L2: \qquad \begin{bmatrix} -K & 0 \\ 0 & N \end{bmatrix} - \lambda \begin{bmatrix} C & M \\ N & 0 \end{bmatrix} \tag{A.5}$$

where N can be any nonsingular $n \times n$ matrix. It is straightforward to show that (A.4), for instance, is a linearizations of $Q(\lambda)$ [85]; simply choose,

$$E(\lambda) = \begin{bmatrix} -(C + \lambda M)N^{-1} & -I \\ -N^{-1} & 0 \end{bmatrix}, \qquad F(\lambda) = \begin{bmatrix} I & 0 \\ \lambda I & I \end{bmatrix} \tag{A.6}$$

and carry out the matrix multiplications; (A.3) follows trivially.

The choice between the first and second companion forms mainly relies on the singularity of M and K. If K is nonsingular (A.4) is the right choice while for a nonsingular M, (A.5) is preferred. In general N is chosen to be the identity matrix or a multiple of the identity matrix like $\|M\|I$ or $\|K\|I$.

References

[1] L. Brillouin, *Wave propagation in periodic structures : electric filters and crystal lattices.* New York : Dover Publications, 2nd ed., 1953.

[2] B. A. Munk, *Frequency selective surfaces : theory and design.* New York : John Wiley, 2000.

[3] R. E. Collin, *Field theory of guided waves.* New York : IEEE Press, 1991.

[4] R. M. Bevensee, *Electromagnetic slow wave systems.* New York : J. Wiley, 1964.

[5] Y. L. R. Lee, A. Chauraya, D. S. Lockyer, and J. C. Vardaxoglou, "Dipole and tripole metallodielectric photonic bandgap (mpbg) structures for microwave filter and antenna applications," *IEE Proc. Optoelectronics*, vol. 147, pp. 395–400, Dec 2000.

[6] B. Lenoir, D. B. S. Verdeyme, P. Guillon, C. Zanchi, and J. Puech, "Periodic structures for original design of voluminous and planar microwave filters," *IEEE MTT-S International Microwave Symposium Digest*, vol. 3, pp. 1479–1482, May 2001.

[7] L. H. Bertoni, L. H. S. Cheo, and T. Tamir, "Frequency-selective reflection and transmission by a periodic dielectric layer," *IEEE Trans. Antennas and Propagation*, vol. 37, pp. 78–83, Jan 1989.

[8] A. P. Feresidis, G. Goussetis, and J. C. Vardaxoglou, "Metallodielectric arrays without vias as artificial magnetic conductors and electromagnetic band gap surfaces," *IEEE Antennas and Propagation Society International Symposium*, vol. 2, pp. 1159–1162, June 2004.

[9] A. P. Feresidis, G. Goussetis, S. Wang, and J. C. Vardaxoglou, "Artificial magnetic conductor surfaces and their application to low-profile high-gain planar antennas," *IEEE Trans. Antennas and Propagation*, vol. 53, pp. 209–215, Jan 2005.

[10] W. Tsay and D. Pozar, "Application of the FDTD technique to periodic problems in scattering and radiation," *IEEE Microwave Guided Wave Lett*, vol. 3, pp. 250–252, Aug 1993.

[11] M. Bozzi and L. Perregrini, "Efficient analysis of FSSs with arbitrarily shaped patches by the MoM/BI-RME method," *IEEE Antennas and Propagation Society International Symposium*, vol. 4, pp. 390–393, July 2001.

[12] C. Mias, J. P. Webb, and R. L. Ferrari, "Finite element modeling of electromagnetic waves in doubly and triply periodic structures," *IEE Proc. Optoelectronics*, vol. 146, pp. 111–118, April 1999.

[13] W. S. Best, R. J. Riegert, and L. C. Goodrich, "Analytical dispersion analysis of loaded periodic circuits using the generalized scattering matrix," *IEEE Trans. Microw. Theory Tech.*, vol. 44, pp. 2152–2158, Dec 1996.

[14] A. Grbic and G. V. Eleftheriades, "Periodic analysis of a 2-D negative refractive index transmission line structure," *IEEE Trans. Antennas and Propagation*, vol. 51, pp. 2604–2611, Oct 2003.

[15] C. Caloz and T. Itoh, "Positive/negative refractive index anisotropic 2-D metamaterials," *IEEE Microwave and Wireless Components Letters*, vol. 13, pp. 547–549, Dec 2003.

[16] Y.-C. Chen, C. K. C. Tzuang, T. Itoh, and T. K. Sarkar, "Modal characteristics of planar transmission lines with periodical perturbations: their behaviors in bound, stopband, and radiation regions," *IEEE Trans. Antennas and Propagation*, vol. 53, pp. 47–58, Jan 2005.

[17] T. Kokkinos, C. D. Sarris, and G. V. Eleftheriades, "Periodic FDTD analysis of leaky-wave structures and applications to the analysis of negative-refractive-index leaky-wave antennas," *IEEE Trans. Microw. Theory Tech.*, vol. 54, pp. 1619–1630, April 2006.

[18] J. Ho, "Analysis of transmission lines embedded in power distribution networks containing electromagnetic bandgap structures," Master's thesis, McGill University, Dec 2005.

[19] J. Choi, V. Govind, and M. M Swaminathan, "A novel electromagnetic bandgap (EBG) structure for mixed-signal system applications," *IEEE Radio and Wireless Conference*, pp. 243–246, Sept 2004.

[20] R. Abhari and G. V. Eleftheriades, "Suppression of the parallel-plate noise in high-speed circuits using a metallic electromagnetic band-gap structure," *IEEE MTT-S International Microwave Symposium Digest*, vol. 1, pp. 493–496, June 2002.

[21] R. Abhari and G. V. Eleftheriades, "Metallo-dielectric electromagnetic bandgap structures for suppression and isolation of the parallel-plate noise in high-speed circuits," *IEEE Trans. Microw. Theory Tech.*, vol. 51, pp. 1629–1639, June 2003.

[22] T. Kamgaing and O. M. Ramahi, "A novel power plane with integrated simultaneous switching noise mitigation capability using high impedance surface," vol. 13, pp. 21–23, Jan 2003.

[23] C. Jinwoo, V. Govind, M. Swaminathan, W. Lixi, and R. Doraiswami, "Isolation in mixed-signal systems using a novel electromagnetic bandgap (EBG) structure," *IEEE 13th Topical Metting on Electrical Performance of Electronic Packaging*, pp. 199–202, 2004.

[24] J. C. W. Ho, Z. Quanyan, and R. Abhari, "Modeling of transmission lines with textured ground planes and investigation of data transmission by generating eye diagrams," *IEEE 13th Topical Metting on Electrical Performance of Electronic Packaging*, pp. 195–198, 2004.

[25] S. Shahparnia and O. M. Ramahi, "Miniaturized electromagnetic bandgap structures for ultra-wide band switching noise mitigation in high-speed printed circuit boards and packages," *IEEE 13th Topical Metting on Electrical Performance of Electronic Packaging*, pp. 211–214, Oct 2004.

[26] C. Guang, K. Melde, and J. Prince, "The applications of EBG structures in power/ground plane pair SSN suppression," *IEEE 13th Topical Metting on Electrical Performance of Electronic Packaging*, pp. 207–210, Oct 2004.

[27] D. Sievenpiper, Z. Lijun, R. F. J. Broas, N. G. Alexopolous, and E. Yablonovitch, "High-impedance electromagnetic surfaces with a forbidden frequency band," *IEEE Trans. Microw. Theory Tech.*, vol. 47, pp. 2059–2074, Nov 1999.

[28] D. M. Pozar, *Microwave engineering.* Hoboken, NJ : J. Wiley, 3rd ed., 2005.

[29] R. F. Harrington, *Time-Harmonic Electromagnetic Fields.* New York: IEEE Press: Wiley-Interscience, 2001.

[30] G. Floquet, "Sure les équations différentielles linéaries a coefficients périodiques," *Ann. École Norm. Sup.*, vol. 12, pp. 47–88, 1883.

[31] F. Bloch, "Über die quantenmechanick der electronen in kristallgittern," *Z. Physik*, vol. 52, pp. 555–600, 1928.

[32] E. W. Weisstein, "Fourier Series from MathWorld –A Wolfram web resource." http://mathworld.wolfram.com/FourierSeries.html, 2006.

[33] S. Guo and S. Albin, "Simple plane wave implementation for photonic crystal calculations," *Optics Express*, vol. 11, pp. 167–175, 2003.

[34] J. D. Shumpert, *Modeling Of Periodic Dielectric Structures (Electromagnetic Crystals)*. PhD thesis, University of Michigan, 2001.

[35] C. Christopoulos, *The Transmission-line Modeling Method: TLM*. Piscataway: IEEE Press, 1995.

[36] G. V. Eleftheriades, A. K. Iyer, and P. C. Kremer, "Planar negative refractive index media using periodically L-C loaded transmission lines," *IEEE Trans. Microw. Theory Tech.*, vol. 50, pp. 2702–2712, Dec 2002.

[37] F. Elek and G. V. Eleftheriades, "A two-dimensional uniplanar transmission-line metamaterial with a negative index of refraction," *New Journal of Physics*, vol. 7, pp. 1367–2630, Aug 2005.

[38] A. K. Iyer and G. V. Eleftheriades, "Negative refractive index metamaterials supporting 2-D waves," *IEEE MTT-S International Microwave Symposium Digest*, vol. 2, pp. 1067–1070, 2-7 June 2002.

[39] C. Caloz and T. Itoh, "Transmission line approach of left-handed (LH) materials and microstrip implementation of an artificial LH transmission line," *IEEE Trans. Antennas and Propagation*, vol. 52, pp. 1159–1166, May 2004.

[40] W. M. Robertson, S. A. Boothroyd, and L. Chan, "Photonic band structure calculations using a two-dimensional electromagnetic simulator," *J. Mod. Opt.*, vol. 41, pp. 285–293, Feb 1994.

[41] A. Mekis, J. C. Chen, I. Kurland, S. Fan, P. R. Villeneuve, and J. D. Joannopoulos, "High transmission through sharp bends in photonic crystal waveguides," *Phys. Rev. Lett.*, vol. 77, pp. 3787–3790, Oct 1996.

[42] H. Y. D. Yang, "Finite difference analysis of 2-D photonic crystals," *IEEE Trans. Microw. Theory Tech.*, vol. 44, pp. 2688–2695, Dec 1996.

[43] R. Mittra, C. H. Chan, and T. Cwik, "Techniques for analyzing frequency selective surfaces-a review," *Proceedings of the IEEE*, vol. 76, pp. 1593–1615, Dec 1988.

[44] K. S. Yee, "Numerical solution of initial boundary value problems involving Maxwell's equations in isotropic media," *IEEE Trans. Antennas and Propagation*, vol. 14, pp. 302–307, May 1966.

[45] A. Taflove and S. C. Hagness, *Computational electrodynamics: the finite-difference time-domain method*. Boston: Artech House, 2nd ed., 2000.

[46] D. Prescott and N. Shuley, "Extensions to the FDTD method for the analysis of infinitely periodic arrays," *IEEE Microwave Guided Wave Lett*, vol. 4, pp. 352–354, Oct 1994.

[47] P. Harms, R. Mittra, and W. KO, "Implementation of the periodic boundary condition in the finite-difference time-domain algorithm for FSS structures," *IEEE Trans. Antennas and Propagation*, vol. 42, pp. 1317–1324, Sept 1994.

[48] Y. Kao and R. Atkins, "A finite difference-time domain approach for frequency selective surfaces at oblique incidence," *IEEE Antennas and Propagation Society International Symposium*, pp. 1432–1435, 1996.

[49] J. Roden, S. Gedney, M. Kessler, J. Maloney, and P. Harms, "Time-domain analysis of periodic structures at oblique incidence: Orthogonal and nonorthogonal FDTD implementations," *IEEE Trans. Microw. Theory Tech.*, vol. 46, pp. 420–427, Apr 1998.

[50] K. L. Slrlagerl and J. B. Sclineiderz, "A selective survey of the finite-difference time-domain literature," *IEEE Antennas and Propagation Magazine*, vol. 37, pp. 39–56, Aug 1995.

[51] T. T. Zygiridis and T. D. Tsiboukis, "Higher-order finite-different schemes with reduced dispersion errors for accurate time-domain electromagnetic simulation," *Int. J. Num. Modeling: Electron. Netw. Devices and Fields*, vol. 17, pp. 461–486, Aug 2004.

[52] O. C. Zienkiewicz, *The finite element method.* London: McGraw-Hill, 3rd ed., 1977.

[53] J. L. Volakis, A. Chatterjee, and L. C. Kempel, *Finite element Method For Electromagnetics: Antennas, Microwave Circuits, and Scattering Applications.* New York : IEEE Press, 1998.

[54] R. L. Ferrari, "Finite element solution of time-harmonic modal fields in periodic structures," *Electronics Letters*, vol. 27, pp. 33–34, Jan 1991.

[55] P. Olszewski, "Expansion of periodic boundary condition for 3-D FEM analysis using edge elements," *IEEE Trans. Magnetics*, vol. 28, pp. 1084–1087, Mar 1992.

[56] D. T. McGrath and V. P. Pyati, "Periodic boundary conditions for finite element analysis of infinite phased array antennas," *IEEE Antennas and Propagation Society International Symposium*, vol. 3, pp. 1502–1505, June 1994.

[57] C. Mias and R. L. Ferrari, "Closed singly periodic three dimensional waveguide analysis using vector finite elements," *Electronics Letters*, vol. 30, pp. 1863–1865, Oct 1994.

[58] A. Freni, C. Mias, and R. L. Ferrari, "Finite element analysis of electromagnetic plane wave scattering from axially periodic cylindrical structures," *IEEE Antennas and Propagation Society International Symposium*, vol. 1, pp. 146–149, July 1996.

[59] C. C. Chen, "Scattering by a two-dimensional periodic array of conducting plates," *IEEE Trans. Antennas and Propagation*, vol. 18, pp. 660–665, Sept 1970.

[60] C. C. Chen, "Transmission through a conducting screen perforated periodically with apertures," *IEEE Trans. Microw. Theory Tech.*, vol. 18, pp. 627–632, Sept 1970.

[61] S. D. Rogers, "Electromagnetic-bandgap layers for broad-band suppression of tem modes in power planes," *IEEE Trans. Microw. Theory Tech.*, vol. 53, pp. 2495–2505, Aug 2005.

[62] S. Shahparnia and O. M. Ramahi, "A simple and effective model for electromagnetic bandgap structures embedded in printed circuit boards," *IEEE Microwave and Wireless Components Letters*, vol. 15, pp. 621–623, Oct 2005.

[63] S. Clavijo, R. Diaz, and W. McKinzie, "Design methodology for sievenpiper high-impedance surfaces: An artificial magnetic conductor for positive gain electrically small antennas," *IEEE Trans. Antennas and Propagation*, vol. 51, pp. 2678–2690, Oct 2003.

[64] F. Elek, R. Abhari, and G. V. Eleftheriades, "A uni-directional ring-slot antenna achieved by using an electromagnetic band-gap surface," *IEEE Trans. Antennas and Propagation*, vol. 53, pp. 181–190, Jan 2005.

[65] A. Corporation, "Ansoft's HFSS." http://www.ansoft.com/products/hf/hfss/, 2006.

[66] J. Jin, *The Finite Elements Method in Electromagnetics.* New York: Wiley, 2nd ed., 2002.

[67] J. P. Webb, G. L. Maile, and R. L. Ferrari, "Finite-element solution of three-dimensional electromagnetic problems," *IEE Proc. H*, vol. 130, no. 2, pp. 153–159, 1983.

[68] E. W. Weisstein, "Green's Theorem from MathWorld –A Wolfram web resource." http://mathworld.wolfram.com/GreensTheorem.html, 2006.

[69] R. L. Ferrari and R. L. Naidu, "Finite-element modeling of high-frequency electromagnetic problems with material discontinuities," *IEE Proc. A, Science, Measurement and Technology*, vol. 137, pp. 313–320, Nov 1990.

[70] J. P. Webb, "Edge elements and what they can do for you," *IEEE Trans. Magnetics*, vol. 29, pp. 1460–1465, Mar 1993.

[71] J. P. Webb and B. Forghani, "Hierarchal scalar and vector tetrahedra," *IEEE Trans. Magnetics*, vol. 9, pp. 1495–1498, Mar 1993.

[72] B. Joe, "Geompack & Mesh Generation." http://members.allstream.net/ bjoe/, 2004.

[73] J. P. Webb, "P3D version 1.5," 2005.

[74] "MATLAB website." http://www.mathworks.com/, 2006.

[75] R. Schneiders, "Mesh Generation & Grid Generation on the Web." http://www-users.informatik.rwth-aachen.de/ roberts/meshgeneration.html, 2006.

[76] S. J. Owen, "Meshing Research Corner." http://www-users.informatik.rwth-aachen.de/ roberts/meshgeneration.html, 2006.

[77] B. Joe, "Geompack++ file formats for regions and meshes," tech. rep., ZCS Inc, Calgary, AB, Canada, Sept 2003.

[78] B. Joe, "Geompack++ meshing operations," tech. rep., ZCS Inc, Calgary, AB, Canada, Sept 2003.

[79] J. P. Webb, "Hierarchal vector basis functions of arbitrary order for triangular and tetrahedral finite elements," *IEEE Trans. Antennas and Propagation*, vol. 47, pp. 1244–1253, Aug 1999.

[80] L. El-Esber, "Hierarchal higher order finite element modeling of periodic structures," Master's thesis, McGill University, Feb 2005.

[81] P. P. Silvester, "Universal finite element matrices for tetrahedra," *Int. J. Num. Modeling in Eng.*, vol. 18, pp. 1055–1061, 1982.

[82] H. Deitel and P. Deitel, *C++ How to Program.* Upper Saddle River, N.J. : Prentice Hall, 4th ed., 2003.

[83] S. McFee and J. P. Webb, "Adaptive finite element analysis of microwave and optical devices using hierarchal triangles," *IEEE Trans. Magnetics*, vol. 28, pp. 1708–1711, Mar 1992.

[84] O. C. Zienkiewicz, J. Z. Zhu, and N. G. Gong, "Effective and practical *h-p* version adaptive analysis procedures for the finite element analysis," *IEEE Trans. Magnetics*, vol. 28, pp. 879–891, Mar 1989.

[85] F. Tisseur and K. Meerbergen, "The quadratic eigenvalue problem," *SIAM Review*, vol. 43, pp. 235–286, May 2001.

[86] C. B. Moler and G. W. Stewart, "An algorithm for generalized matrix eigenvalue problems," *SIAM J. Num. Anal.*, vol. 10, pp. 241–256, May 1973.

[87] V. N. Kublanovskaya, "On an approach to the solution of the generalized latent value problem for λ-matrices," *SIAM J. Num. Anal.*, vol. 7, 1970.

[88] A. Ruhe, "Algorithms for the nonlinear eigenvalue problem," *SIAM J. Num. Anal.*, vol. 10, pp. 674–689, Sept 1973.

[89] G. Peters and J. H. Wilkinson, "Inverse iteration, ill-conditioned equations and Newton's method," *SIAM Review*, vol. 21, pp. 339–360, May 1979.

[90] G. H. Golub and C. F. V. Loan, *Matrix Computations.* Baltimore : Johns Hopkins University Press, 3rd ed., 1996.

[91] R. Barrett, M. W. Berry, T. F. Chan, J. Demmel, J. Donato, J. Dongarra, V. Eijkhout, R. Pozo, C. Romine, and H. van der Vorst, "Templates for the solution of linear systems: Building blocks for iterative methods," tech. rep., SIAM, Philadelphia, 1993.

[92] H. Zha, "Computing the generalized singular values/vectors of large sparse or structured matrix pairs," *Numerische Mathematik*, vol. 72, pp. 391–417, Jan 1996.

[93] C. Mias, J. P. Webb, L. El-Esber, and R. L. Ferrari, "Finite element modeling of electromagnetic waves in doubly and triply periodic structures," *IEE Proc. Optoelectronics*, vol. 152, p. 274, Oct 2005.

[94] R. L. Ferrari, "Electronic band-structure for two-dimensional periodic lattice quantum configurations by the finite element method," *Int. J. Num. Modeling: Electron. Netw. Devices and Fields*, vol. 6, no. 4, pp. 283–297, 1993.

[95] S. Frankel, *Multiconductor transmission line analysis.* Dedham, Mass. : Artech House, 1977.

[96] J. A. Faria, *Multiconductor transmission-line structures : modal analysis techniques.* New York : J. Wiley, 1993.

[97] F. Elek and G. V. Eleftheriades, "Dispersion analysis of the shielded sievenpiper structure using multiconductor transmission-line theory," *IEEE Microwave and Wireless Components Letters*, vol. 14, pp. 434–436, Sept 2004.

[98] F. Gomes and D. Sorensen, "ARPACK++ beta version." http://www.ime.unicamp.br/ chico/arpack++/, 2006.

[99] M. N. Vouvakis, K. Zhao, and J. F. Lee, "Finite-element analysis of infinite periodic structures with nonmatching triangulations," *IEEE Trans. Magnetics*, vol. 42, pp. 691–694, Apr 2006.

[100] S.-C. Lee, M. N. Vouvakis, and J.-F. Lee, "A non-overlapping domain decomposition method with non-matching grids for modeling large finite antenna arrays," *Journal of Computational Physics*, vol. 203, pp. 1–21, Feb 2005.

[101] I. Gohberg, P. Lancaster, and L. Rodman, *Matrix Polynomials.* New York : Academic Press, 2nd ed., 1982.